# Mechanical, Electrical and Chemical Effect of Laser Spike Annealing on Novel Porous Low Dielectric Constant Ethyl-Bridged Organosilane

A Thesis

Presented to the Faculty of Graduate School

of Cornell University

In Partial Fulfillment of the Requirement for the Degree of

Master of Science

by

Zeming Sun

August 2014

## ABSTRACT

Scaling of semiconductor devices has also driven a need for the improvement of interconnects. As feature sizes became smaller, the parasitic capacitance increased between wires resulting in unacceptable interconnection delay. To mitigate this problem, low dielectric constant materials ("low *k*" materials) were introduced to replace the silicon dioxide, whose *k* value around 4 is well outside the target value of $k = 2.0$. While the incorporation of organic groups and, especially, the presence of pores in an Si-O framework material decreases the dielectric constant dramatically, it also leads to the loss of mechanical strength. Alternative processing technologies are required to improve mechanical properties of SiCOH-class materials, the current standard for low *k* materials, while maintaining dielectric properties. Laser Spike Annealing (LSA) is one alternative annealing process that may achieve this goal.

This work explored the use of LSA to anneal porous low *k* ethyl-bridged organosilane films. This novel SiCOH-class material has the potential to meet targets with respect to lower dielectric constant and stronger mechanical properties. Use of LSA was explored to determine the behavior under several heating processes. The effects of LSA on this new low *k* film and a comparison of the results to those using other rapid annealing techniques were studied.

In this thesis, we will discuss the structural and chemical evolution as a function of LSA and hotplate conditions. Second, we will link the dielectric and mechanical effects of LSA to those structural changes under a continuous temperature profile. Third, we will explore the effects of dwell time, initial structure and initial porosity on the LSA-generated results. Finally, we will evaluate and compare LSA and the conventional hotplate annealing.

## BIOGRAPHICAL SKETCH

Zeming Sun was born in the Chinese city of Shijiazhuang, a transportation hub and industrial city not far from Beijing. At the age of 18, he entered Beijing University of Science and Technology and majored in Materials Science and Engineering. In his Sophomore year, he joined Professor Wenjiang Qiang's group and later completed the thesis "Eddy Current Testing of Thermal Aging of Duplex Stainless Steel in Nuclear Plants". After completing his Junior year, he exchanged to Pohang University of Science and Technology in Republic of Korea (South). In Professor Nack-Joon Kim's group, he completed the project "The Microstructure and Texture of 3.5wt% Silicon Steel by Twin Roll Process". In June 2012, he obtained Bachelor's of Engineering degree. Before he started graduate study at Cornell University, he went to Tohoku University in Japan and interned in Professor Masashi Sahashi's group. He made preparation for shifting his research focus to electronic materials and completed the project "Influence of Nano-oxide Layer in Mn-Ir Based Spin Valve Multilayers". At Cornell, he was fortunate to have Professor Michael Thompson as his mentor. His master thesis is about laser spike annealed low dielectric constant materials. While performing his research in Professor Thompson's group, Zeming was motivated to pursue a Ph.D degree. He decided to enroll in Electrical Engineering department at Oregon State University in September 2014.

**ACKNOWLEDGEMENTS**

This thesis would not have been possible without support from my family. I owe my sincere gratitude to my parents and my sister. They encourage me to pursue my academic dreams and always provide me helpful suggestions. I am privileged to be educated abroad with love, company and sacrifice of my parents. I always keep their love, support and encouragement in my mind.

I am fortunate to have Professor Michael Thompson as my mentor and advisor. He is an extremely smart person. With his guidance, I have gained significant amount of theoretical knowledge in my filed of interest, but most importantly, I have learned how to conduct researches independently. Also, Professor Thompson is very nice, patient and experienced. Whenever I faced up with difficulties, he could provide me plenty of practical advice and far-sighted ideas. He led me to leap from an undergraduate student into a graduate researcher. I would like to express the deepest appreciation to Professor Thompson here.

I am also sincerely grateful to Professor Paulette Clancy. Throughout my graduate study, she is always ready to offer me valuable help and open for helpful directions. Her teaching in the group meeting made me a better researcher. And, her recommendation allowed me to get the opportunity to enrich myself in the doctoral study.

I give my special thanks to my sub-group teammates, Bob Bell and Zheyi Han. Bob, as a project leader, helped and led me to jump-start my graduate research. I would like to thank Yao Sun and Duhan Zhang from Professor Ulrich Wiesner's group for helping me with preparing samples. I also appreciate Byungki Jung, Jing Jiang and Kwan Tan for giving me advice in both organic and physical chemistries.

It was my pleasure to work with my group colleagues, Xuetian Ma, Suki Zhang, Chen-Yang Chung, Bin Zhu, David Lynch, Wenjin Zhang and Alan Jacob. I will truly miss everyone.

Finally, all Cornell Nanofabrication Facilities (CNF) and Center of Materials Research (CCMR) facility members are gratefully acknowledged.

## CONTENTS

LIST OF TABLES

LIST OF FIGURES

CHAPTER 1

# INTRODUCTION

## *1.1Use of Low k Materials*

According to Moore's Law, the number of active devices on a chip is approximately doubling every two years. To keep up with this trend, a corresponding feature size reduction of microelectronic devices is required. As a result of this miniaturization of size scaling, signal delay and cross-talk are becoming increasingly important. Signal delay originates from both gate delay and interconnect delay. As shown in Figure 1.1, interconnect delay began to dominate when the transistor size (known as the technology node scale) decreases below 250 nm. Currently, the industry is approaching 11 nm nodes, hence the issue related to interconnect delay has become a critical issue to solve.

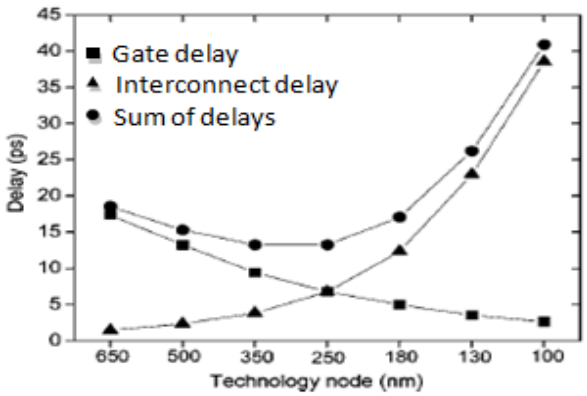


Figure 1.1 Calculated gate and interconnect delay as a function of technology node. Reprinted with permission from [1].

In integrated circuits (ICs), Cu wires contact semiconductor devices, while dielectric films are used to separate inter-level and intra-level Cu wires (Figure 1.2a). This interconnection can be simplified as a chain of resistors (Cu wires) and capacitors (dielectric parts between adjacent

wires), as shown in Figure 1.2b. The interconnect delay time, τ, is given by $\tau = RC$ , where R is the resistance of the wires and C is the parasitic capacitance.

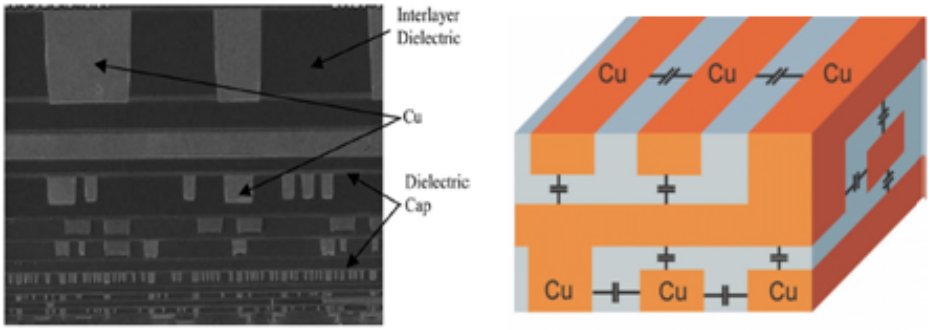


a) Cross-section of interconnects in ICs. b) Simplified diagram of interconnects.
Figure 1.2 Use of low *k* materials and schematic of interconnects in ICs.
Reprinted with permission from [2].

Therefore, resistance and capacitance are two essential influences on the choice of new materials. The first effort to reduce τ occurred with the switch from aluminum to copper wires to take advantage of copper's lower resistivity. More recently, industry is working to replace silicon dioxide ($k$ = 4.0) with a lower k material (the lowest reported $k$ value is around 1.8[1]), but a target value of around 2.0 is still generally unavailable for a material which satisfies other property constraints.

A capacitor is an electronic device consisting of two conductors separated by a dielectric. The classic parallel plate model (Figure 1.3) has a capacitance, given by

$$\mathrm{C} = k\varepsilon_0 \cdot \frac{\mathrm{A}}{\mathrm{d}} \tag{1.1}$$

where C is the capacitance, $k$ is the dielectric constant, A is the plate area, d is the separation and $\varepsilon_0$ is the dielectric constant of vacuum. This relationship illustrates the reason for using low $k$ materials to reduce parasitic capacitance.

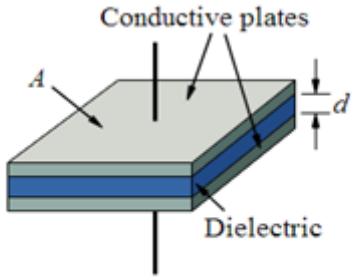


Figure 1.3 Parallel plate model.

### *1.2 Polarization-The Source of Dielectric Constant*

To conduct a rational design of new low $k$ materials, an understanding of the origin of the dielectric constant, namely polarization, is necessary. Following discussion of the mechanisms of polarization, we will discuss methods to decrease the dielectric constant in this section.

#### *1.2.1 Mechanisms for Polarization*

Dielectrics are defined in terms of the response of their electrons to an applied electrical field, known as the polarization. Under an external electrical field, electronic charges cannot move through dielectrics but are induced onto the surface of dielectrics, as shown in Figure 1.4.

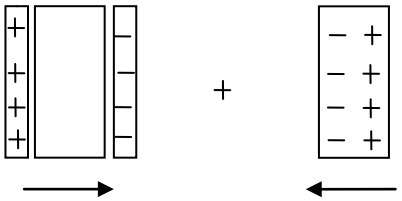

a) External electrical field. b) Polarized charges.

Figure 1.4 Polarization phenomenon.

The dielectric response depends on the frequency of the external electrical field, and hence must be defined as a complex function

$$\hat{k}(\omega) = k'(\omega) + ik''(\omega) \tag{1.2}$$

where *k*' is the real part of the dielectric constant and *k*'' is the imaginary part of the dielectric constant. A typical frequency dependence is summarized in Figure 1.5.

Various polarization mechanisms contribute to the dielectric constant, including atomic polarization, bond polarization, orientational polarization, relaxation polarization and space charge polarization[5].

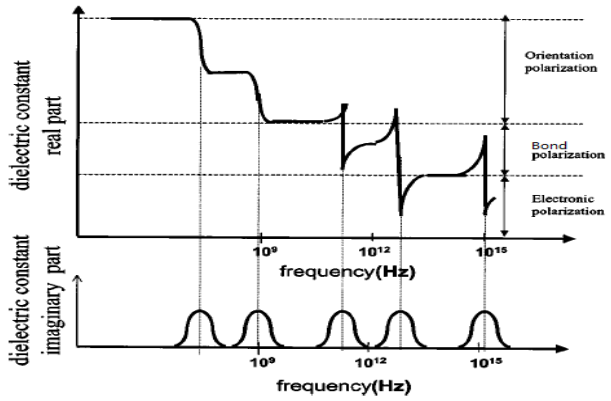


Figure 1.5 Frequency dependence of the real and imaginary part of the dielectric constant. Reprinted with permission from[4].

***Atomic Polarization***

Atomic polarization dominates in the optical frequency range from $10^{14}$-$10^{16}$ Hz. In this regime, the applied electronic field leads to centroid displacement of negative charge with respect to positive charges inside the atoms, creating a dipole moment. The dipole moment is determined by the radius of the electron clouds; hence, to decrease atomic polarization, elements with small atoms and bonds with symmetric structures are preferred.

***Bond Polarization***

For frequencies in the range of $10^{12}$-$10^{13}$ Hz, bond polarization (or ion polarization) is generated between atoms of different electronegativities. Atoms with higher electronegativities attract more electrons and lead to a higher local electron density. Besides electronegativity, the atom radius also has an effect on the electric dipole moment, **p**, by limiting the charge separation distance.

From a macro-scale perspective, the dipole moment, **p**, is determined by an external electric field, $\mathbf{E_0}$, and an intrinsic parameter of the bonds, given by the polarizability, α. Thus, the dipole moment **p** can be expressed as

$$\mathbf{p} = \alpha \mathbf{E}_0. \tag{1.3}$$

Connected to a micro-scale analysis, the polarizability, α, is mainly determined by bond length, bond energy and the difference of electronegativity. The bond polarizability provides guidance for new materials design, as shown in Table 1.1. The C-C bond has a relatively low polarizability, whereas O-H bonds, potentially created during synthesis or due to water absorption, has a high polarizability.

Table 1.1 The polarizability of bonds in polymers with low polarizability[1].

| Bond | C-C | C-F | C-O | C-H | O-H | C=O | C=C | C≡C | C≡N |
|---|---|---|---|---|---|---|---|---|---|
| Polarizability[$Å^{-3}$] | 0.53 | 0.56 | 0.58 | 0.65 | 0.71 | 1.02 | 1.64 | 2.04 | 2.24 |

***Orientational Polarization and Other Mechanisms***

Dipole orientational polarization occurs in polar molecules with permanent dipoles and operates in the frequency range of $10^5$-$10^{10}$ Hz. Under an external electrical field, permanent dipoles will change their orientation to achieve a minimum energy state. Orientational polarization is common in polymers and glasses, but less common in covalent or ionic insulators.

Relaxation polarization and space charge polarization occur at very low frequencies. Relaxation polarization is related, for example, to the unsaturated terminal groups of a polymer chain. Under an external electrical field, these labile groups move easily, resulting in polarization. Space charge polarization arises from impurities, inhomogeneity and interfaces. These defects become the barriers to electron motion, leading to accumulation of electrons in these areas. In

summary, a uniform film with few labile groups is preferred and post annealing contributes to this preference by reducing the number of terminal groups or rearranging terminal structures.

### *1.2.2 Clausius-Mossotti Relationship*

The macroscopic property of the dielectric constant, *k*, is connected to the microscopic parameter, the polarizability, α, by the Clausius-Mossotti relationship[1,3,4]. This relation quantitatively discusses three major polarization contributions, that is, atomic, bond and orientational polarization.

First, Lorentz local field theory is introduced to show how a local field acts on a microscopic system. To achieve this, a sphere void (Figure 1.6) is created in the model, leaving all other molecules unchanged. The depolarization field of the Lorentz void can be expressed as

$$\mathbf{E_d} = \frac{\mathbf{P}}{3\varepsilon_0} = \frac{\varepsilon_0 \chi \mathbf{E_0}}{3\varepsilon_0} = \frac{(k-1)\mathbf{E_0}}{3} \tag{1.4}$$

where χ is the susceptibility of the material and the fraction of 1/3 is a shape factor for the sphere. Consequently, the local electrical field of a Lorentz void can be expressed as

$$\mathbf{E_{loc}} = \mathbf{E_0} + \mathbf{E_d} = \frac{k+2}{3}\mathbf{E_0}. \tag{1.5}$$

The connection between the macroscopic picture and the microscopic picture is based on their relevant expressions of the total polar moments, given as

$$\mathbf{P} = n_0 \alpha \mathbf{E_{loc}} = \varepsilon_0 (k-1)\mathbf{E_0}. \tag{1.6}$$

where $n_0$ is the density of polarized particles. The particle number density $n_0$ can be expressed by the mass density ρ and molecular weight M in the equation

$$n_0 = \frac{\rho N_A}{M}. \tag{1.7}$$

Based on equations 1.5-1.7, the Clausius-Mossotti relationship is given by

$$\frac{k-1}{k+2} = \frac{n_0 \alpha}{3\varepsilon_0} \text{ or } \frac{k-1}{k+2} = \frac{\rho N_A \alpha}{3M\varepsilon_0}. \tag{1.8}$$

According to multiple mechanisms, the total polarizability, α, is achieved by the addition of the atomic polarizability, $\alpha_a$, the bond polarizability, $\alpha_b$, and the orientational polarizability, $\alpha_o$. Finally, the Clausius-Mossotti relationship can be written as

$$\frac{k-1}{k+2} = \frac{\rho N_A}{3M\varepsilon_0}(\alpha_a + \alpha_b + \alpha_o). \quad (1.9)$$

### *1.2.3 Methods of Decreasing Dielectric Constant*

According to the Clausius-Mossotti relationship, the dielectric constant, *k*, can be reduced by two methods: decreasing the polarizability or decreasing the dipole density[1].

***Decreasing Polarizability***

To achieve low *k* materials, it is preferable to work with non-polar and low polarizable bonds[1].

Preferable materials are those with few polar chemical groups and those with a symmetric structure that cancels the dipoles of chemical bonds between dissimilar atoms. For example, a methyl group can be introduced to replace a hydrogen terminus. Also, precursors with symmetric bridges or cubic structures can be used to decrease the polarizability.

In addition, the bond polarizability can be decreased by the incorporation of lower polarization bonds. For example, Si-O bonds can be replaced with less polarizable Si-F, Si-H and Si-C bonds. According to Table.1, the incorporation of C-C bonds can further decrease the polarizability.

***Decreasing Density and Introducing Pores***

The density can be decreased by increasing the free volume (porosity) in the materials. This can be achieved in two ways: arranging the material structure (constitutive pores) or introducing deliberate porosity (subtractive pores)[4,6].

Constitutive pores can be achieved by three methods: choosing precursors with porous structures, introducing network connectivity during synthesis, and rearranging the cross-linking by post processing. First, precursors with initial pores can be found in materials with cubic

structures, benzene groups and cyclic polymers. Second, the increase of network connectivity can be achieved by introducing bulky monovalent groups or by increasing the extent of cross-linking organic bonds. Third, post treatment by heat or UV exposure can be an effective method to remove long labile groups or crosslink bonds.

Subtractive pores can be achieved by two methods. The first is to use porogens (surfactants) in a sol-gel process to create self-assembled nanoparticles, which are desorbed into nanopores. The second is to limit the incorporation of agglomerates in the gas phase of a plasma enhanced chemical vapor deposition (PECVD). The reason why such deliberate porosity can decrease the dielectric constant can also be understood by remembering that the dielectric constant of air, $k_{air}$, has a value approximately 1.

***Summary***

Methods to reduce the dielectric polarizability need to be considered simultaneously. In most cases, structural rearrangement can bring about positive and negative effects at the same time. For example, the incorporation of $-CH_3$ groups not only leads to an more open structure, but also contributes to the lower polarizability. However, it can increase the relaxation polarization and deteriorate the thermal stability as a labile terminal group. Similarly, the density must not be so low as to reduce the mechanical strength, even though the open structure can effectively decrease the *k* value. Given the complex design window, low *k* materials focus more on the final properties. The history of the development of low *k* options is discussed in the next section.

***1.3 Low Dielectric Constant Materials***

Several approaches have been explored to decrease the dielectric constant [1,2,4]. Chronologically speaking, fluorine was first added into silicon dioxide, to introduce porosity and for its lower electronegativity. However, the decrease of dielectric constant was substantial (a *k*

value around 3.8). Subsequently, organic polymers have been considered, which was shown to dramatically reduce the *k* value, but they failed to achieve the required mechanical strength. Most recently, the hybrid materials, inorganic silicon dioxide mixed with organic groups, have been widely studied. This class of materials, commonly known as SiCOH, have achieved low *k* while also shown a mechanical strength improvement compared to that of the previous organic polymers. Porosity has been introduced to further decrease the dielectric constant of SiCOH films. Porous SiCOH dominates the field of low *k* materials in terms of the prevalence of use to date, and thus, this class as well a novel generation of carbon-bridged organosilanes that has been posited as a potential low k material are discussed further[1,4].

### *1.3.1 Classification of Typical Low Dielectric Constant Materials*

#### *Silicon Dioxide and Fluorine Doped Silicon Dioxide*

Silicon dioxide ($SiO_2$) is the conventional material used as the dielectric in transistors. It shows a high chemical and thermal stability, due to its dense structure (Figure 1.6a). However, the relatively high polarizability of Si-O bond leads to a high dielectric constant of 4. To lower the *k* value, two methods have been explored in which Si-O bonds are replaced with Si-F bonds or Si-$CH_3$ bonds (as discussed in the next section). As discussed above, both chemical groups are less polarizable and they can be expected to increase the interatomic distance and the 'free volume' inside the tetrahedral structure.

Fluorosilicate glass (F-$SiO_2$) has a structure in which fluorine substitutes for oxygen in the $SiO_2$ framework, as shown in Figure 1.6b. The dielectric constant that can be achieved in this way is around 3.6-3.9. Besides the two advantages discussed above, the Si-F bond is the second strongest single bond, which can decrease bond polarization and increase resistance to oxidation[1]. However, when the doping content of fluorine is above 4%, the structure is not

stable against high moisture absorption. This absorbance must be strictly prevented, since the *k* value of water is around 80. For this reason, F-$SiO_2$ cannot be used to further decrease the *k* value. Thus, amorphous carbon and organic polymers are considered to further decrease the dielectric constant.

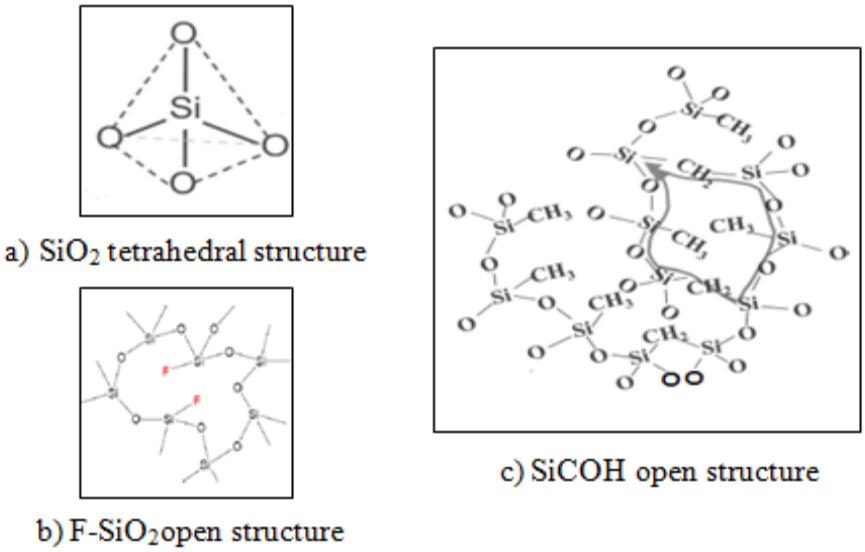


a) $SiO_2$ tetrahedral structure

b) F-$SiO_2$open structure

c) SiCOH open structure

Figure 1.6 Summary of structures in silicon dioxide, fluorine doped silicon dioxide and methyl doped silicon dioxide. Reprinted with permission from[4].

***Amorphous Carbon***

According to the carbon $sp^3/sp^2$ ratio and the hydrogen content, $C_H$, amorphous carbon materials can be cataloged into three kinds of materials. First, when the carbon atoms are mainly $sp^3$ hybridized and the hydrogen content is above 50%, such materials can be described as polymer-like, a-CH. These materials are mechanically soft with a low k value. However, if the $sp^3$ content remains high while the hydrogen content is reduced below 1%, it is referred to as a tetrahedral amorphous carbon (taC), which is a very hard film. Finally, when the $sp^2$ content dominates the hybridization and the hydrogen content is lower than 30%, it is called a diamond-like carbon (DLC). This film is hard due to the insertion of graphitic clusters into the $sp^3$ network. Compared

to these amorphous carbons, graphite is highly $sp^2$ hybridized and diamond is highly $sp^3$ hybridized[1,4].

These three kinds of amorphous carbon materials, along with graphite and diamond, are well studied as candidates of low *k* materials. Their properties, as shown in Table 1.2, do not exhibit sufficiently low *k* values. Also, there are concerns of thermal stability and mechanical properties, which also make amorphous carbons uncompetitive in this field.

Table 1.2 The properties of amorphous carbon, graphite and diamond[1].

| Properties | diamond | graphite | taC | DLC | Polymer-like |
|---|---|---|---|---|---|
| *k* value | 5.58 | conductor | 6.5 | <4 | 2.2-2.3 |
| Hardness(GPa) | 90-150 | 0.3 | 40-80 | 2-30 | soft |

***Organic polymers***

Organic polymers were also explored, since a number of polymers initially have dielectric constant below 4.0 and many also have a high toughness and crack-resistance. After screening in early research, four types of polymers have been identified for study, including polymides, polybenzoxazoles, polyarylene ethers and polyarylenes. The dielectric constant of dense polymers without deliberate porosity is about 2.65-3.3[1].

In spite of these significant advantages, organic polymers have some intrinsic drawbacks. First, their mechanical strength and hardness are very low. Also, it is not easy to meet the thermal and oxidative stability requirements. The stringent requirements of a high glass transition temperature and low oxygen sensitivity have further diminished enthusiasm for organic polymers as a replacement for $SiO_2$.

### *1.3.2 SiCOH and Porous SiCOH*

In the class of inorganic dielectrics, $SiO_2$ already has a low dielectric constant, so a hybrid structure incorporating organic groups into the inorganic $SiO_2$ backbones has drawn much attention. These materials are generally referred to as SiCOH.

***Structures of SiCOH***

SiCOH has a structure with some degree of $-CH_3$ substitution for oxygen in the $SiO_2$ network and with $-CH_2$ bridges between silicon atoms, as shown in Figure 1.6c. Closed pores can be generated by $-CH_2$ bridges and open pores by $-CH_3$ groups. Due to this natural porosity, the dielectric constant can achieve values as low as 2.5-3.5. With deliberate porosity introduced into the structure, the dielectric constant can be further decreased to be as low as 1.8. However, the introduction of pores also dramatically decreases its mechanical strength[1,4].

Generally, the 3-D structures of SiCOH are cataloged into three kinds: random cross-linked structures, ladder structures and cage-like structures. The cage-like structure (Figure 1.7c) has a T8 cubic unit with eight silicon atoms on the vertices and a large Si-O-Si bond angle of around $150^{\circ}$. With more open space, it has a lower *k* value, but poor mechanical properties. Comparatively, the randomly cross-linked structure (Figure 1.7a) has a network composed of different bonding and a small Si-O-Si bond angle of $144^{\cdot}$, yielding higher mechanical strength[7].

The cage-like structure is favored to allow space for the organic groups, especially if the functional groups are large. In this case, the intermolecular interaction can be minimized by the cage-like structure, which in turn leads to a lower connectivity. Due to the priority of decreasing the *k* value, this structure was predominant in the early years. Most recently, the goals have changed to strengthening the materials while maintaining the existing low *k* value, so high

network connectivity becomes preferred. Post annealing has been shown to break down the polyhedral structure and to recreate the cross-linking[1,8].

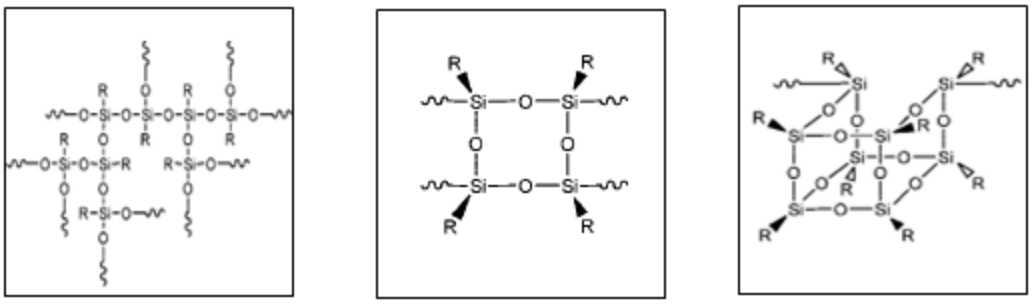

a) Radom cross-linked structure b) Ladder structure c) Cage structure

Figure 1.7 Summary of SiCOH 3D structures. Reprinted with permission from [1].

***H ydrogen Silsesquioxane(HSSQ)***

Addition of hydrogen atoms was first used to expand the dense $SiO_2$ structure. This material is referred to as hydrogen silsesquioxane (HSSQ), and its structure is similar to F-doped $SiO_2$. However, it has much better properties with a *k* value below 2.8 and a modulus of 8.3 GPa[1,4]. Compared to F-$SiO_2$, more hydrogen can be incorporated into the film, leading to these improvements.

In spite of the excellent physical properties, the existence of unusual thermal transformations in a temperature range, that is likely to be experienced during subsequent processing to create electronic devices, has had a negative effect on the implementation of HSSQ. When heated, HSSQ first transforms from a cage-like structure to a more randomly cross-linked network structure that is favored at temperatures between 250 and 350 ℃. Above 350 ℃, porosity is formed with the loss of $SiH_4$ and hydrogen. After it reaches 450 ℃, a final reconstruction occurs with the formation of $SiO_2$. Also, similar to polymers, oxygen sensitivity is another important

problem in the application. The Si-H bond can be easily oxidized, resulting in the deterioration of electronic properties and a pathway for stress cracks[1].

***Methyl Silsesquioxane(MSSQ)***

Methyl silsesquioxane (MSSQ) is a typical SiCOH film, when the hydrogen is substituted with methyl groups. Its dielectric constant is comparable to that of HSSQ, but its mechanical modulus of 3.8-4.5 GPa is relatively low, since the Si-O-Si network is less dense with more open space near each silicon atom. The most attractive properties of MSSQ are its low oxygen sensitivity and high temperature stability. This material is acceptable in current practice, but its intrinsic brittleness, leading to vulnerability to cracking, pushes research to novel alternatives[1].

***Three Approaches that Improve SiCOH Structure***

First, additional C-C bonds need to be created by doping ethyl or methyl groups. It has been demonstrated that the dielectric constant is strongly influenced by its carbon content. In other words, to meet the requirement of a low dielectric constant, the carbon level needs to be maintained or increased[1].

Second, it is preferred to achieve a higher ratio of the randomly cross-linked network to cage-like structures. This can be accomplished by controlling the initial precursor or relying on the annealing processes.

Third, carbon bridges can be introduced as part of the network. In this approach, the carbon bridge is a combination of both additional functional carbon groups and a continuous network. This leads to a 4-5 times higher value of the mechanical strength than other films of similar densities and dielectric constant[1].

Based on these approaches, carbon-bridged organosilicas are discussed below as a potential candidate in the SiCOH family.

### *1.3.3 Carbon-Bridged Organosilanes*

Currently, there are several prospective candidates for low dielectric constant materials. However, most of them cannot be commercialized because of their inability to satisfy either the desired properties or the integration requirement.

Two exceptions are zeolites and carbon-bridged organosilanes. Zeolites have a crystalline structure with micropores. The crystalline nature contributes to a better mechanical properties, while this material also takes advantages of micropores to exhibit excellent dielectric constants. It is reported that the modulus can be as high as 30-40 GPa, with the dielectric constant of 2.7-3.1. However, the pore size is too large to be useful in current microelectronics.

***Advantages of Carbon-Bridged Organosilanes***

Carbon-bridged organosilanes are reported to have a low dielectric constant of around 2.3 and a modulus strength of 7.5 GPa[9,10]. A comparison of structures between carbon-bridged organosilanes and other typical low *k* materials is given in Figure 1.8.

The good mechanical properties can be attributed to three features: First, the Si-O-Si bonds greatly increase the Young's modulus and hardness. Second, the carbon bridges contribute further to network connectivity. Finally, the Si-C-Si bond is more stable than Si-$CH_3$ bond, so the bridges can also contribute to thermal stability during the processing.

Three features also contribute to the low *k* value: First, the carbon bonds are less polarizable than other organic groups, as given in Table 1.1. Second, the open structure in MSSQ can be enhanced by the extra carbon chains. Third, pores can be deliberately created by adding porogens during synthesis. Pores provide the major contribution to the low dielectric value, as discussed.

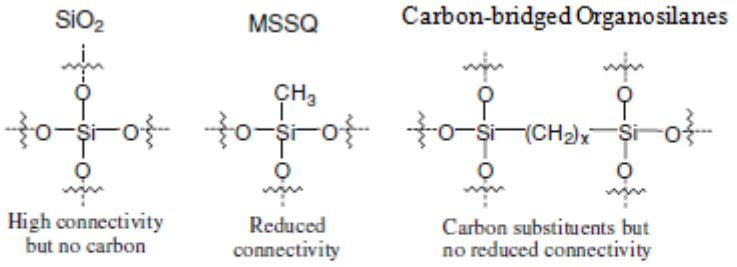


Figure 1.8 Structure comparison of $SiO_2$, MSSQ and carbon-bridged organosilanes. Reprinted with permission from[8].

***Effects of Pores***

The size, the ratio (porosity), the shape and the distribution of pores can all influence the final properties. The "open structures", mentioned above, are difficult to measure, and only deliberate pores can be characterized and will be discussed in this section.

For pore shapes, several idealized structures are shown in Figure 1.9. In 3D, the idealized shapes are cylindrical and spherical (or elliptical). In a 2D section, they are generally cataloged as closed pores and open pores. To design the ideal low *k* material, a spherical morphology with closed pores is preferred, as it can provide free volumes while maintaining the required connections[4].

To maintain a mechanically tough film, it is preferred that the pores be uniform in size and ordered within the film. The pore size is constrained by the size of the microelectronic devices and must be controlled down to diameter below 2 nm. Porosity is quantified as the ratio of free volume to the total bulk volume of material. Generally, a higher porosity is preferred.

The characterization of porosity and pore size can be achieved by both experimental measurement and mathematical modeling. Here, three measurement methods are given. First, porosity and pore size can be given by Barrett-Joyner-Halenda (BJH) pore size and volume analysis or by Brunauer-Emmett-Teller (BET) surface area analysis. Both of these two methods

are based on the measurement of gas adsorption and desorption. Second, the pore size can be precisely determined by transmission electron microscopy (TEM), if the pores are relatively uniform and ordered. Third, if the low k film is synthesized by a sol-gel process, Dynamic Light Scattering Analyzer (DLS) can be used as an indirect method to measure the micelle size.

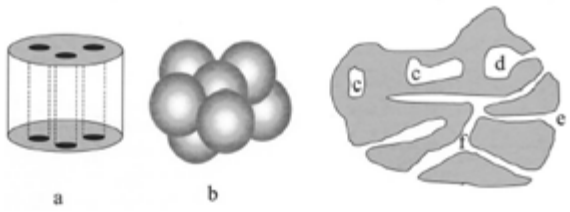


Figure 1.9 Summary of pore shape in 2D and 3D. (a) cylindrical pores, (b) sphere pores, (c) closed pores, (d) ink bottle shape pores, (e) funnel shape pores, (f) open pores. Reprinted with permission from [4].

***Effects of Carbon Bridges***

In the current research, carbon chains are typically used as bridges. The length of the chains influences porosity and pore size, which affect the dielectric constant and modulus. Longer carbon bridges are reported to lead to a smaller pore size and a higher porosity, as shown in Table 1.3.

A benzene-bridged organosilane is another option to be studied. Compared to linear bridged organosilane, it has large functional groups and a ring component in the structure. It is reported that benzene-bridged organosilane can form smaller pores and have a higher pore volume[12]. The electrical and mechanical properties of different bridging groups can be further studied to identify the effect of carbon bridges on the final properties.

Table 1.3 Pore sizes and porosity of the carbon-bridged materials[11].

| Carbon bridge type | BET surface area[$m^2$/g] | DFT pore size[nm] |
|---|---|---|
| Methylene | 815 | 2.97 |
| Ethylene | 862 | 2.63 |
| Hexylene | 892 | 2.19 |
| Octylene | 970 | 2.04 |

### *1.4 Laser Spike Annealing*

While porosity improves dielectric properties, it also damages the connectivity of the Si-O-Si network, resulting in deterioration of mechanical properties (decrease of Young's modulus, hardness and fracture toughness). This problem can be moderated by post thermal annealing, ultraviolet irradiation (UV treatment), electron bombardment (E-beam), and laser spike annealing (LSA). The heat treatment contributes to two aspects. First, it is hoped that this will initiate a reorganization of the Si-O-Si structure into the preferred network structure, and second, it can generate additional porosity by removing porogens.

LSA is a promising heat treatment due to its high power density and short heating time. However, the behavior of low *k* materials, annealed at high temperature for short time frames, needs to be studied in order to substantiate whether LSA is a viable method to use in the semiconductor industry as an effective method of improving the properties of the material.

#### *1.4.1 Classification of Post-Annealing Methods*

***Furnace Annealing***

Furnace annealing is a traditional method for heat treatment. Although convenient, its use is restricted because the curing temperature is limited to around 500 ℃ due to back-end metallization. At this low temperature, the energy is not sufficient to remove labile species in the porogens, and thus the final porosity is not adequate. Therefore, additional assistance is necessary via photon or electron bombardment to fully develop the porosity.

***E-beam Exposure***

The e-beam exposure is generated by a large area electron beam source. The beam energy, current and treatment dose can be controlled to provide various annealing conditions. It has been reported that e-beam exposure can significantly improve the modulus and fracture resistance[13].

However, this method, while effective, often leads to front-end device damages (gate oxide in the FET). The damage sensitivity to e-beam conditions has been studied[14]. Damage is not sensitive to the beam current, but the beam energy and dose play an important role. Moreover, the vacuum processing condition brings about additional challenges regarding efficiency[8]. These problems greatly limit the use of e-beam exposure.

***UV Treatment***

UV treatment uses a blanket ultraviolet exposure, in addition to thermal heating, to illuminate the entire wafer[8]. The processing variables include cure temperature, UV light output, cure time and cure pressure. It is reported a higher cure temperature, at a constant UV output within enough cure time, leads to a modulus improvement by 1.25 with a *k* value of 2.5[15]. However, several drawbacks limit implementation of UV cure in manufacturing. First, the UV cure suffers from exposure non-uniformity caused by the dependence of optical absorbance on surface structures[8]. Also, an *in situ* UV chamber clean is critical as removed organic species from porogens are deposited in the chamber[15].

LSA can push the temperature above the 500 ℃ limit for furnaces. Thus, LSA can solve most of the problems associated with a UV cure; for example, LSA does not require a chamber. As a promising technique, the principles and set-up of LSA are discussed in the next section.

### *1.4.2 Set-up and Principles of Laser Spike Annealing*

Laser-based millisecond spike annealing technique uses a line-focused continuous wave (CW) laser beam to scan across the sample and anneal an irradiated area. In this thesis, a far-infrared $CO_2$ gas laser was used.

***Set-up of LSA***

The $CO_2$ laser spike annealing system is composed of a 120 W $CO_2$ laser ($\lambda$=10.6 μm), two controlling shutters, an attenuator, two focusing lens, and a linear motion stage (Aerotech ES14663-1). The schematic of the $CO_2$ laser set-up is shown in Figure 1.10. The $CO_2$ laser is the energy source. The two shutters, a safety shutter and a process shutter, are used to control the processing. The polarizer-analyzer-attenuator, containing a series of ZnSe plates, is used to control the intensity of the laser (laser power) by changing the rotation angle. The linear motion stage controls the sample movement to achieve the scanning at speeds of up to 400 mm/s[17].

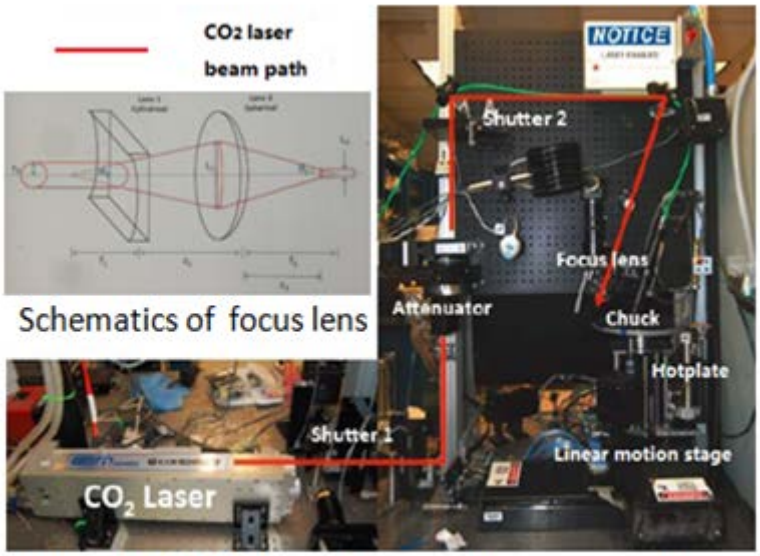


Figure 1.10 $CO_2$ laser spike annealing system and its beam path. Reprinted with permission from [16, 17].

To induce absorption of the $CO_2$ radiation samples are placed on a hotplate capable of reaching 400 ℃. The hotplate includes a vacuum chuck to hold the sample during experiments. Second, nitrogen flows over the top of the hotplate to protect the sample. A thermocouple is used to monitor the temperature of the hotplate.

The $CO_2$ laser is focused to a line beam using two focusing lens, as shown in Figure 1.10. The original $CO_2$ beam shape is circular with a 1.9±0.2 mm radius ($r_0$). The beam first enters a cylindrical lens with an effective focal length $f_1$. At this lens, it expands in certain axis with a half-angle $\theta_1$ of $r_0/ f_1$. After the expansion in a distance of $z_1$, a spherical lens focuses the asymmetric beam. Eventually, the beam is focused into a line with a full width half maximum (FWHM) of around 90 μm in the short axis (beam length) and a FWHM of around 588 μm in the long axis (beam width), as shown in Figure 1.11. The data are based on the laser power of 20 W and the scan speed of 100mm/s.

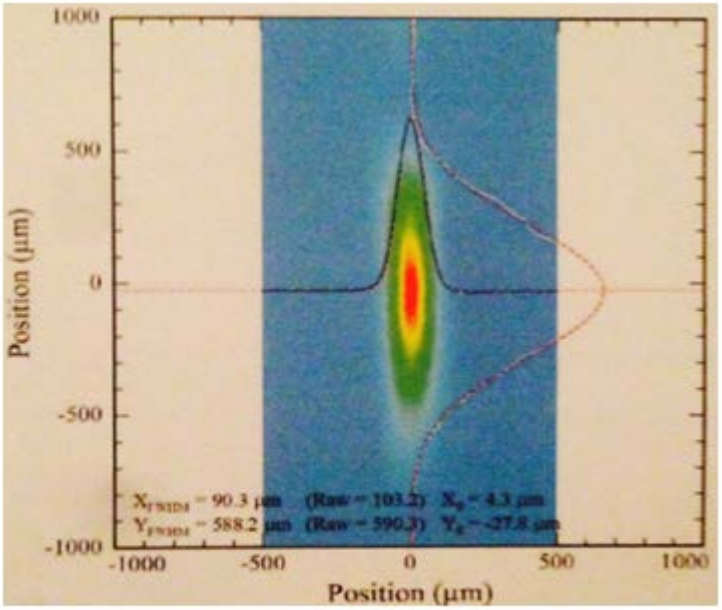


Figure 1.11 $CO_2$ laser beam intensity profile.
Reprinted with permission from [16, 17].

***Principles of Laser Scanning***

When a line-focused continuous wave (CW) laser beam scans across the sample, it rapidly heats the surface to the desired annealing temperature with the surface cools afterwards by thermal conduction into the substrate, as shown in Figure 1.12.

The annealing of low k materials is achieved by photon absorption in the underlying Si substrate; the thin dielectric is nearly transparent at the $CO_2$ laser wavelength.

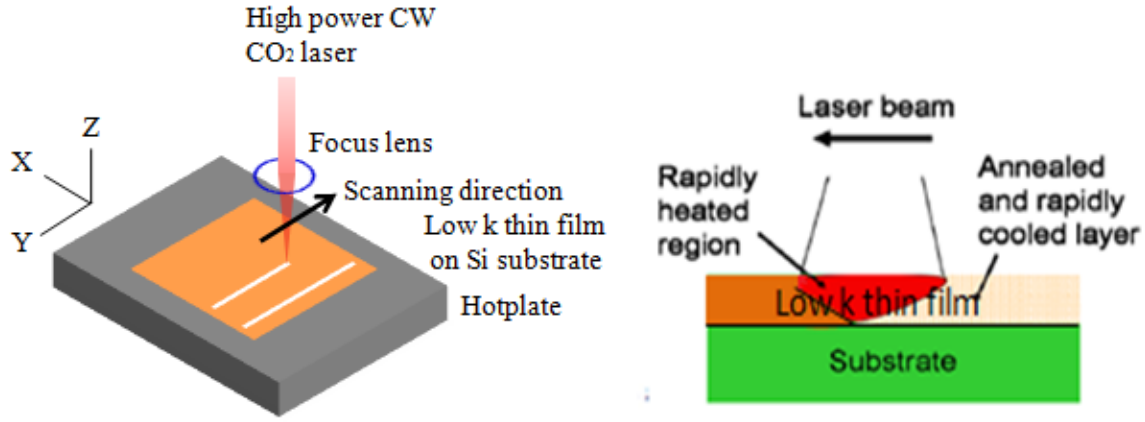


a) Schematic of laser scanning b) Cross-section view of laser scanning

Figure 1.12 Principles of laser scanning and annealing. Reprinted with permission from [17, 18].

***Parameters of LSA***

The annealing conditions by LSA are controlled by two primary parameters, laser power (temperature) and dwell time. In general, annealing temperatures can reach up to and beyond the silicon melting point of 1414 ℃. Laser dwell time can change from 0.01 ms to 10 ms.

Dwell time ($\tau_{dwell}$) is defined as the heating duration of laser beam at a position, given by

$$\tau_{dwell} = \frac{W}{v} \tag{1.10}$$

where W is defined as the FWHM (full width half maximum) of the laser beam in the short axis (direction of laser scanning), and v is the stage scan velocity. For a dwell time of 0.5 ms, with a beam width of 90 μm, a scan speed of 180 mm/s is required. In this thesis, dwell times of 0.5 ms, 1ms and 3ms were used, as summarized in Table 1.4.

Table 1.4 Summary of dwell times.

| Dwell Time[ms] | 0.5 | 1 | 3 |
|---|---|---|---|
| Scan Speed[mm/s] | 180 | 90 | 30 |

The temperature experimented by the sample is a two-dimensional position-related concept, and is determined by the laser power density. As shown in Figure 1.11 and 1.13, the beam intensity profile (power density) can be modeled as nearly Gaussian distributions. It is not a perfect Gaussian, due to optics contamination, refractive index gradients and the off-normal angle of the incident laser to the sample surface[19].

In the long axis of laser beam(the x-axis in laser scanning), the temperature distribution is defined as spatial temperature profile, as shown in Figure 1.13a. This spatial temperature profile, similar to beam intensity profile, is given by a Gaussian function, as

$$T_G(x|\sigma) = T_0 \exp[-\frac{(x)^2}{2\sigma^2}] \tag{1.11}$$

where x is the position relative to the beam center, $T_0$ is the beam center temperature, and σ is the standard deviation given by

$$\sigma = \frac{FWHM}{\sqrt{8\ln 2}} \approx \frac{FWHM}{2.35}. \tag{1.12}$$

The total laser power is given by the integral of the laser power density over the long axis. The laser power density, as shown in Figure 1.12, is given as

$$I_G(x|\sigma) = I_0 \exp[-\frac{(x)^2}{2\sigma^2}] \tag{1.13}$$

where $I_0$ is the maximum power density at the beam center and other parameters are the same with these in spatial temperature profile. The laser power is given as

$$P = \int_{-\infty}^{\infty} I(x)dx = \sqrt{2\pi}\sigma I_0. \tag{1.14}$$

Based on Equation 1.14, the laser power can be expressed as

$$P = (1.064)(FWHM) \cdot I_0 . \tag{1.15}$$

In the short axis of laser beam (the y-axis in laser scanning), the temperature varies with time as shown in Figure 1.13b. The temperature profile is not symmetric since the beam is scanning.

The profile can be interpreted as an *in situ* temperature profile during the laser scan. Positions ahead of the beam represents heating as the laser approaches, while positions behind the beam show cooling after the laser passes. The temperature starts increases approximately 2 ms prior the peak and begins cools almost immediately. After approximately 3 ms, the temperature returns to room temperature. The total heating duration is only 5 ms, leading to the spike annealing behavior.

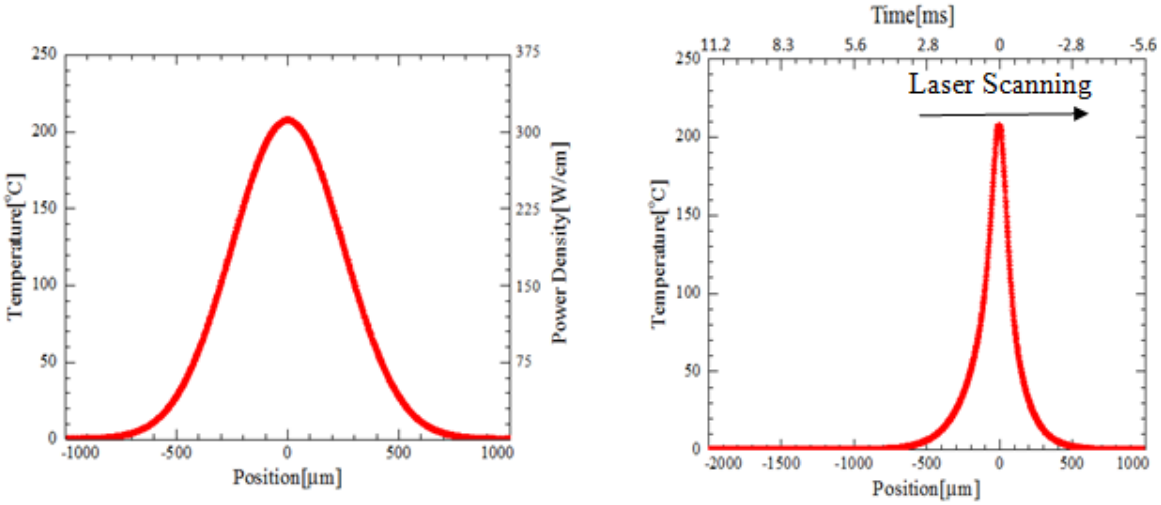


a) Spatial temperature profile and power density profile. b) Temporal temperature profile.

Figure 1.13 Temperature profiles under 20W power, 0.5ms dwell time and 588μm FWHM.

CHAPTER 2

# SAMPLE PREPARATION

## *2.1 Classification of Fabrication and Synthesis Methods*

Various methods have been used to fabricate low *k* thin films. These methods can be roughly classified into two categories, fabrication by thin film deposition and synthesis by chemical self-assembly. For thin film deposition, most physical vapor deposition (PVD) and chemical vapor deposition (CVD) methods have been attempted, including thermal evaporation, e-beam sputtering, ion sputtering, bias sputtering and plasma enhanced chemical vapor deposition (PECVD). For chemical self-assembly, sol-gel and spin-on assisted sol-gel processes are widely used.

### *Thin Film Deposition and PECVD*

While almost all the thin film techniques have succeeded in producing films, most have intrinsic disadvantages that keep them from being suitable for manufacturing. Thermally grown films form too slowly under the required temperature. For sputtering, the stoichimetric relation cannot be guaranteed and films tend to be contaminated in the chamber. For common CVD processes, precursors are hard to handle and step coverage is poor, because reactive intermediates can diffuse on the heated surface. To address this problem, PECVD, with a high-energy plasma, can facilitate the reactive intermediates to break chemical bonds and form stable products before they impact the deposition surface. Based on these reasons, PECVD has become the most popular method to fabricate low *k* films[1].

### *Sol-Gel Process and Spin On Process*

Unlike PECVD, sol-gel process control elemental compositions and bonding environments precisely by the precursor stoichiometry. Also, the process is simpler, much less expensive and

faster. A comparison of PECVD and sol-gel process is given in Table 2.1. Costs are based on rates at CCMR and CNF facilities at Cornell.

Table 2.1 Comparison of PECVD and sol-gel process.

| Method | Facility | Price | Estimated Time |
|---|---|---|---|
| PECVD | PECVD | $150/use | 1-2 hours |
| Spin-on assisted sol-gel process | Spin coater | $40/hour | 5 minutes |

### *2.2 Mechanisms of Sol-Gel Process*

Sol-gel processes generally follow a common set of processes. The sol solution is prepared under an acid or base catalyst. During aging of the sol solution, the gelation process begins. After aging, based on the difference in drying condition after aging, various products can be obtained, as shown in Figure 2.1. For one pathway (dashed red line), xerogels can be obtained by evaporation and aerogels by solvent extraction. These structures have extremely low densities, and hence are not discussed further. For the other pathway (solid red line), spin coating is used to accelerate the solvent evaporation and produce high quality films. The process is referred to as a spin-on assisted sol-gel process. After this process, a high quality dense thin film can be obtained.

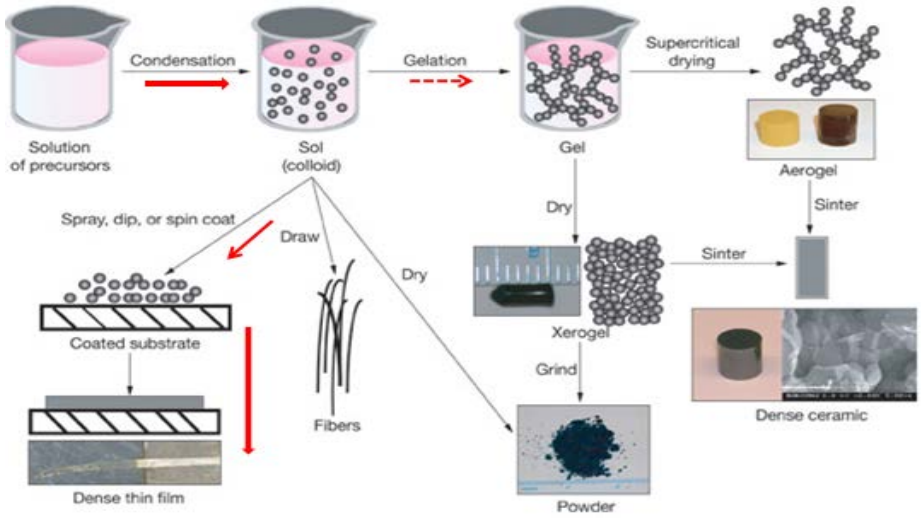


Figure 2.1 Summary of sol-gel products. Reprinted with permission from [20].

***Hydrolysis and Condensation***

The mechanism of the sol-gel synthesis is based on two reactions, hydrolysis and condensation. In this thesis, the precursor is an ethyl-bridged organosilane, BTESE (1,2-bis-(triethoxysilyl)ethane), as shown in Figure 2.2a.

The hydrolysis reaction (Figure 2.2b) can be catalyzed by either an acid or base. The hydroxyl group (-OH) continues to replace alkoxy group ($-OCH_2CH_3$) producing an alcohol. The Si-OH bonds in the hydrolysis become the reactants in the following condensation reaction.

With three products formed in the hydrolysis, several combinations of reactants can be involved in the condensation. The most straightforward reaction is given in Figure 2.2c. In this reaction, the introduced hydroxyl group (-OH) reacts with alkoxy group ($-OCH_2CH_3$) producing the alcohol. After this reaction, the desired Si-O-Si bond is built.

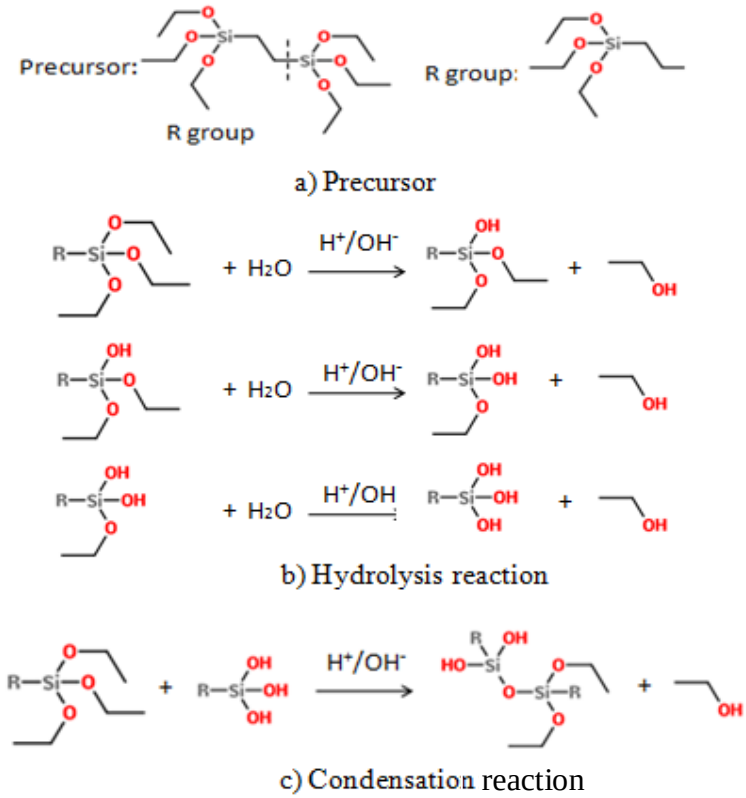


Figure 2.2 Hydrolysis and condensation reaction.

Four aspects have an effect on the sol-gel process.

- Acid catalyst effect
- Precursor substituent effect in hydrolysis
- Precursor substituent effect in condensation
- Hydrophobic effect

First, acid catalysts generate an open cross-linking structure while base catalysts tend to form a nanoparticle structure. Thus, acid catalysts were used in this thesis to obtain an open structure. Second, with the substitution from alkoxy group ($-OCH_2CH_3$) to hydroxyl group (-OH), the hydrolysis reaction slows down, since the alkoxy group is more electron donating than the hydroxyl group. Third, the first step in hydrolysis dominates the reaction initially, so its product will become the first reactant in the condensation. With a greater number of large alkoxy group in the first reactant, the open structure becomes dominant. Finally, since the ethoxy groups in the precursor are hydrophobic, alcohol-water co-solvents are necessary to make the solution miscible.

### *2.3 Porogens and Micelle*

Porogens are surfactants used in the sol gel process to form micelle initially which then decompose later to generate pores.

In this thesis, the porogen Brij-76 ($C_{18}H_{37}(OCH_2CH_2)_{10}OH$) was used. The formation of the micelle is shown in Figure 2.3a. This porogen has a hydrophilic end (-OH) and a hydrophobic end (long C-C and C-O chains). In certain water/alcohol ratio, the porogen can self assemble into nanoparticles with the hydrophilic ends outside and the hydrophobic ends inside. After high temperature annealing, the long hydrophobic alkyl and alkoxy chains inside the micelle can be removed creating nanopores. The size and number of the micelle is controlled by the

water/alcohol ratio, the porogen/precursor ratio, and the length of the carbon chains in the porogen.

The interaction between the micelle and the precursor is based on the hydrolysis reaction, as shown in Figure 2.3b. After the micelle is generated, Si atoms in the precursor attach to the micelle producing an alcohol. Based on this mechanism, the size of the nanopore is approximately the size of the micelle.

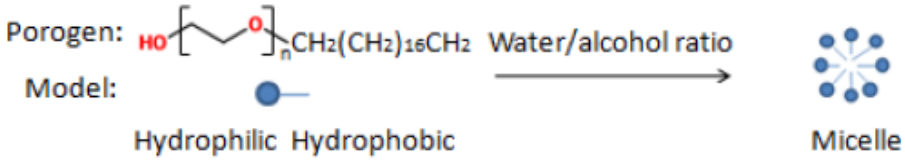


a) Formation of micelle by porogen

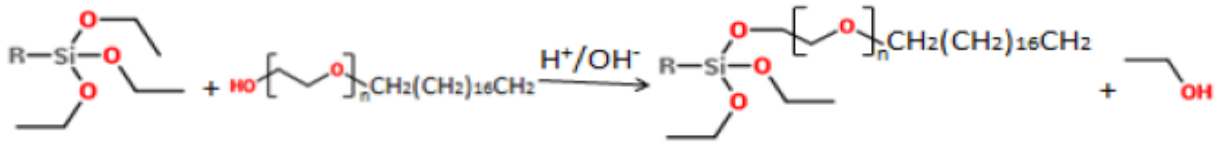


b) Condensation reaction of porogen with precursor

Figure 2.3 Formation of micelle and condensation reaction of porogen.

### *2.4 Procedures and Conditions for Synthesis*

The chemicals used in the synthesis are summarized in Table 2.2. All were purchased from Sigma-Aldrich.

Table 2.2 Summary of chemicals in the synthesis.

| | Precursor | Porogen | Solvent | Catalyst |
|---|---|---|---|---|
| Name | BTESE | Brij 76 | PMOH | Nitric Acid |
| Chemical Name | 1,2-bis-(triethoxysilyl)ethane | - | 2-Methoxy-1-propanol | - |
| Molecular Formula | In Figure 2.2a | In Figure 2.3a | 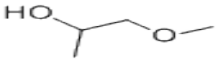 | $HNO_3$ |

Samples were prepared in five steps; preparation of reaction solutions, mixture of BTESE and porogen, addition of catalyst, standing (aging) and spin-coating, as shown in Figure 2.4. The

concentration of both BTESE and porogen was 25 wt.% in the PMOH solvent. 0.609 mL of 1 M nitric acid was added per gram of BTESE. The solution was left standing for 15 minutes. Finally, films were spun for 1.5 minutes at 2000 rpm.

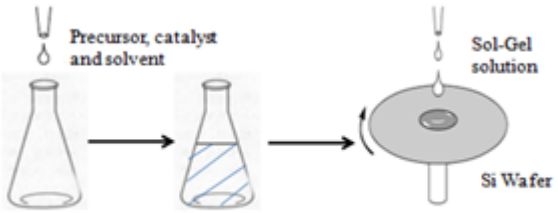


Figure 2.4 Procedure of spin-on assisted sol-gel process.

Several parameters were varied in the synthesis including the ratio of porogen to precursor, the ratio of water to alcohol (solvent), and the amount of acid (including pH value). Based on previous successful sol-gel synthesis[9,10,22], four samples with different conditions were explored, as given in Table 2.3. Sample A was the control group. Sample A and sample B differ in the amount of porogen/precursor ratio to compare the effect of porosity. Sample A and sample C differ in the amount of acid to compare the effect of catalyst. Sample D has an extra agitation step before standing, in order to check the effect of mixture condition on the product.

Table 2.3 Summary of sample conditions.

| | Porogen /Precursor Ratio | Acid Amount /1g precursor | Aging Type | Acid Conc. | Alcohol Ratio |
|---|---|---|---|---|---|
| Sample A | 21.5% | 0.609 mL | Standing | 1 M | Roughly Same |
| Sample B | 9.0% | 0.609 mL | Standing | | |
| Sample C | 21.5% | 0.456 mL | Standing | | |
| Sample D | 21.5% | 0.609 mL | Agitation +Standing | | |

Sample A and sample C failed to distinguish any acid influences on the synthesis, mostly likely because the change was not large enough. As shown in Figure 2.5, the FTIR spectrum of samples A and C show no distinct difference.

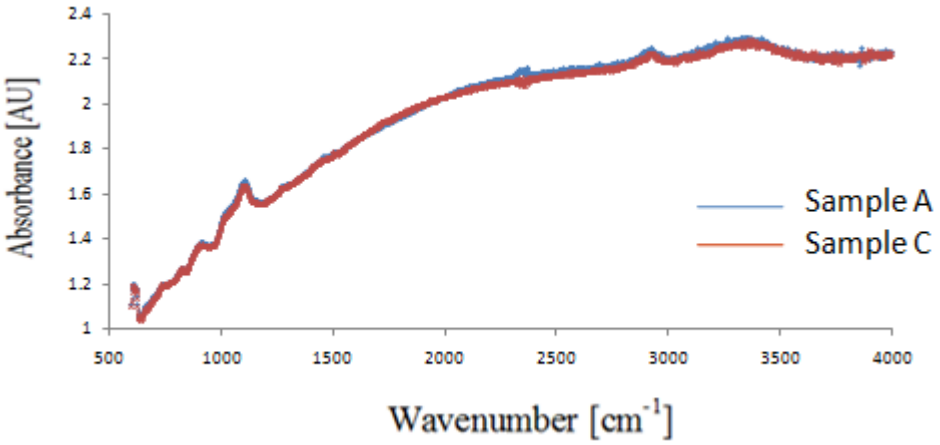


Figure 2.5 FTIR spectra of samples with different amount of acid catalyst.

Sample A and sample D show different appearances of sol solution, as shown in Figure 2.6. Sample A without agitation is layered with the water-based acid on the top and the alcohol-based precursor/porogen mixture on the bottom. This suggests that the sol-gel cross-linking occurs at the interface of these two layers. On the other hand, sample D with agitation shows turbidity which indicates the formation of particles. Such particles will likely have a negative effect on film uniformity and may lead to current leakage and crack growth or fracture.

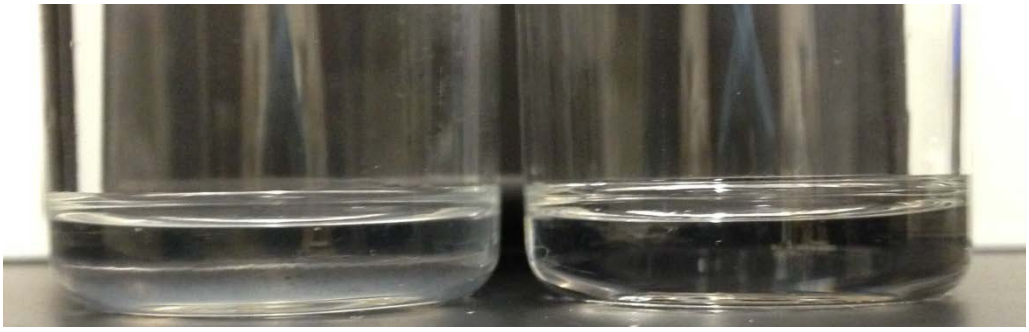

Sample D Sample A

Figure 2.6 Influence from agitation during the sol-gel process.

CHAPTER 3

# POST-THERMAL TREATMENT

## *3.1 Post-Thermal Treatment Procedures*

After deposition, low k films go through three steps of post thermal treatment, as shown in Figure 3.1. The purpose and processing conditions are given in this section. The effects of post thermal treatment on reactions and structural rearrangement are given in Chapter 5.

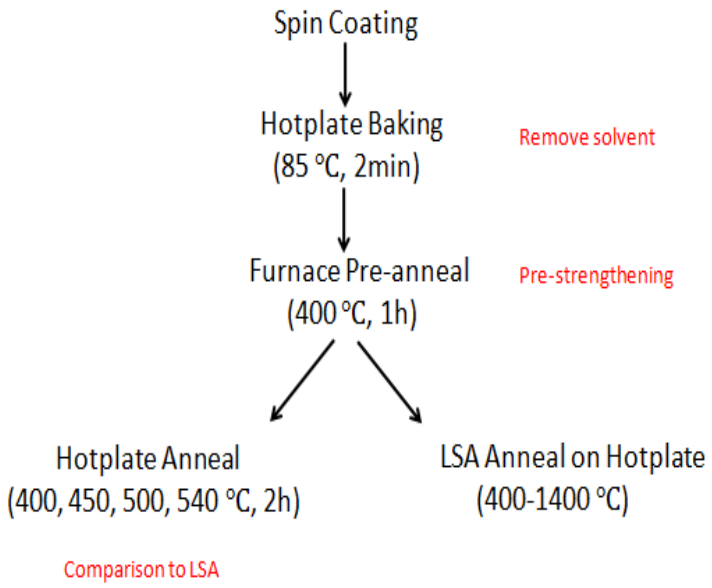


Figure 3.1 Heat treatment flow for low *k* films.

Immediately after spin coating, samples were annealed on a hotplate at 85 ℃ for 2 minutes. This step evaporated the remaining solvent and continue the sol-gel (condensation) reaction after spin coating.

Second, films were put into a furnace (YES Polymide Bake Oven) to cure at 400 ℃ for 1 hour. The curing profile is given as Figure 3.2. This step is to pre-cure. Without this cure, films were soluble in acetone and failed during subsequent photolithographic processing.

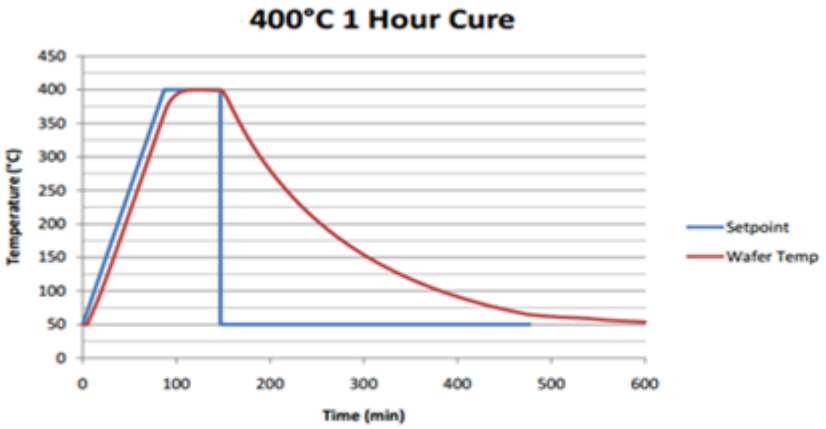


Figure 3.2 Furnace curing profile. Reprinted with permission from YES Polymide Bake Oven instruction in CNF.

Third, after curing at the lower temperature, the film was annealed either by LSA or by further hotplate annealing. This step is to rearrange the structure and to achieve the optimum annealing condition for desired properties.

Hotplate annealing conditions are summarized in Table 3.1. Four pieces of sample A were annealed under various temperature for sufficient time (2 hours) to allow maximum structural changes to be obtained.

Table 3.1 Summary of hotplate annealing conditions.

| Sample Number | AH1 | AH2 | AH3 | AH4 |
|---|---|---|---|---|
| Temperature | 540 ℃ | 500 ℃ | 450 ℃ | 400 ℃ |
| Time | 2 hours | | | |

### *3.2 Designing of LSA on Low k Materials*

#### *3.2.1 Assistance of Hotplate for LSA and Photon Absorption in Semiconductors*

LSA was conducted with the assistance of a hotplate, as shown in the LSA set-up (Figure 1.10). The hotplate was required since lightly-doped silicon wafers do not absorb the $CO_2$ laser at room

temperature. The heating of the low k films required photon absorption in the underlying silicon substrate, since the very thin dielectrics cannot absorb the $CO_2$ wavelength either.

First, the mechanism of photon absorption in semiconductors is discussed. The near-infrared light can be absorbed in the silicon mainly by two processes: electron transitions across the band gap from valence to conduction band (band to band absorption) and free carrier absorption by the excitation of electrons and holes into a higher energy status within the energy band[23].

The absorption and its mechanisms are affected by three parameters: temperature, doping concentration and photon energy of the incident light. First, the photon energy can influence the absorption in two situation. When it is smaller than the band gap, the band to band absorption cannot proceed and the absorbance will be extremely small for an intrinsic semiconductor. With increase of photon energy, a dramatic increase of the absorbance is observed as shown in Figure 3.3. Second, Figure 3.3 also shows that the temperature can increase the absorption in two ways. On one hand, deduced by Fermi-Dirac statistics, the intrinsic carrier density increases with the temperature as

$$\ln(n_i) = \text{constant} + \frac{3}{2}\ln kT - \frac{\varepsilon_g}{2kT} \tag{3.1}$$

where $n_i$ is the intrinsic carrier density, T is the temperature, $\varepsilon_g$ is the band gap energy and k is the Boltzmann constant. Thus, the free carrier mechanism can be enhanced by a higher temperature. On the other hand, the indirect transition of silicon requires a phonon absorption(or emission), so the band to band mechanism can be increased strongly with temperature. For doped silicon, an increased temperature can also increase this mechanism by reducing the band gap. Third, a higher doping concentration can decrease the band gap and increase the density of free carriers by increasing the Fermi energy level and changing the band structure. As a result, both

mechanisms are enhanced. Also, the doping level changes the behaviors under increasing temperature, as shown later in Figure 3.4.

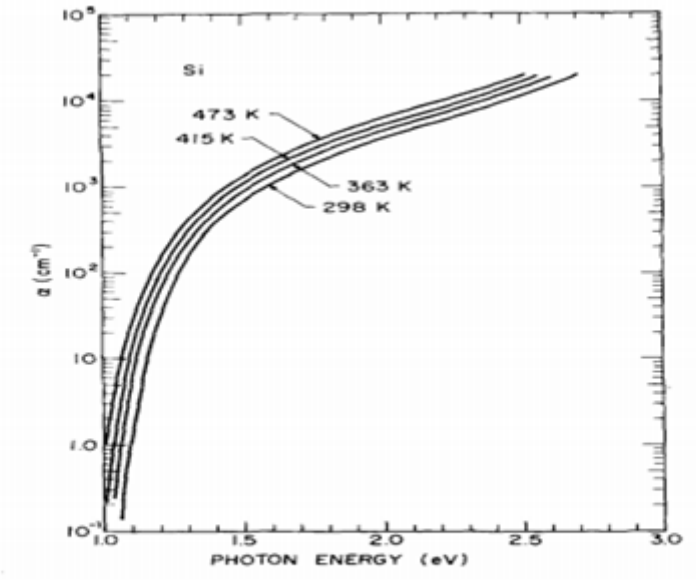


Figure. 3.3 Photon energy dependence and temperature dependence of absorbance in near IR region. Reprinted permission from[23]

In this thesis, a lightly-doped n-type silicon wafer with a doping concentration of $9\times10^{14}$ $cm^{-3}$ was used as the substrate for low *k* films. At room temperature, this carrier density is insufficient for free carrier absorption. Temperature must be used to increase the intrinsic carrier concentration to induce photon absorption. It is noted that a heavily-doped silicon wafer was not chosen as a substrate, because the carriers would interfere in the FTIR characterization.

The absorbance (α) model of lightly-doped silicon and heavily-doped silicon is shown in Figure 3.4a. The lightly-doped silicon is transparent under around 300 ℃ and its absorbance increase as a linear function with temperature afterward. The heavily-doped silicon keeps a high absorbance under around 450 ℃ due to the initial carrier density, and its absorbance increases at higher temperatures as the same linear function as shown in the lightly-doped silicon (Figure

3.4b). This model has a fit with the data of transmission analysis for different doped silicon, which is defined as

$$T = e^{-\alpha d} \tag{3.2}$$

where T is the normalized transmission, α is the absorbance and d is the wafer thickness(500 nm).

The temperature of the hotplate was set at 400 ℃, which generates an intrinsic carrier concentration of approximately $2.4 \times 10^{15}$ $cm^{-3}$. LSA samples include an additional hotplate annealing time of approximately 10-20 minutes due to sample set-up and alignment.

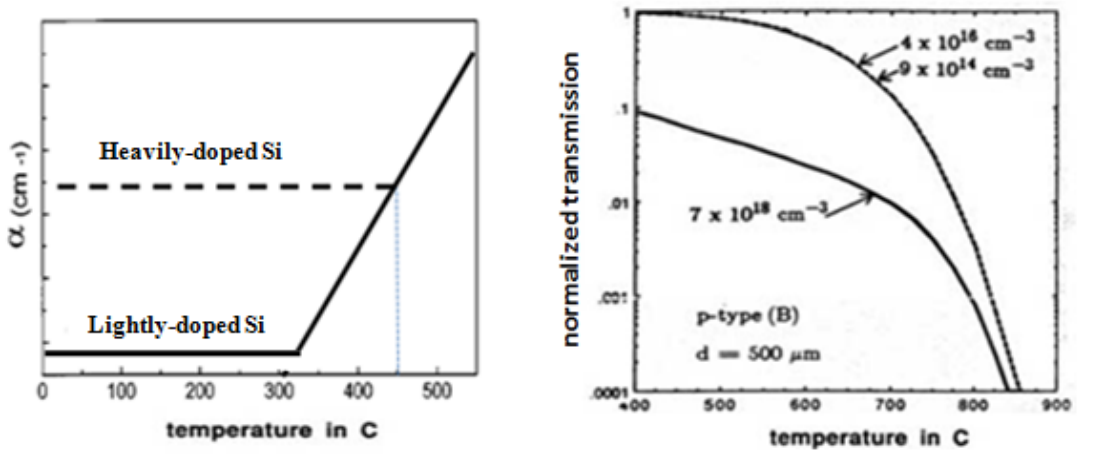


a) Absorbance model of temperature dependence for different doping level.

b) Transmission data of temperature dependence of different doping level.

Figure 3.4 Doping concentration influence on temperature dependence of absorbance. Reprinted with permission from[23].

### *3.2.2 LSA Condition Design: Laser Temperature and Dwell Time*

Laser temperature and dwell time in LSA are critical to achieve the optimum annealing conditions. Both parameters were explored in these experiments. Different dwell times were achieved by multiple LSA scans on the same sample, eliminating many potential systematic errors allowing for a better comparison. A continuous temperature change was obtained across a

single laser scan based on the spatial temperature profile as shown in Figure 3.5. Temperatures as a function of position are related to the maximum temperature at the laser beam center.

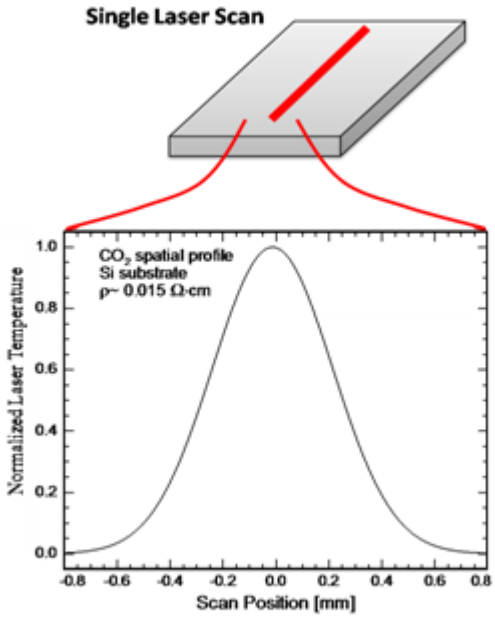


Figure 3.5 Normalized spatial temperature profile laterally across the beam for a single laser scan.

The LSA scanning design is represented in Figure 3.6, and the annealing conditions are summarized in Table 3.2. The porous sample (sample A) and the dense sample (sample B) were annealed under LSA using the same conditions. The sample size was 20 mm by 20 mm, allowing for six scans with a spacing of 3 mm between scans. The first five scans (scan 1-scan 5) were annealed at different dwell times under the same expected maximum temperature (1100 ℃), ranging from a short dwell of 0.5 ms to a long dwell of 3 ms. The last scan (6) remained unirradiated (blank) as a reference. The total annealing temperature is the sum of laser-induced temperature change and the hotplate temperature (400 ℃). Consequently, the laser power was adjusted for a 700 ℃ jump. The scanning length ideally would be 18 mm or more, ensuring a uniform area for the 12 mm long metal contacts used in the capacitance measurement. This

length also helped to visually distinguish the laser scan positions. Laser scans were aligned precisely to alignment marks on the sample using the *in-situ* camera.

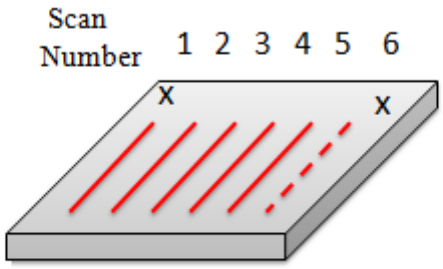


Figure 3.6 Schematic of multiple laser scans on one sample.

The laser maximum temperature is determined by the laser power, and is a function of the dwell time. For a short dwell, a higher power is required to reach the same temperature as that of a long dwell. The relationship of laser power to temperature as a function of the dwell was obtained from Byungki Jung[17]. The chosen laser powers were based on this relationship. However, it was found that the actual annealing temperature did not match the calculated temperature in the given temperature profile, due to non-linear effects introduced by the hotplate. Therefore, an absolute temperature calibration, based on the samples in this thesis was developed and is discussed in next section.

Table 3.2 Summary of LSA conditions for the porous sample (A) and the dense sample (B).

| Sample Number | AL1/BL1 | AL2/BL2 | AL3/BL3 | AL4/BL4 | AL5/BL5 | AL6/BL6 |
|---|---|---|---|---|---|---|
| Scan Number | 1 | 2 | 3 | 4 | 5 | 6 |
| Dwell Time | 3 ms | 1.5 ms | 1 ms | 0.75 ms | 0.5 ms | No Laser |
| Laser Power | 32.2 W | 36.1 W | 38.6 W | 40.4 W | 43.2 W | |
| Expected Maximum Laser Temperature | 700℃ | | | | | |
| Best Estimates of Maximum Laser Temperature | 1062 ℃ | 1012 ℃ | 1021 ℃ | 1002 ℃ | 1012 ℃ | |
| Hotplate Temperature | 400 ℃ (Actually 398-400 ℃) | | | | | |
| Expected Total Annealing Temperature | 1100℃ | | | | | 400 ℃ |
| Best Estimates of Annealing Temperature | 1462 ℃ | 1412 ℃ | 1421 ℃ | 1402 ℃ | 1412 ℃ | 400 ℃ |

### *3.3 $CO_2$ Laser Temperature Calibration*

Differences between the conditions that Byungki Jung used for the initial laser temperature calibration, and the actual conditions of these experiments, are summarized in Table 3.3. The primary differences are the concentration of dopants in the substrate, and the initial substrate temperatures.

Table 3.3 Differences of conditions for Jung's calibration and current experiments.

| Experimental Conditions | Jung's Calibration | Current Experiments |
|---|---|---|
| Substrate Type | Heavily-doped n type Si | Lightly-doped n type Si |
| Films on Substrate | None | Low k Film |
| Initial Temperature | Room temperature(25 ℃) | Hotplate heating(350 ℃-400 ℃) |
| Temperature Calibration Methods | Thermistor<br>Gold melting<br>Simulation | Gold melting<br>Simulation |

#### *3.3.1 Absolute Calibration*

To establish absolute temperatures for a given dwell time, a procedure based on the melting of gold was used as shown in Figure 3.7. Several lines of gold dots, with a diameter of 3 μm and a center to center spacing of 10 μm, were deposited on a low k film and patterned photolithographically. A single $CO_2$ laser scan at a given dwell time and laser power (above the gold melt threshold) was performed with the sample on the hotplate at 370 ℃. The scan direction was normal to the gold dot line. Due to the Gaussian-like temperature profile, gold dots melt from the center of the beam, to the point where the temperature drops to the gold melt point (1063 ℃). This corresponds to the laser temperature reaching 693 ℃ after correction for the hotplate temperature. Thus, one absolute point (L, 693 ℃) is obtained on the Gaussian distribution where L is the distance from the laser center to the point where the temperature reaches 693 ℃. This distance was determined by counting the number of melted gold dots (N) as

$$L = \frac{(N-1)\times 10\ \mu m}{2} = 5N - 5\ \mu m \tag{3.3}$$

The Gaussian function of the laser spatial temperature distribution is given by

$$T(x|\ \sigma) = T_0\ \exp[-\frac{(x)^2}{2\sigma^2}], \tag{3.4}$$

where $T_0$ is the laser maximum temperature and the standard deviation δ is given by FWHM of 588 μm as

$$\sigma = \frac{FWHM}{\sqrt{(8\ln 2)}} \approx \frac{588\ \mu m}{2.35} = 250\ \mu m\ . \tag{3.5}$$

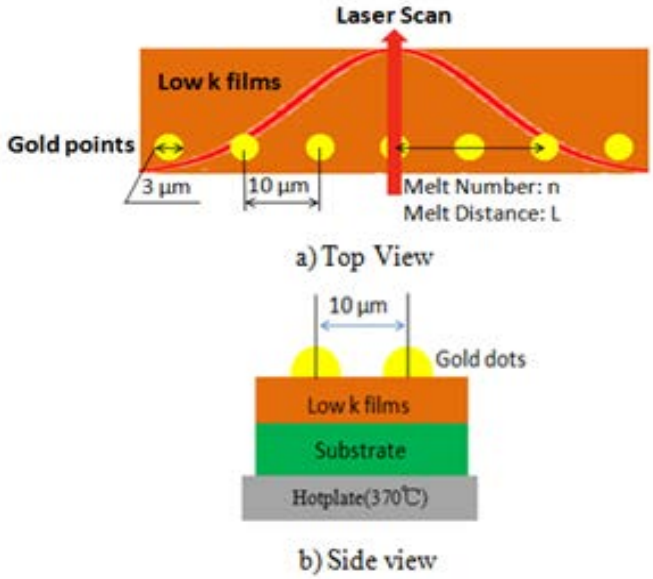


Figure 3.7 Schematic of laser temperature calibration.

The gold dot melt tracks can be unambiguously indentified using bright field optical and dark field optical microscopy, as shown in Figure 3.8. As the laser temperature reaches the threshold for gold melt, the molten dot contracts into several drops. Partially melted dots on the edge were counted only when more than half of the gold dot lines exhibited such behavior; otherwise they were treated as fluctuation of the laser power during LSA.

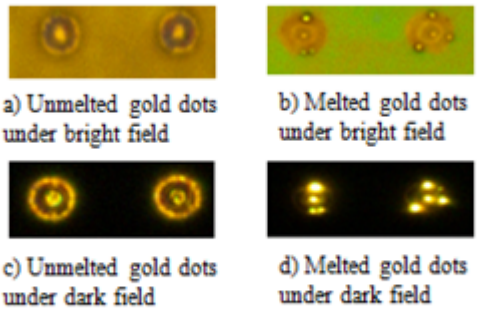


Figure 3.8 Optical images of unmelted gold dots and melted gold dots.

### *3.3.2 Simulation*

To confirm the accuracy of the temperature calibrations, laser temperature simulations were conducted as a comparison. The Cornell Laser Annealing Simulation Package (CLASP), developed by M. O. Thompson, P. Clancy and K. Iyengar, was used[16].

Parameters are summarized in Table 3.4. First, the initial temperature was set at 298 K (25 ℃, room temperature) and 643 K (370 ℃, hotplate). Second, the dwell time was determined by the scanning speed as given in Table 1.4. The silicon substrate concentration was set as the same as $4.0\times10^{18}$ $cm^{-3}$, with the assumption that the lightly-doped silicon after hotplate heating reaches the same carrier density as the heavily doped silicon. The simulation is only a 2D model assuming an infinitely wide beam (long axis). To determine the equivalent line beam power corresponding to the peak laser intensity, Equation 1.16 was used. The laser power is the integral of the line power density over the long axis. For a beam FWHM in long axis, the maximum power density $I_0$ as a function of laser power P is given by

$$I_0 = \frac{P}{1.06 \cdot FWHM}. \tag{3.6}$$

The calculated maximum line power density for a given laser power is shown in Table 3.5.

Table 3.4 Summary of parameters for laser temperature simulation.

| Laser Parameter | Laser Wavelength | Beam FWHM in short axis | Beam FWHM in long axis |
|---|---|---|---|
| Value | 10.6 μm | 90 μm | 588 μm |
| Substrate Parameter | Substrate Initial Temperature | Scanning Velocity | Substrate Concentration |
| Value | 298 K or 643 K | Table 1.4 | $4.0\times10^{18}$ $cm^{-3}$ |

### *3.3.3 Result Discussion*

Calibration results are summarized in Table 3.5 and Figure 3.9. Errors in the absolute calibration arises from three aspects. First, the beam FWHM is assumed to be 588 μm (20 W, 0.25 ms) for all laser powers and dwell times. In practice, the beam FWHM is slightly larger for higher laser powers and longer dwell times. As a result, the calculated laser maximum temperature by absolute calibration would be greater. Second, the absolute temperature (1064 ℃) might fall between two gold dots, and thus, the calculated laser maximum temperature by absolute calibration would be smaller. Third, any misidentification of melted gold dots adds to the errors. In this thesis, the error bar for laser temperatures was estimated by varying the counted number of melted gold dots (by ±1).

Table 3.5 Summary of laser power and laser maximum temperature.

| Dwell Time [ms] | 3 | | | 1 | | | 0.5 | | | |
|---|---|---|---|---|---|---|---|---|---|---|
| Power [W] | 36 | 38 | 40 | 40 | 42 | 44 | 48 | 50 | 52 | 54 |
| Laser Maximum Power Density[W/cm] | 575 | 607 | 639 | 639 | 671 | 703 | 767 | 799 | 831 | 863 |
| Laser Maximum Temperature by Simulation[℃] | 1204 | 1273 | 1340 | 1077 | 1114 | 1170 | 1164 | 1213 | 1262 | 1310 |
| Laser Maximum Temperature by Absolute Calibration[℃] | 1207 | 1297 | 1362 | 1082 | 1128 | 1180 | 1154 | 1207 | 1265 | 1328 |

Figure 3.9 compares the experiments, absolute calibration and simulations. There is an excellent match for dwell times at 0.5 ms, 1 ms and 3 ms, with differences less than 2%. The relationship between laser power (P) and laser maximum temperature ($T_0$) is approximately linear over a reasonable power range. The laser maximum temperature used for LSA can thus be calculated by these linear relations.

Under 0.5 ms, the linear relation for total temperature above 1000 ℃ is

$$T_0 = 29.0\ P - 240 \tag{3.7}$$

Under 1 ms, the linear relation for total temperature above 1000 ℃ is

$$T_0 = 30.0\ P - 137 \tag{3.8}$$

Under 3 ms, the linear relation for total temperature above 1000 ℃ is

$$T_0 = 38.8\ P - 187 \tag{3.9}$$

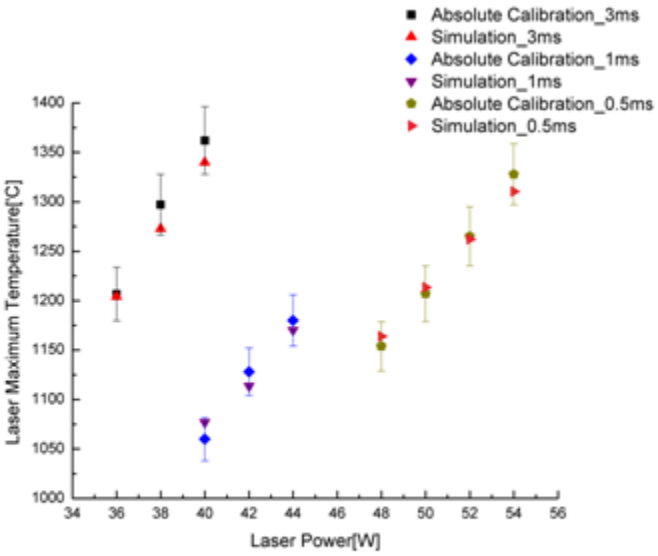


Figure 3.9 Relation of laser power and laser maximum temperature, using absolute calibration and simulation under 0.5ms, 1ms and 3ms.

Based on these relations, the best estimate for the maximum laser temperatures were calculated and are shown in Table 3.2. The peak temperature at a given power is a strong

function of dwell time. For example, Figure 3.10 shows the laser maximum temperature as a function of the dwell time for a laser power of 40 W. The temperature is normalized to value at $\tau_{dwell}$ =1 ms. The different slope above and below 1 ms is due to the "thermally thin" substrate phenomenon. The thermal diffusion length for cooling is about 560 μm for 1 ms dwell time, which is comparable to the silicon wafer thickness of 525 μm[17]. For dwell times greater than 1ms, the finite silicon wafer thickness and the nature of the wafer/hotplate interface influence the LSA behavior.

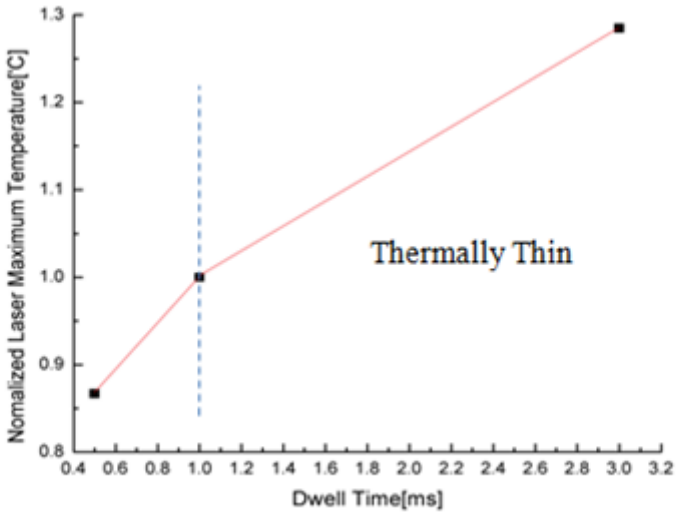


Figure 3.10 Relation of normalized laser maximum temperature and dwell time.

Based on the curves in Figure 3.10, the laser maximum temperature for 0.75 ms and 1.5 ms were estimated with results, as shown in Table 3.2.

In the "Thermally Thick" region ($\tau_{dwell}$ < 1 ms), the relation is

$$T_{relative} = 0.265\ \tau_{dwell} + 0.734, \quad (3.10)$$

and in the 'Thermally Thin' region($\tau_{dwell}$>1 ms), the relation is

$$T_{relative} = 0.142\ \tau_{dwell} + 0.857. \quad (3.11)$$

Thus, the laser maximum temperature for various dwell times can be obtained from the temperature calibration at a dwell of 1ms and the relative factor $T_{relative}$.

The absolute calibration for samples laser-annealed without a hotplate was done for dwell times at 0.5 ms, 1 ms and 3 ms. The laser powers were as high as 58 W for 0.5 ms, 52 W for 1 ms and 46 W for 3 ms. For all the cases, no melted got dots were observed by optical microscopy. This behavior conforms the necessity for using a hotplate during LSA to improve the photon absorption.

### *3.3.4 Comparison of Existing and Current Laser Temperature Calibration*

The comparison between the previous and the current laser temperature calibration is shown in Figure 3.11. The laser maximum temperature with the hotplate is about 150-300 ℃ higher than that at room temperature for both absolute calibration and simulation. This behavior is a result of the different temperature gradient during the thermal conduction. With an increase of laser power at a constant dwell time, the difference of laser temperature between the hotplate and room temperature conditions, becomes smaller. This is expected since the influence from the temperature gradient becomes smaller as the laser temperature is increased. It can also be estimated that with an increase of dwell time under a constant laser power, the difference of laser temperature again becomes smaller for the same reason.

This temperature difference may be due to two reasons: different carrier density and different temperature gradients. Heavily-doped silicon at room temperature has a slightly higher absorbance than the lightly-doped silicon at 400 ℃. This would result in a higher heating temperature for the heavily-doped silicon. However, the experimental results contradict with this model. Consequently, the initial temperature difference must have a significant effect, due to the

difference of thermal conduction during cooling. Figure 3.12 shows that cooling on the hotplate exhibits a distinctive delay compared to sample, cooled on a holder at room temperature.

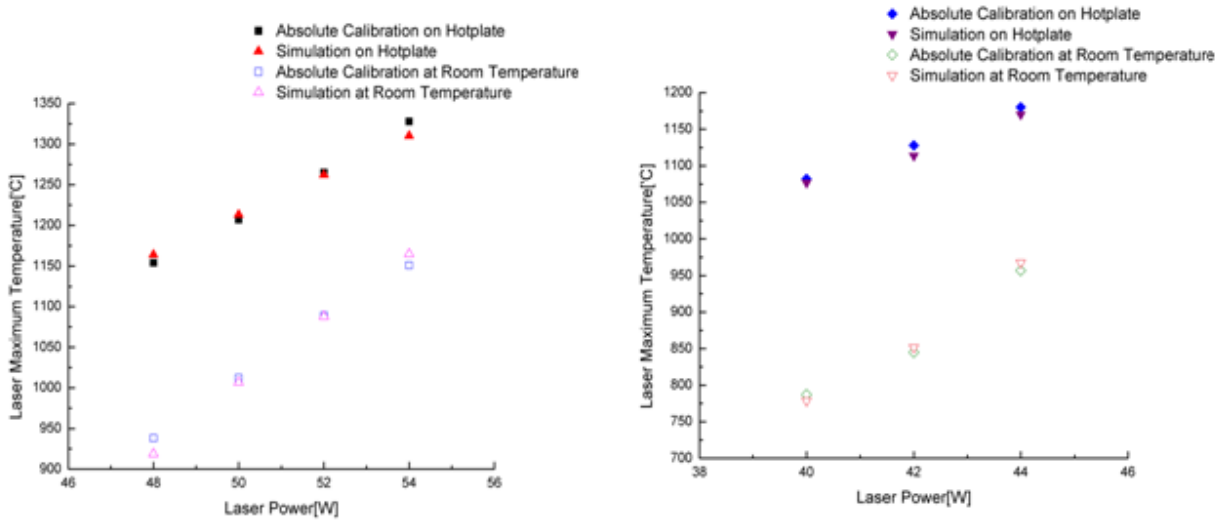


Figure 3.11 Comparison of existed and current laser temperature calibration by absolute calibration and simulation.

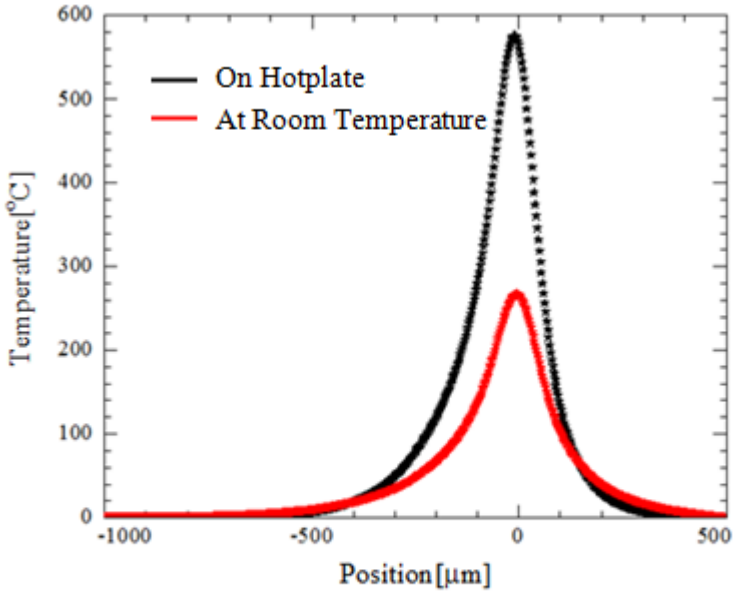


Figure 3.12 Comparison between temporal temperature profiles on hotplate and at room temperature(48W, 0.5ms).

CHAPTER 4

# CHARACTERIZATION AND TESTING

In this thesis, three major properties were explored: chemical properties, dielectric properties and mechanical properties. Chemical and structural properties are characterized by Fourier transform infrared spectroscopy (FTIR), Raman spectroscopy and X-ray photoelectron spectroscopy (XPS). Optical properties and thicknesses were measured by ellipsometry and profilometry. Capacitance was determined using C-V measurement with the dielectric constant calculated from measured capacitances and thicknesses. Finally, images were obtained by optical microscopy and mechanical properties ( modulus) were determined using nano-indentation.

## *4.1 Chemical and Structural Characterization*

Chemical and structural characterization of films after synthesis and after heat treatment provide a microscopic connection between structural information and measured properties. These data are used to establish how processes affect the final properties.

FTIR, Raman and XPS can be understood as the response of materials exposed to light with different wavelengths. In the spectrum shown in Figure 4.1, FTIR is in the IR range, Raman is in the UV-Vis range and XPS is in the X-ray range.

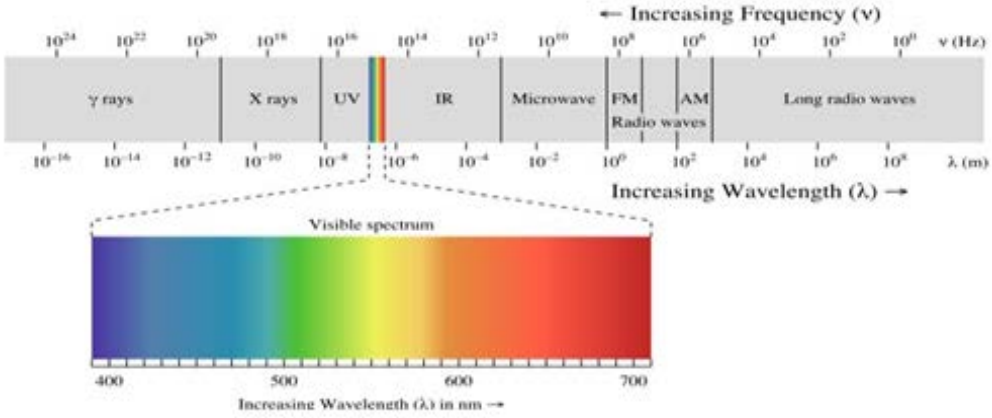


Figure 4.1 Light Spectrum.

### *4.1.1 Comparison of FTIR Spectroscopy and Raman Spectroscopy*

FTIR and Raman both measure nearly the same range of bond vibrational frequency (around 400-4000 $cm^{-1}$ wavenumber), but are sensitive to different chemical bonds because of their differing mechanisms and selection rules[26].

FTIR is based on photon energy absorption under IR light (2.5 μm-15 μm), while Raman is based on inelastic scattering under UV-Vis light (488 nm in this thesis). Under FTIR, molecules absorb a photon of light and directly excite into a higher vibrational state, resulting in the attenuation of the light source[27]. Accordingly, the characteristic frequency for FTIR is determined by the difference between vibrational energy states of the molecule. For Raman, the incident light source is at a much higher energy (compared to molecule vibrations), and thus is more appropriately referred to as the scattering phenomenon. As shown in Figure 4.2, rather than elastic Rayleigh scattering, Stokes Raman scattering shifts the scattered photon by a characteristic frequency, which is determined by the shifting of the vibrational state.

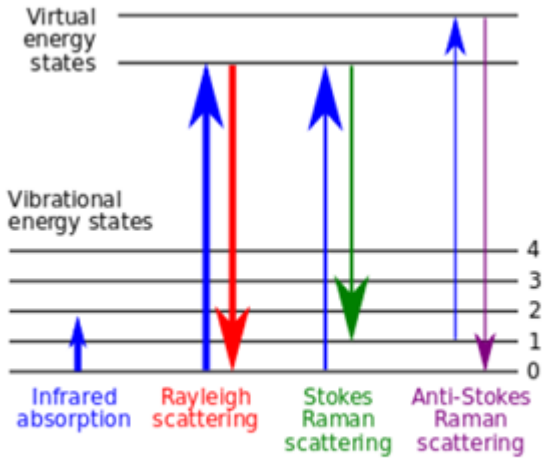


Figure 4.2 Mechanisms of infrared absorption and Raman scattering. Reprinted with permission from [26].

For selection rules, FTIR is sensitive to the changes of dipole moments, while Raman is sensitive to the changes of polarizability. So, asymmetric vibration and polar bonds with

permanent dipole moments are usually measured by FTIR, while symmetric vibration and non-polar bonds, such as C-C bond, are usually studied by Raman. Both tools are used in this thesis to provide a full picture of the structure in low *k* materials.

The vibrational modes includes stretching (changing bond length) and bending (changing bond angle). Generally, stretching has a higher energy change than bending, so stretch modes are easier to observe. In this thesis, all vibrations are these stretch modes.

The stretching characteristic frequency of a bond can be roughly determined by Hooke's Law, given as

$$\nu = \frac{1}{2\pi}\sqrt{k \cdot \frac{m_1+m_2}{m_1 m_2}} \tag{4.1}$$

where k is the spring constant of bond, and $m_1$ and $m_2$ are the masses of the atoms. This frequency is translated into wave number for a reasonable scale in the figure, given as

$$\tilde{\nu} = \frac{1}{\lambda} = \frac{1}{2\pi c}\sqrt{k \cdot \frac{m_1+m_2}{m_1 m_2}} \tag{4.2}$$

where λ is the wavelength and c is the speed of light.

### *4.1.2 FTIR Spectroscopy*

A Bruker Hyperion FTIR Spectrometer in the CCMR facility was used for all measurements. This instrument has a shift resolution of 4 $cm^{-1}$ and a spatial resolution of 20 μm. To decrease the noise, 100 scans were used for all spectra. The noise is approximately proportional to the square root of the number of scans.

FTIR was used in two ways. For exploring the synthesis process, samples, as deposited, after furnace pre-anneal and after LSA, were measured. As reference, samples of bare silicon wafers and pure porogen were also tested.

For exploring the effect of LSA, FTIR mapping with a resolution of 25 μm was done in a distance up to 2125 μm across a laser scan. Shown in Figure 4.3, the mapping (for both FTIR and Raman) refers to multiple measurements in an auto motion across the sample. By alignment and positioning, the structural information during mapping is correlated to temperature (the spatial temperature profile), dielectric constant and modulus. For comparison, samples annealed by hotplate alone were also characterized by FTIR.

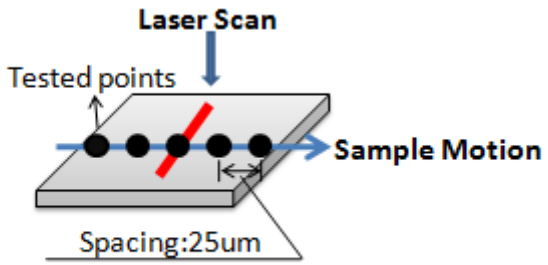


Figure 4.3 Schematic of mapping (FTIR or Raman).

### *4.1.3 Raman Spectroscopy*

For Raman measurements, the Renishaw Raman Spectroscopy in the CCMR facilities was used. Laser sources at 488 nm and 785 nm were explored. The wavelength of the incident light, although it does not impact the Raman shift, does affect the laser energy and detection depth. Preliminary tests showed that the 785 nm laser source did not exhibit distinct peaks, while the 488 nm laser source provided more information due to the smaller penetration depth. This reduced the influence from the silicon wafer, while also having a higher sensitivity due to a higher energy. Another parameter is the laser power, which relates to the signal/noise ratio and the sensitivity. A longer exposure time and accumulations can also improve the signal/noise ratio, but it increases the possibility of decomposition and also increases the required time. From preliminary tests, a power setting of 50% with 5 accumulations for 20 seconds each using 488 nm laser was chosen as the default condition.

Though effective, the 488 nm laser leads to a strong background due to fluorescence, as shown in Figure 4.4a. Because the excitation energy is high, the vibrational level can jump into the excited electronic state rather than the virtual electronic state in Raman scattering, as shown in Figure 4.4b. The background must be subtracted to obtain the actual value of peaks.

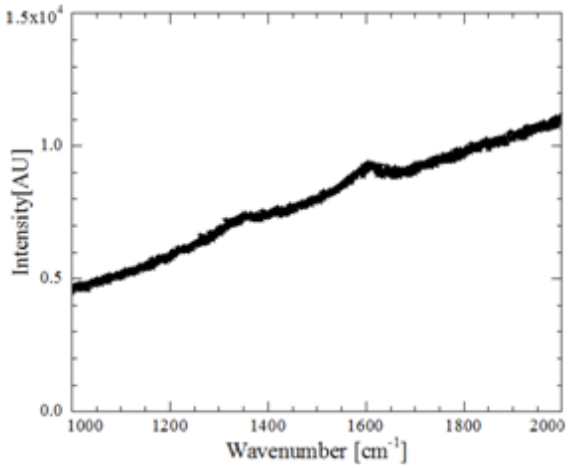


a) Background in Raman spectrum due to fluorescence

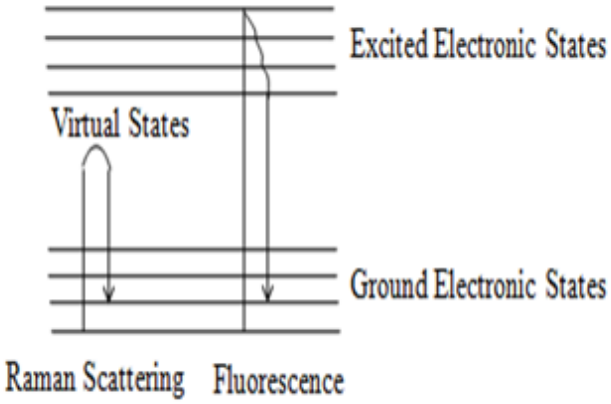


b) Comparison of excitation modes between Raman scattering and fluorescence

Figure 4.4 Fluorescence phenomenon and physical origin.

One method for background subtraction is to model the background as a function of wavenumber. This requires that the background be the same for all the samples, or to change only slowly. The average intensity of the background was found to vary along the scan position as shown in Figure 4.5a. This curve was fit to a cubic polynomial to normalize all spectra to an equal intensity. This change is thought to arise from a focus shift during scanning. This was confirmed by measuring the Raman intensity as a function of the focus error as shown in Figure 4.5b. After the background was modeled, it was removed from the spectrum allowing analysis of the actual peaks. However, the results showed that peaks remained obscured by the noise of the high fluorescence signal. The background shape of spectrum in the Raman mapping was not consistent and the peak signal not distinct enough to stand out above the noise.

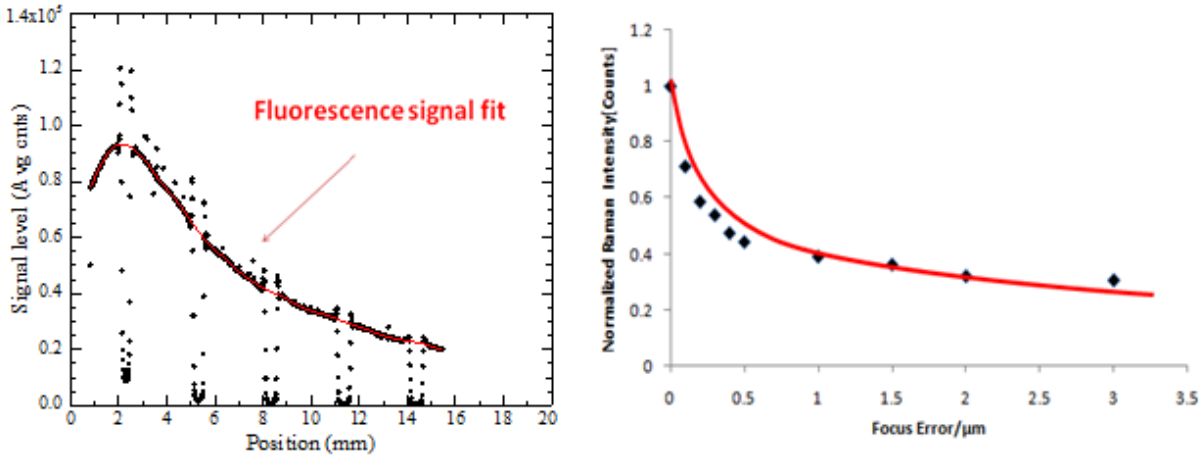


a) Signal level of background in Raman mapping (Fitting part from Prof. M. O. Thompson).

b) Intensity change as a function of the focus position.

Figure 4.5 Signal level of background as a function of the focus position.

Another method for background subtraction is a rolling-circle filter, as shown in Figure 4.6a[28]. By subtracting the value in the tangential point of the spectrum and the inside circle, the background can be removed, without considering the background shape. One important parameter is the circle radius. A circle of small radius is strongly affected by the spectrum noise, while a circle of large radius misleads the analysis of the peaks. Preliminary tests shown that a circle with a radius of 200 (in unit of x axis) gives the reasonable results, as shown in Figure 4.6b. The Raman data, in the following sections, is based on the background subtraction by this rolling-circle filter.

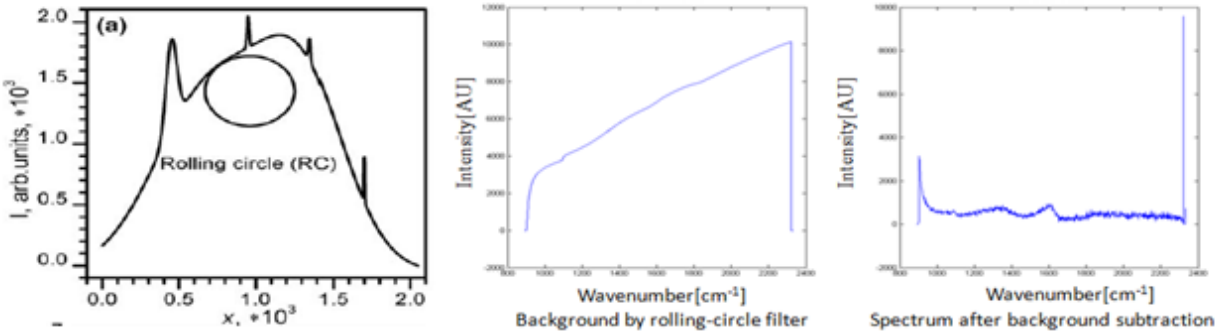


a) Rolling-circle filter[28].

b) Results after rolling-circle filter with a radius of 200.

Figure 4.6 Schematic and results of rolling-circle filter.

### *4.1.4 X-Ray Photoelectron Spectroscopy*

X-ray photoelectron spectroscopy (Jonathan Shu) was used to analyze the low *k* materials from an elemental perspective. As shown in Figure 4.7, an incident x-ray leads to the ejection of electrons from inner atomic orbitals. The characteristic binding energy of the electron is given by

$$E_{Bonding} = h\nu - E_k - W$$

(4.3)

where h$\nu$ is the photon energy of X-ray, $E_k$ is the resulting kinetic energy of the electron and W is the spectrometer work function, determined by the difference between the energy of the Fermi level and that of the vacuum level[29]. The bonding energy of electronic states in different elements differ, and thus the number of ejected electrons at the characteristic bonding energy provides information of number of atoms present in the surface region. The environment of the atom also has an effect on its bonding energy, and thus shifts in the bonding energy provides information on structural and chemical changes. XPS is a surface-sensitive technique with a penetration depth of less than 10nm, so it was used as a supplemental tool to confirm results from FTIR and Raman.

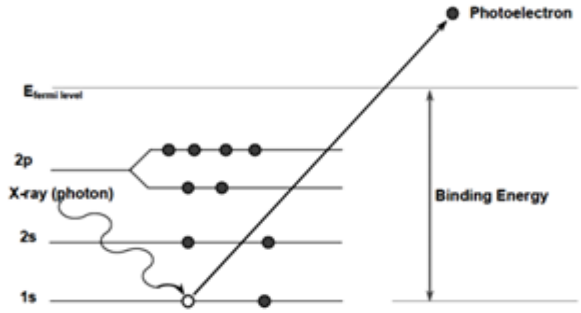


Figure 4.7 Mechanisms of XPS. Reprinted with permission from[29].

### *4.2 Optical Images by Microscopy*

Optical images (Figure 4.8) of porous samples (A) and dense samples (B), both as deposited and after furnace pre-anneal, as well as after LSA, were obtained using a Nikon microscope in CNF.

Samples as deposited (Figure 4.8a) showed a radial and cross-linked network on the surface. This was attributed to particles created before spin-coating, leading to small changes in the surface topography and film thickness.

After furnace pre-anneal (Figure 4.8b), the network changes into a jointing shape with agglomeration of particles into larger particles. This suggests that diffusion of small particles occurs during heating, and the larger resultant particles could be vulnerable to damage under LSA at high temperatures.

After LSA (Figure 4.8c), small black precipitates are observed at high LSA temperatures. No distinct trend was observed for the area and distribution of these precipitates under different dwell times and different samples. These precipitates may be simultaneously affected by two aspects: the film quality and the laser temperature (and the dwell time). Only when the temperature is high enough and defect sites are weak enough, precipitates can occur. This would explain why no significant trend in the distribution of these precipitates was observed.

When observed, the Fourth, by the scale of photolithography pattern (Figure 4.14), the width of the precipitates band was around 200-300 μm, which may have a negative effect on capacitance measurement, acting as pathways for current leakage.

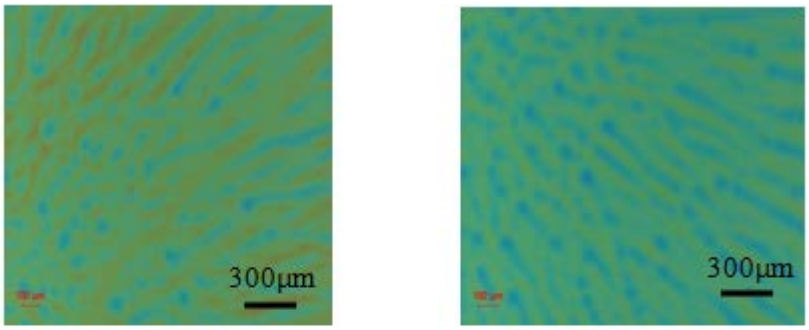


Porous Sample (A) Dense Sample (B)

a) Optical images of samples as deposited.

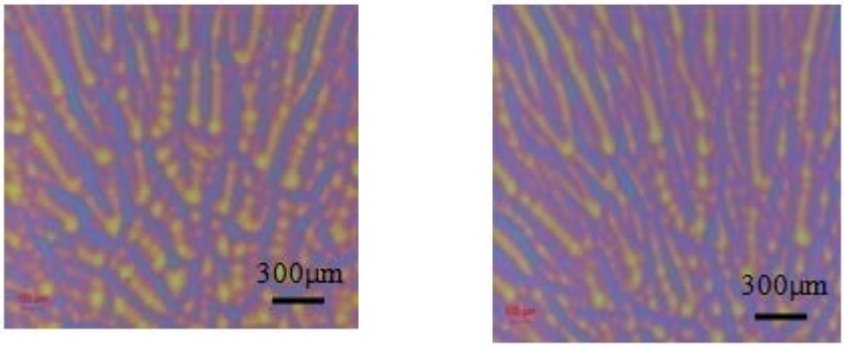


Porous Sample (A) Dense Sample (B)

b) Optical images of samples after furnace pre-anneal.

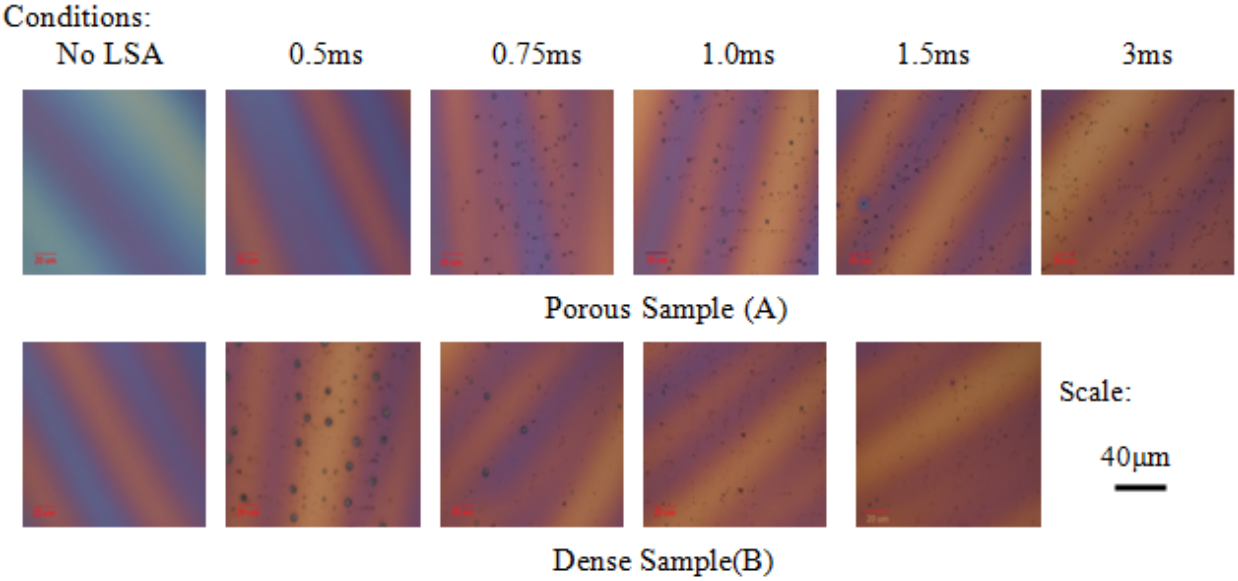


c) Optical images of samples after LSA (laser temperature around 1400℃).

Figure 4.8 Optical images of samples as deposited, after furnace pre-anneal and after LSA.

### *4.3 Thin Film Thickness*

Thickness measurements were made using a Woollam Spectroscopic Ellipsometer and a P10 Profilometer in CNF. The ellipsometer was used for samples as deposited and after furnace pre-anneals. Although extremely accurate, the spatial resolution is limited to 1mm, and so is not capable of measuring samples after LSA. The P10 profilometer was used for all the samples, both for confirmation of ellipsometry measurements and as the primary method for measuring samples after LSA.

#### *4.3.1 Thickness by Profilometry and its Variations*

The profilometer is a physical method to obtain the thickness and surface roughness. A diamond tip in contact with sample moves across the sample measuring the vertical displacement. To determine film thickness, samples were prepared by scratching down to the substrate to get two absolute flat surfaces. After leveling to these flat areas, the height between the substrate and the film surface was determined, as shown in Figure 4.9.

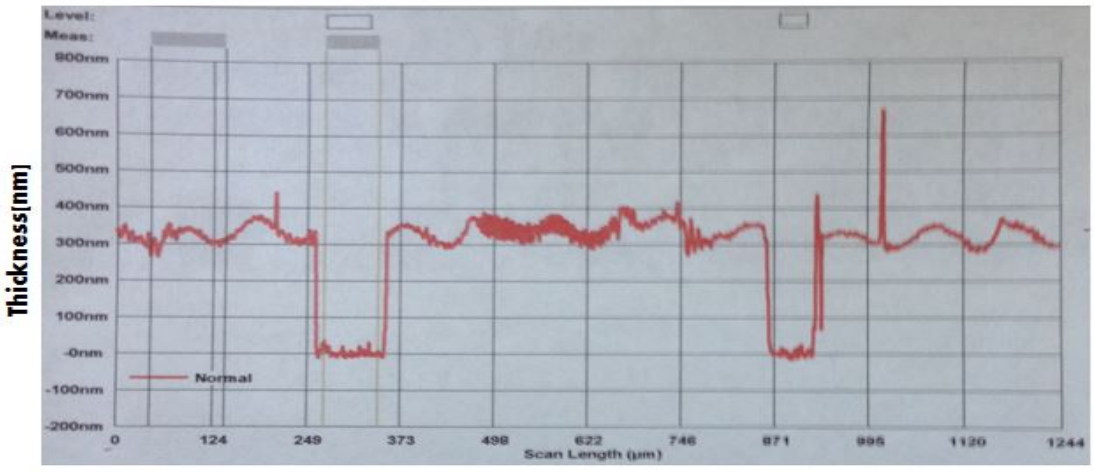


Figure 4.9 Thickness acquisition by profilometry (dense sample C, thickness of 316.3 ± 25 nm).

For samples after LSA, two steps of testing were performed. First, the thickness in the unannealed state was obtained as a reference thickness, using the above method. Second, the

thickness change (densification) by LSA was measured by mapping across the laser scan and leveling the profile to the unannealed regions on either side of the laser scan. The final thickness of LSA annealed films was obtained by subtracting this thickness change from the reference thickness. In this thesis, the lateral scan speed was 20 μm/second and the contact force was 2 mg. The thicknesses of porous sample (A) and dense sample (B) are summarized in Table 4.1.

Table 4.1 Thickness of porous sample (A) and dense sample (B).

| Sample | Thickness | | Average Thickness | Standard Deviation | Estimated Uncertainty |
|---|---|---|---|---|---|
| | Position 1 | Position2 | | | |
| A | 275.5 nm | 268.2 nm | 271.8 nm | 5.2 nm | 25 nm |
| B | 317.9 nm | 316.3 nm | 317.1 nm | 1.1 nm | |

An estimation for the thickness uncertainty was determined by three aspects. First, by comparing the bare silicon wafer and the unannealed low *k* film surface, a background variability of 60-100 nm was observed as shown in Figure 4.10. This background is likely due to the silicon wafer not being strictly flat. Such errors have a large effect on measurement when the scanning distance is long. Further, this background cannot be subtracted because the shape changes and the absolute error are large (60-100 nm). In this thesis, the background was not considered and the actual thickness may be slightly smaller than the calculated thickness.

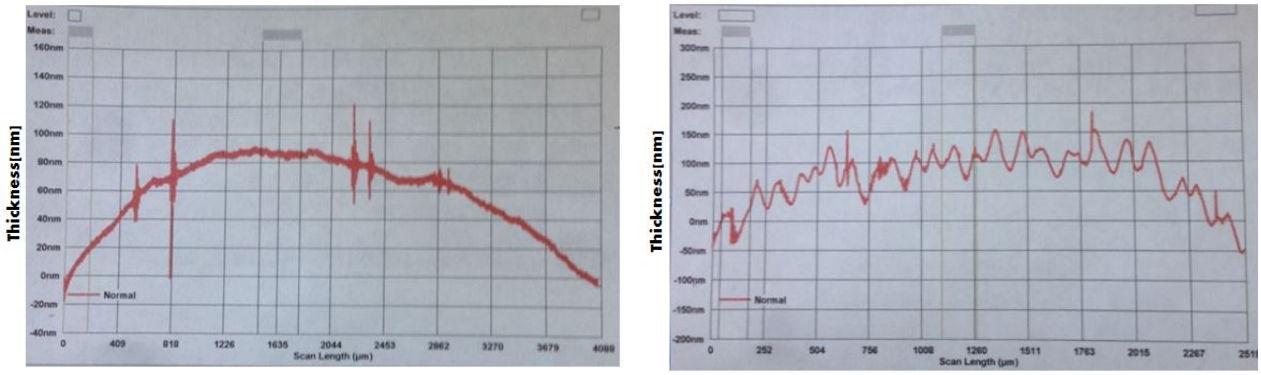


a) Thickness of the bare silicon wafer b) Thickness of the unannealed low k film

Figure 4.10 Comparison of thickness measurement by Profilometry in a long scan length.

Second, the morphology of the film (Figure 4.8) generates variation in thickness (Figure 4.10b). The variation was in the range of 20-30 nm and relatively uniform over the film surface. So, 25 nm is chosen as an estimation of the thickness uncertainty.

Finally, the local noise (roughness) leads to small deviations during measurement. It is not considered because its effect is small compared to the large scale variations.

### *4.3.2 Identification of Densification*

The identification of densification after LSA is affected by the morphology variations, as shown in Figure 4.11 for the porous sample A. The dense sample B shows essentially no additional densification with any changes obscured by the sample variations. The densification of porous sample A was modeled as a quadratic function. For the densification of the 0.5 ms dwell LSA on porous sample A in Figure 4.11, the width of densification is 450 μm, and the maximum change in thickness is -52.3 nm. Thus, with three points (-225.5 μm, 0), (0, -52.3 nm) and (225.5 μm, 0), the quadratic function was obtained as

$$T = 1.03\times10^{-3} L^2 - 52.3 \quad (4.4)$$

where T (in unit of nm) is the relative thickness to the unannealed area and L (in unit of μm) is the relative distance to the center. Similarly, the densification of 3ms dwell LSA on porous sample A was modeled as

$$T = 2.90\times10^{-4} L^2 - 125.3. \quad (4.5)$$

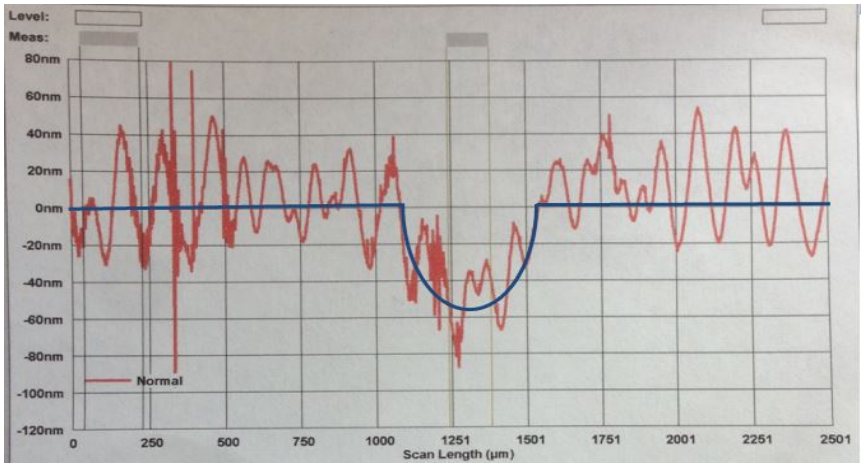


Figure 4.11 Densification of porous sample A under the 0.5ms LSA.

### *4.4 Capacitance and Dielectric Measurement*

A C-V capacitance measurement system was used to measure capacitance of sample. The system consists of an LCR meter with a resolution of 4 digits above 1pF, a mechanical movement stage, a vacuum and a camera.

#### *4.4.1 C-V Measurement*

As shown in Figure 4.12a, C-V measurements by an LCR meter is based on measuring the current through the device (LCUR) and voltage across the device (between HPOT and LPOT)[31]. By obtaining the amplitude and phase angle of the current and voltage, the capacitance is calculated.

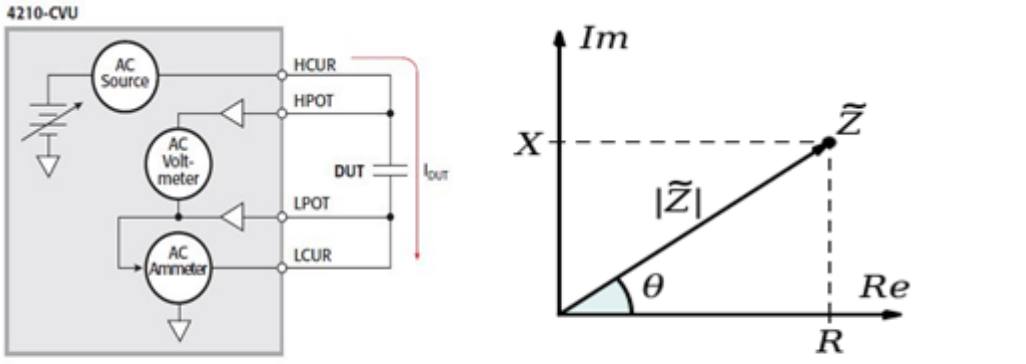


a) Schematic of LRC meter. b) Schematic of complex impedance plane.

Figure 4.12 Mechanisms of C-V measurement by LRC meter.

For these samples, the inductance was taken to zero. Between two common impedance models, the series model makes more sense than the parallel model, and thus the series capacitance (C) is assumed to be in series with a series resistance (R). As shown in Figure 4.13b, with the measured amplitude, $|\tilde{Z}|$, and the phase angle, $\theta$, the impedance is determined by

$$\tilde{Z} = |\tilde{Z}|e^{j\theta} \tag{4.6}$$

$$|\tilde{Z}|=R^2+X_c^2 \tag{4.7}$$

$$\tan\theta = \frac{X_c}{R} \tag{4.8}$$

$$X_C = -\frac{1}{\omega C}. \tag{4.9}$$

### *4.4.2 Metal-Insulator-Semiconductor (M-I-S) Structure*

Samples for the C-V measurement were based on a metal-insulator-semiconductor structure[32], that is, the silicon wafer as a semiconductor, the low *k* film as a dielectric and the metal contact (aluminum) on top. As shown in Figure 4.13a, the C-V measurement involves three important designs for the M-I-S structure, including DC bias, AC signal and metal contacts.

DC bias can accumulate electrons to the interface between the low *k* dielectrics and the silicon wafer, so that the capacitance is measured across the low *k* film. The measured results have confirmed this model, as shown in Figure 4.13b. As the DC bias voltage is reversed into the inversion region, electrons move away from the low *k* film and the capacitance reaches a minimum. As the DC bias voltage becomes positive in the depletion region, electrons are attracted towards the low *k* film interface and the capacitance increases. At a DC strongly in the accumulation region, electrons cannot go through the low *k* film and accumulation at the interface causing the capacitance to reach its maximum. In this thesis, the capacitance under a DC bias of 20-30V was averaged to represent the capacitance of low *k* materials.

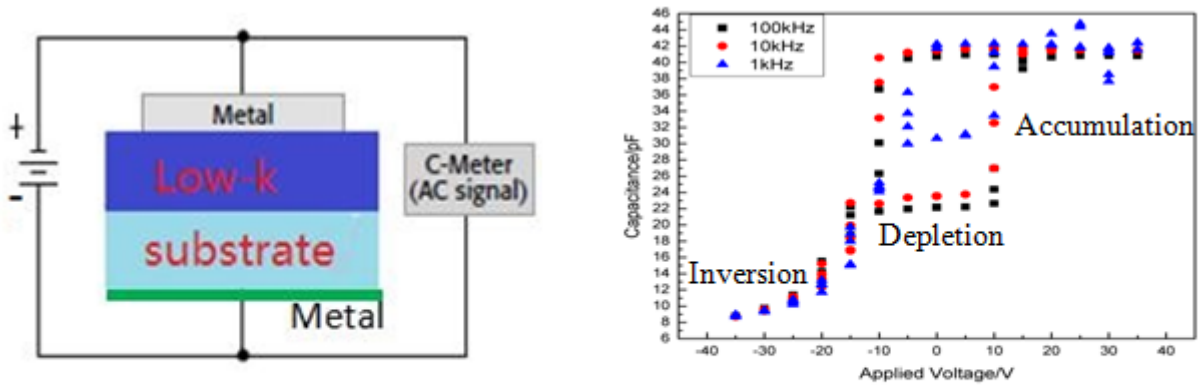


a) Schematic of Metal-Insulator-Semiconductor Structure.

b) Capacitance loop by DC bias sweep under various AC frequencies.

Figure 4.13 Mechanism of capacitance measurement for low *k* films.

According to Equation 4.9, an AC signal with a high frequency is required because of the extremely low capacitance of these films. A very high frequency can increase the capacitive reactance giving greater signal for detection. Figure 4.13b showed frequencies between 1 kHz to 100 kHz did not affect greatly on the capacitance under a high DC bias. In this thesis, 100 kHz was chosen as the AC signal.

Metal contacts were deposited on the top and bottom of the low *k* film. Metals contacts on the top (Cr 3 nm / Al 300 nm) enabled the tips to contact the low *k* film using micromanipulation. Metals contacts on the bottom (Cr 3 nm / Al 300 nm) ensured a good contact between the silicon wafer and the stage.

Oxidized silicon wafers were used to calibrate the C-V determined capacitance. C-V measurements are very sensitive because of the very low capacitance values. It was found that cleaning the samples and the stage before each measurement was critical to obtain good values. In the future, better metal contacts in the photolithography steps would also benefit the capacitance measurement.

### *4.4.3 Alignment*

In order to perform measurements at precise positions with respect to the laser scan lines (temperatures), three alignments were done: pre-alignment, laser alignment and post alignment.

For pre-alignment, two marks were made on the corner of the sample. These were used as two reference positions, as shown in Figure 3.6. With other areas protected by photoresist, the marks were etched using an Oxford Plasma 81 Etcher (in CNF) with $CF_4$ for 10 minutes.

As shown in Figure 3.6, the laser alignment used the marks, with the same patterns on the camera, to establish the locating of the laser scans on the samples. This enabled spatial temperature profiles to correlate with the spatially resolved parameter measurements.

For C-V measurements, long aluminum metal lines were deposited along the laser scan direction. As shown in Figure 4.14, 20 μm aluminum strips run parallel with the visible laser scan. The length of these aluminum strips was 12 mm with a spacing of 5 μm. At the top of each strip, a 100 μm×100 μm strip was used to contact the tip. A small window was also opened on the aluminum strip to provide places for other spatially resolved measurements.

Patterned metal contacts were fabricated by lift off method using image reversal. Compared to positive photolithography, this method avoided residual metal contamination which might have adversely influenced the capacitance measurements.

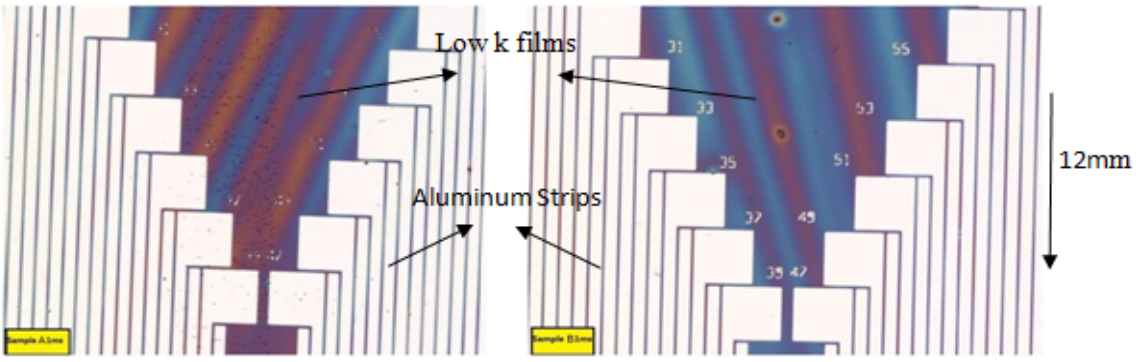


a) Post alignment for porous sample A. b) Post alignment for dense sample B.

Figure 4.14 Post alignment with aluminum strips of 20μm width, 12mm length and 5μm spacing.

### *4.5 Mechanical Measurement*

Mechanical properties can be characterized by measurements of modulus, hardness, stress and adhesion. In this thesis, a nano-indentation system (in Prof. Shefford P. Baker's lab) was used to measure modulus and hardness. After a hard tip was pressed onto the sample, the relation between load and displacement was obtained, as shown in Figure 4.15. The modulus, E, can be obtained as

$$E = \frac{1}{\beta} \cdot \frac{\sqrt{\pi}}{2} \cdot \frac{S}{\sqrt{A_p(h_p)}} \tag{4.10}$$

where $A_p$ is the projected area when the contact depth is $h_p$, S is the stiffness given by the slope of the curve dP/dh upon unloading, and β is the geometrical constant[33].

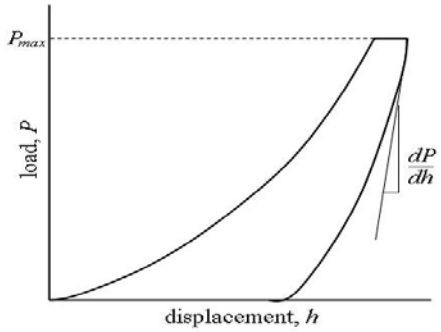


Figure 4.15 Schematic of relation between load displacement.
Reprinted with permission from [33].

CHAPTER 5

# CHEMICAL AND STRUCTRUAL EVOLUTION

## *5.1 Analysis of Synthesis Reaction*

The sol-gel reaction was described in Chapter 2. To confirm the success of these reactions and to explore the actual structure before LSA, chemical characterization of porous sample A by FTIR and XPS was performed.

### *5.1.1 Structural Evolution by FTIR Spectroscopy*

The structural comparison of as deposited and after furnace pre-anneal is given in Figure 5.1. The identification of the most important FTIR peaks is given in Table 5.1[34, 35].

First, spectra of a bare silicon wafer and of the pure porogen are shown as reference. The silicon wafer shows only a small Si-Si peak at 1100 $cm^{-1}$, while the porogen on a silicon wafer shows a strong $sp^3$ -$CH_2$ peak at 2846-2975 $cm^{-1}$, which is denoted as the porogen peak.

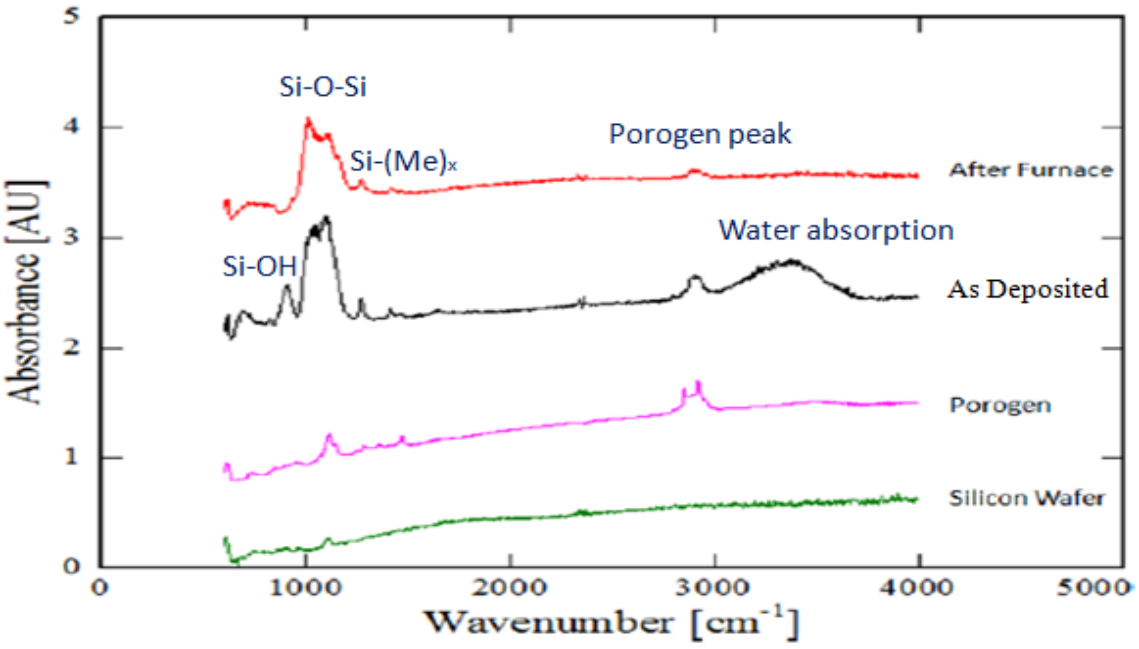


Figure 5.1 Structural comparison of as deposited and after furnace pre-anneal.

Table 5.1 Identification of FTIR peaks in literature. Reprinted with permission from [34, 35].

| Chemical bonds | Si-O-Si | $Si(Me)_x$ | Si-OH | Suboxide Si-O-Si | Network Si-O-Si | Ladder Si-O-Si |
|---|---|---|---|---|---|---|
| Literature[34] /$cm^{-1}$ | 730 | 754-848 | - | 1023-1035 | 1063-1065 | 1105 |
| Literature[35] /$cm^{-1}$ | ~800 | 760-850 | - | 1034 | 1060-1065 | - |
| Observed Peak/ $cm^{-1}$ | 730 | 816 | 902 | 1023-1035 | 1065 | 1105 |
| | | | | | | |
| Chemical bonds | Cage Si-O-Si | $Si(Me)_x$ | $Si(Me)_x$ | $sp^3$ $CH_2$ (porogen) | Absorbed $H_2O$ | |
| Literature[34]/ $cm^{-1}$ | 1135-1140 | 1273-1259 | 1405-1412 | 2873-2880 | - | |
| Literature[35]/ $cm^{-1}$ | - | 1270 | - | 2860-2930 | 3385 | |
| Observed Peak/ $cm^{-1}$ | 1140 | 1273 | 1412 | 2846-2975 | 3040-3727 | |

As deposited, sol-gel films exhibit a Si-O-Si peak in the range of 1000-1200 $cm^{-1}$. This confirms the success of the sol-gel process by creating the Si-O-Si backbones. This Si-O-Si peak contains four types of structures: suboxide (1023-1035 $cm^{-1}$), network (1063-1065 $cm^{-1}$), ladder (1105 $cm^{-1}$) and cage (1135-1140 $cm^{-1}$). The suboxide structure is the Si-O-Si bond with nonoxygen neighbors. In the cage structure[Figure 5.2c] the Si-O-Si bond angles open to 150° or larger; while in the network-like structure[Figure 5.2a] the bond angle reduces to <144°[36]. The cage structure is a 3D structure, created for coordinating with large side group. The cage structure, with more free space, tends to produce a lower *k* value, while the network structure tends to produce a higher modulus. The wavenumber characterization of these structures in FTIR is based on their different Si-O-Si bond energy. For the network, the bond angle is close to $SiO_2$, and thus is observed in a lower wavenumber. Both the cage and the ladder have ring structures. The vibration modes of a ring structure include the asymmetric mode, which has a higher intensity absorption and a higher wavenumber, and the symmetric mode, which has a lower intensity absorption and a lower wavenumber[37]. For the 3D cage structure, the symmetric mode is restricted and the asymmetric mode can be used to quantify the cage structure[37]. In

contrast, the symmetric mode can be used to quantify the ladder structure in a relatively low wavenumber range.

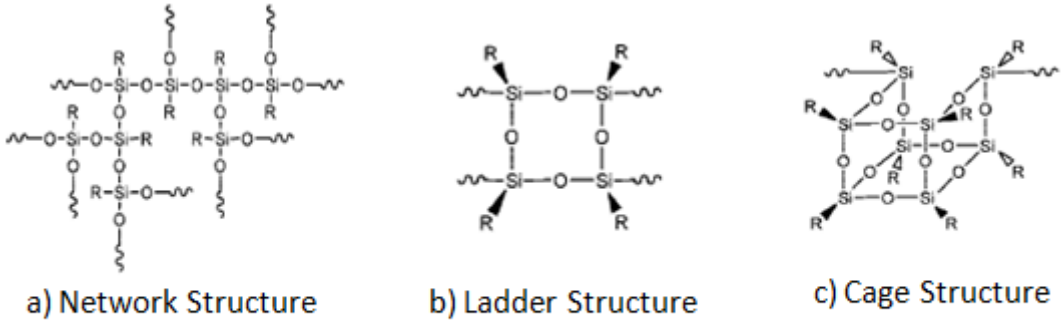


Figure 5.2 Structures of Si-O-Si bond in low *k* materials.

As deposited, the carbon-related peaks include the Si-$(Me)_x$ peaks and the porogen peak, which are used as indicators of carbon content. The Si-$(Me)_x$ peaks at 754-848 $cm^{-1}$ and 1273-1259 $cm^{-1}$ can indicate the intensity of various methyl substitutions on silicon atoms.

As deposited, the -OH related peaks including the Si-OH peak and the water peak, which must ultimately be removed. The Si-OH peak near 900 $cm^{-1}$ arises from the hydrolysis reaction. This indicates that the sol-gel reaction is not completed even after synthesis and baking. The water absorption peak at 3040-3727 $cm^{-1}$ negatively affects the k value.

After the furnace pre-anneal at 400 ℃, the water absorption peak disappears, indicating that the furnace does effectively evaporate water from the low *k* films. Second, the Si-OH peak is also removed, indicating that the furnace can accelerate the condensation reaction and introduce additional Si-O-Si bonds .

After the furnace pre-anneal, significant changes occur in the sub-peaks of the Si-O-Si bonds, as shown in Figure 5.3. A linear baseline was used to model the spectrum background. The peak areas of four structures from the Si-O-Si bonds and one peak from the Si-OH bond are summarized in Table 5.2. The Si-OH bond density decreases dramatically, as they develop into

Si-O-Si bonds by the condensation reaction. Similarly, the ladder structure decreases, indicating that the ladder structure reacts with Si-OH bonds. Since silicon atoms in the product are connected with large functional groups, the ladder structure favors the transformation into a 3D cage structure. Table 5.2 shows this dramatic increase of the cage structure. In contrast, the suboxide and network structures change only slightly. The peak center of the Si-OH and suboxide structures are within the reasonable range, as reported in the literature[34][35]. In conclusion, the furnace pre-anneal leads to the completion of the condensation reaction and the creation of cage structures by connecting ladder structures with Si-OH bonds.

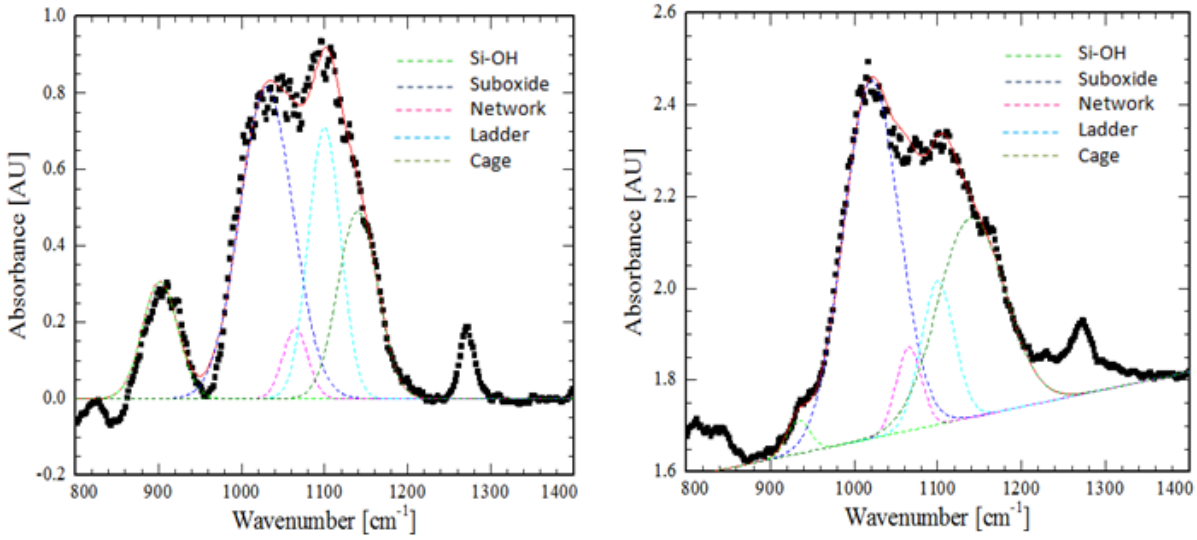


a) As deposited b) After the furnace pre-anneal

Figure 5.3 Fitting of four structures from Si-O-Si bonds and one peak from Si-OH bond.

Table 5.2 Summary for peak areas of Si-OH peak and of four structures from Si-O-Si peaks.

| | | **Si-OH** | **Suboxide** | **Network** | **Ladder** | **Cage** |
|---|---|---|---|---|---|---|
| As Deposited | Peak Center/ $cm^{-1}$ | **902** | **1030** | 1065 | 1105 | 1140 |
| | Peak Area | **16.3** | 65.4 | 6.9 | **34.5** | **29.3** |
| After Furnace Pre-anneal | Peak Center/ $cm^{-1}$ | **933** | **1023** | 1065 | 1105 | 1140 |
| | Peak Area | **2.5** | 64.5 | 6.9 | **15.9** | **43.7** |

After the furnace pre-anneal, organic groups are mostly lost. As shown in Figure 5.4, both the porogen peak (2846-2975 $cm^{-1}$) and the $Si(Me)_x$ peak (1273-1259 $cm^{-1}$) have decreased by a factor of 2. The organic loss is an indicator of the carbon depletion and the pore creation, which help to maintain a lower dielectric constant. Also, this shows that the porogen and organic groups are not completely removed during furnace pre-anneal. Thus LSA, which can readily anneal films at a higher temperature, can potentially further remove the porogen.

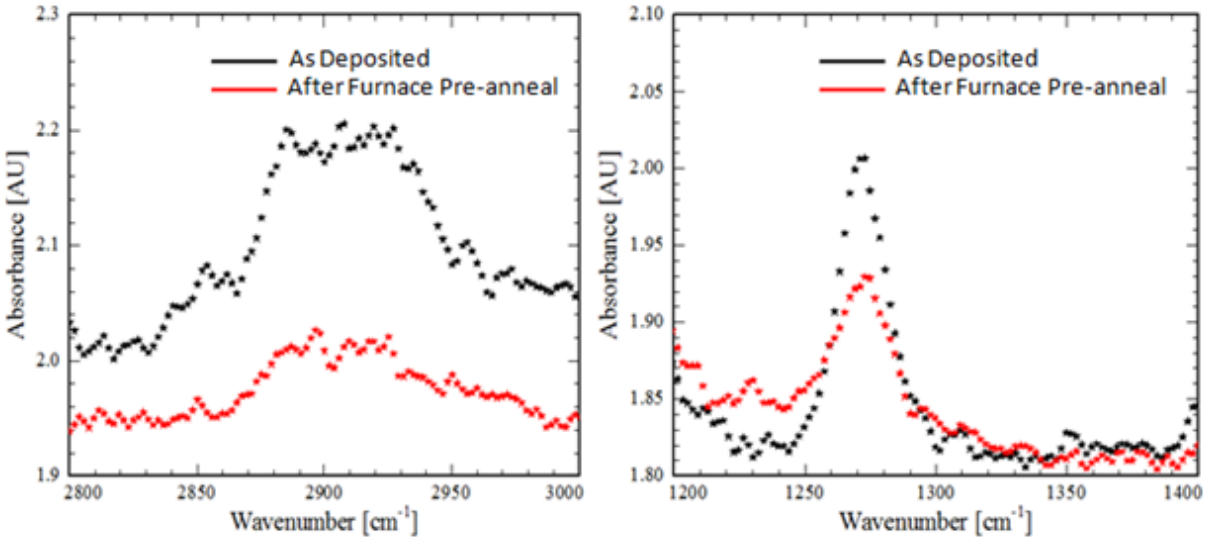


a) Comparison of porogen peaks. b) Comparison of $Si(Me)_x$ peaks.

Figure 5.4 Structural comparison of carbon-related peaks between as deposited and after the furnace pre-anneal.

The Si-C-C-Si bridge peak cannot be identified in the FTIR spectrum with any confidence, and hence it is difficult to prove the existence of this bridge after or during heat treatment. Literature suggests that Si-C bonds are relatively stable[38]. The standard enthalpy of formation for $Si\text{-}C(O)_3$ is -62.0 kJ/mol, which is comparable to the standard enthalpy of formation for $Si\text{-}(O)_4$, which is a strong bond with a value near -61.6 kJ/mol. Since C-C bonds in the other environment have a lower standard enthalpy of formation ($C\text{-}(C)_2(H)_2$ bonds are -20.7 kJ/mol and $C\text{-}O(C)(H)_2$ bonds are -33.9 kJ/mol), the Si-C-C-Si bonds should be relatively stable during the synthesis. Yet, it is also reported that the Si-C-Si bond can be broken down by oxygen

plasma, leading to an increased number of Si-O bonds and $Si(Me)_x$ bonds[39]. However, in our experiments, the scission of the Si-C-C-Si bridge is hard for the following three reasons. First, the furnace anneal was performed in nitrogen with no oxygen. Even for LSA, due to the extremely short annealing time and the protection of flowing nitrogen, it is hard for the oxygen in the air to attack the bridge. Second, any oxygen present is at a much lower energy than the oxygen plasma, so the scission is limited. Third, besides the scission of Si-C-C-Si, many other pathway for oxygen attack might occur, such as $-CH_3$ group formation and Si-O bond formation, hydrogen abstraction and oxygen incorporation, and hydrogen abstraction through -OH radical formation[39]. Most reaction pathways are more vulnerable than the scission of Si-C-C-Si bond. In conclusion, we infer that the Si-C-C-Si bridge remained throughout furnace pre-anneal and LSA. Further analysis by high resolution solid NMR experiments could potentially investigate the neighborhood environment of silicon and carbon[40]

### *5.1.2 Elemental Evolution by X-ray Photoelectron Spectroscopy(XPS)*

XPS results for as deposited and after furnace pre-anneal are shown in Figure 5.5. The relative concentration of C1s, O1s and Si2p peaks are summarized in Table 5.3. The Si2s peak at 150eV is not marked because its atomic scattering factor is very small.

Table 5.3 Summary for elemental evolution of the C1s, O1s and Si2p peaks in XPS.

| | | **C 1s** | **O 1s** | **Si 2p** |
|---|---|---|---|---|
| As Deposited | Peak Center | 280eV | 528eV | 98eV |
| | Chemical Bond | **C-C**(280.5eV) | **Si-OH**(527.6eV) | $SiO_2$(96.8eV)<br>$SiO_3$(99.8eV) |
| | Peak Area | 11878 | 32383 | 4840 |
| After Furnace Pre-anneal | Peak Center | 283eV | 531eV | 101eV |
| | Chemical Bond | C-O(282.7eV) | Si-O-X(531eV) | **$SiO_4$**(101.8eV) |
| | Peak Area | 10970 | 42830 | 5718 |

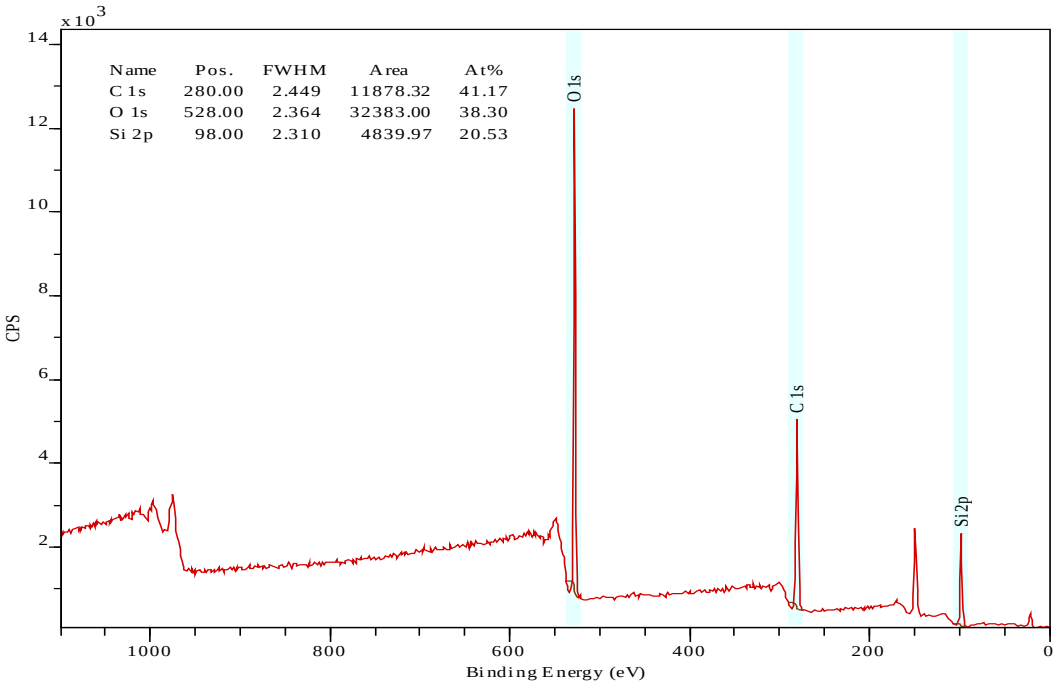


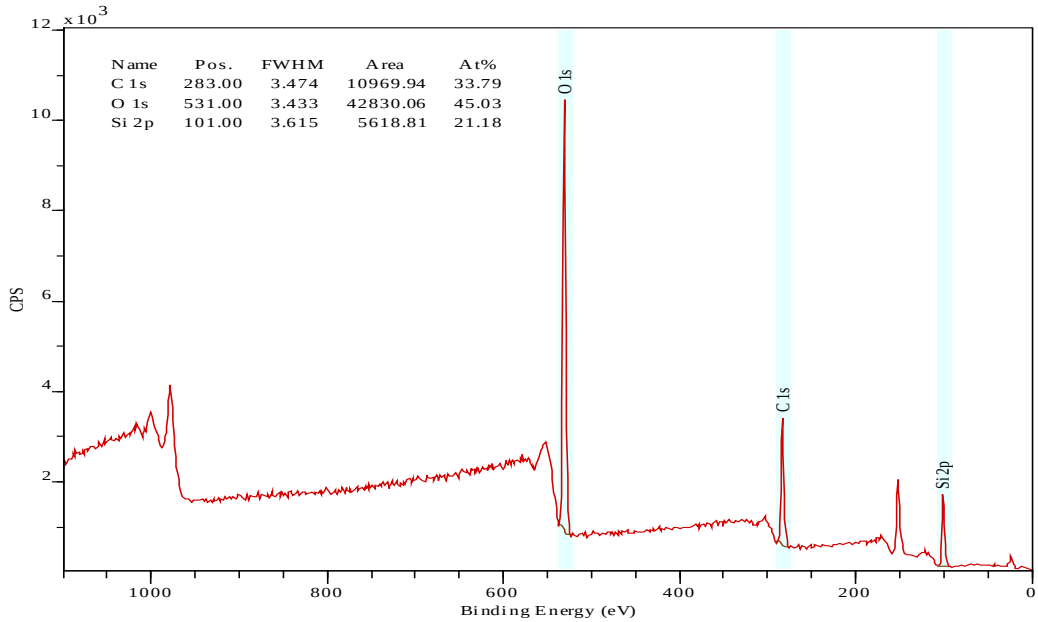


a) As deposited.

b) After furnace pre-anneal.

Figure 5.5 Elemental evolution from as deposited to after furnace pre-anneal.

Chemical shift and composition change are discussed here. For chemical shift, the bonding energy of the C1s peak shifts from 280 ev to 283 eV indicating a bond change from a C-C bond (280.5 eV) to a C-O bond (282.7 eV)[41]. This proves these organic groups are oxidized during the furnace pre-anneal. This information matches the decrease of the Si-$(Me)_x$ peak and the porogen peak in FTIR. Second, the bonding energy of the O1s peak shifts from 528 ev to 531 eV indicating a bond change from a Si-OH bond (527.6 eV) to a Si-O-(Si or X) bond (531 eV) [41]. In other words, the Si-OH bond, which has a higher polarizability, is removed, and this information matches the decrease of the Si-OH peak in FTIR. It proves that the secondary condensation of hydroxyl and alkoxy groups occurs with Si-O-Si bonds being created. Third, the bonding energy of the Si2p peak shifts from 98 ev to 101 eV. When the silicon is more oxidized, the bonding energy shifts to higher energy, from Si-$O_2$ (96.8 eV) to Si-$O_3$ (99.8 eV) to $SiO_4$ (101.8 eV), so it again proves the oxidization of silicon atoms[41]. For composition change, carbon is lost with a corresponding increase in oxygen, indicating oxidization of silicon concurred with carbon loss.

### *5.2 Chemical Effects of Laser Spike Annealing*

#### *5.2.1 Temperature-Dependent Structural Evolution*

Based on the spatial temperature profile, the structural information at varying laser temperatures was obtained as a function of the relative position compared to the laser scan center. The porous sample A under 3ms LSA (total maximum temperature: 1462 ℃) is described in this section.

***Baseline Variations within Samples***

In order to achieve effective comparison between points, the uniformity of FTIR was measured. As shown in Figure 3.4 and Table 3.2, six scans with different dwell times were performed on the same sample. Baseline spectra on either side of each LSA scan were obtained. Although

expected to be similar, significant changes were observed across the sample as shown in Figure 5.6. The laser annealing temperature is approximately zero at these positions and the total annealing temperature is hence only 400 ℃. The data show that the cage structure fraction decreases along the sample with only slight changes in the other three structures. This result matches the data from hotplate annealing, as discussed later with Figure 5.16. This suggests that an continuous temperature variation might occur along the hotplate, leading to the cage structure loss.

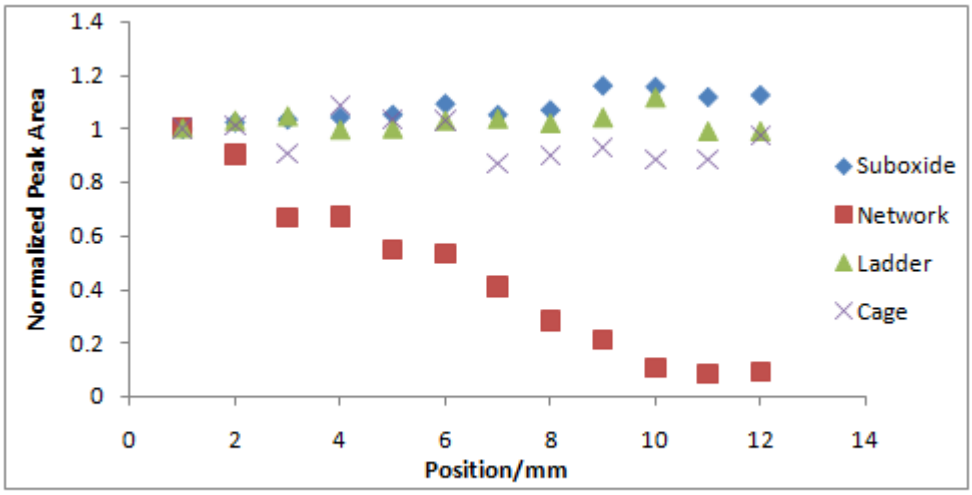


Figure 5.6 Variation in the baseline spectra due to hotplate temperature difference.

Difference in the local environment of the sol solution can also greatly affect the baseline structure. As shown in Figure 5.7, before the gel point during spin coating, the sol solution has already created chains and connections, which vary in different local environments. Individual samples should be relatively consistent but significant differences may exist between samples. Such behavior was observed as discussed later with Figure 5.17.

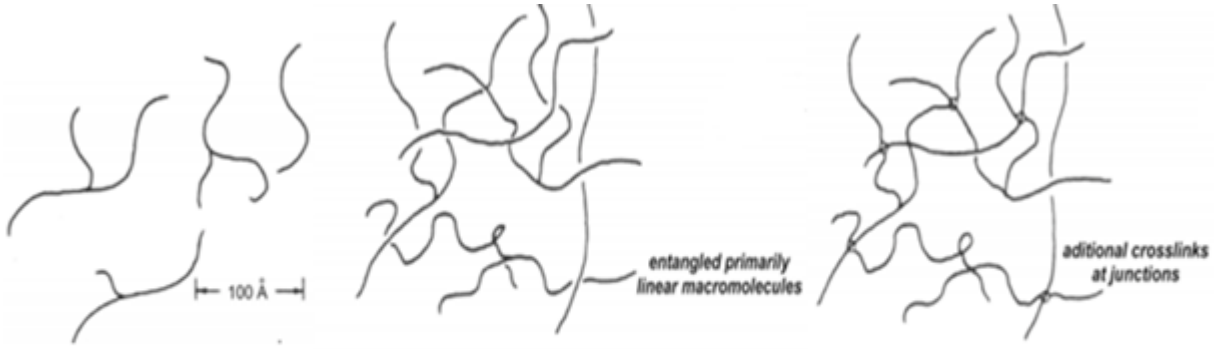


a) Sol far from gel point. b) Sol near gel point. c) Gel Point.

Figure 5.7 Baseline-structural evolution from sol solution to gel point.
Reprinted with permission from [42].

For a single scan, it is assumed that the initial structure is constant. This assumption was justified by examining the strip with no LSA at different points (four points from left to right with a spacing of 100 μm), as shown in Figure 5.8. The spectra are essentially the same when normalized, as shown in Figure 5.8b. Thus it is valid to compare data from the FTIR mapping across a single LSA scan.

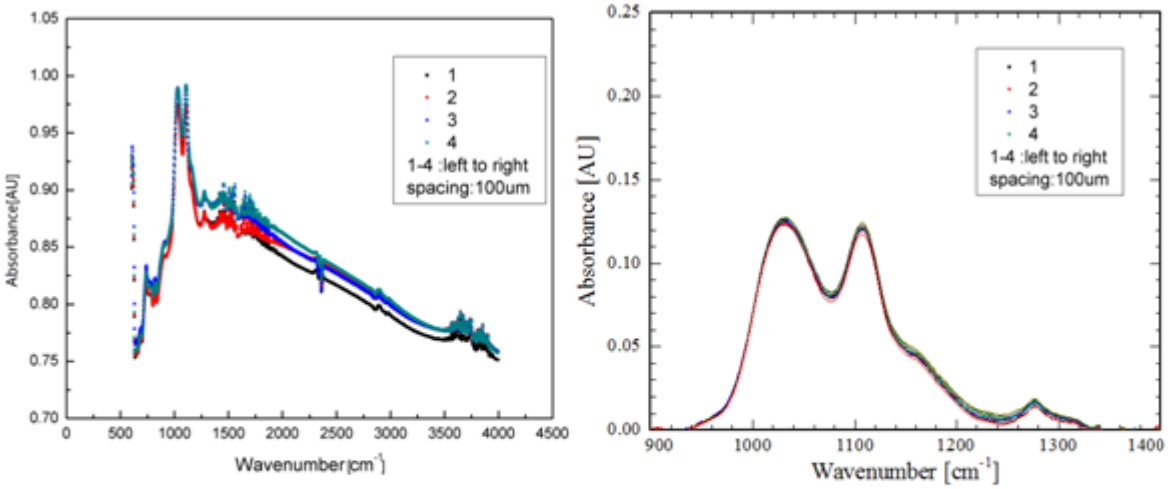


a) Comparison of different points across the strip with no LSA.

b) Spectra after normalization and removal of a linear background.

Figure 5.8 Comparison of spectra across four points corresponding to the area of an LSA strip but with no LSA anneal.

***Changing Spectrum across Sample under LSA***

The structural evolution of FTIR mapping on the 3 ms dwell time sample is shown in Figure 5.9a. On the edge of the laser scan ($T_{peak}$ = 428 ℃), the Si-O-Si bond shows two peaks. At the laser scan center ($T_{peak}$ = 1462 ℃), the Si-O-Si bond changes into a single peak. The continuous evolution of the Si-O-Si peaks across the 3ms laser scan, at a spacing of 25 μm, is shown in Figure 5.9b. This shows the transformation from two peaks to a single peak as the temperature increases. The decrease on the left edge indicates loss of the suboxide structure. The increase in the middle indicates an increase of the network structure. Finally, the two unchanged edges on the right indicates that the ladder structure and the cage structure are only slightly modified. Thus under a high laser temperature, the suboxide structure develops to the network structure with the cage structure being retained.

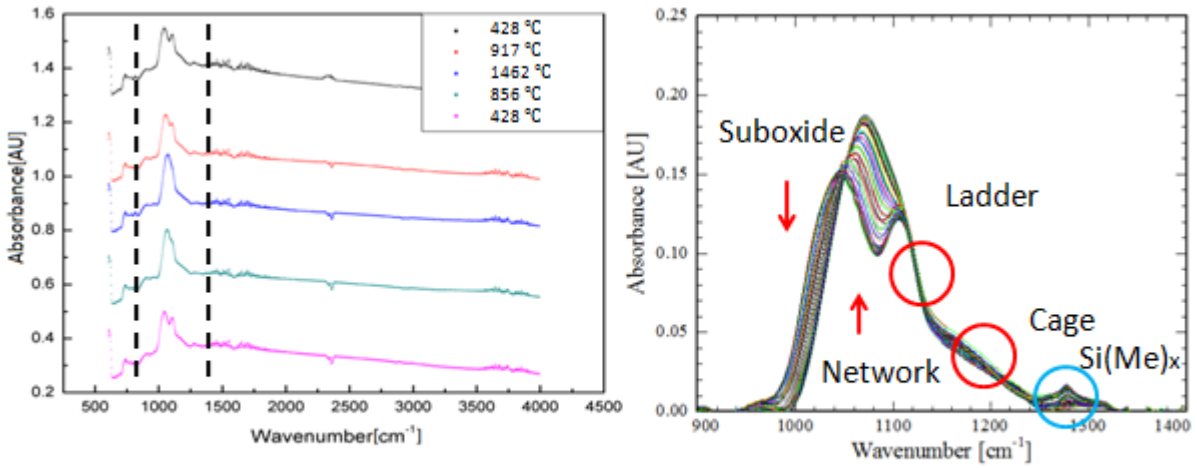


a) Structural comparison in representative points. b) Continuous structural evolution.

Figure 5.9 Structural evolution in the FTIR mapping.

Quantitatively, the four sub-peaks in the Si-O-Si bond were fitted into Gaussian peaks as shown in Figure 5.10. For fitting, the peak centers were fixed, with the suboxide structure at 1035 $cm^{-1}$, the network structure at 1065 $cm^{-1}$, the ladder structure at 1105 $cm^{-1}$, and the cage structure at 1140 $cm^{-1}$.

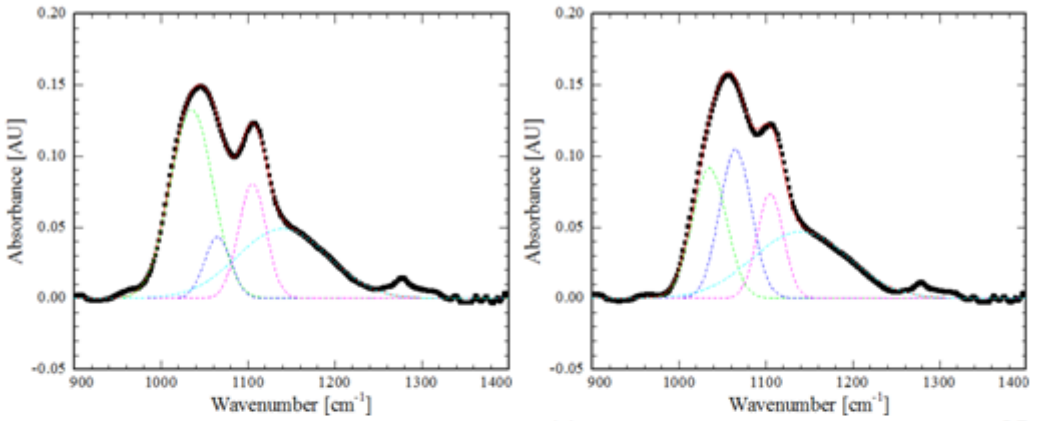


a) Position: 725µm, Temperature:416°C. b) Position: 375µm, Temperature:745°C.

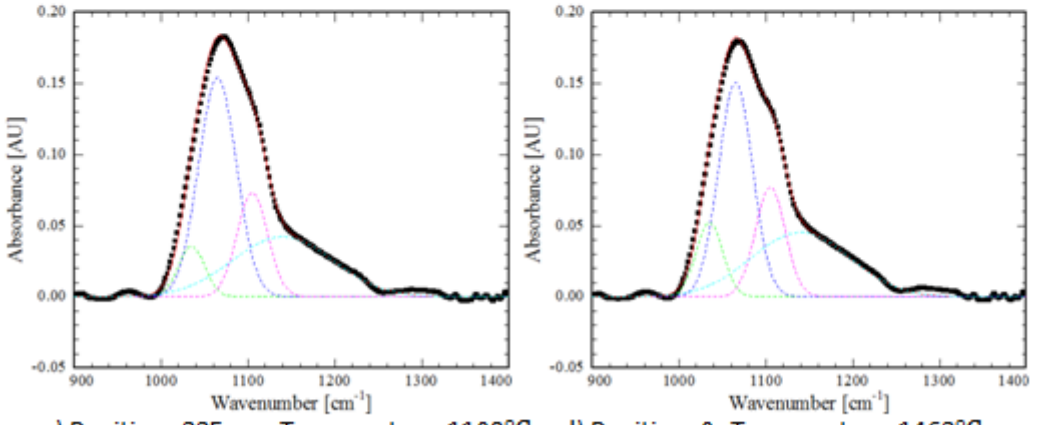


c) Position: 225µm, Temperature:1108°C. d) Position: 0, Temperature:1462°C.

Figure 5.10 Evolution of four sub-peaks in the Si-O-Si bond.

The peak area was then determined for each sub-peak. Figure 5.11 shows these peak areas as a function of the peak annealing temperature. The structural transformation from suboxide to network begins at near 500 ℃. Eventually, the network increases by a factor of 5.4. The network peak intensity continues to increase even at the higher temperatures studied. This suggests that even higher laser temperature could be used to create even more network bonds. Figure 5.11 also shows that the ladder structure and the cage structure change by less than 10%. The retention of the open cage structure helps to maintain a low *k* value.

As shown in Figure 5.9b, the Si-$(Me)_x$ peak decreases as the laser temperature increases. This indicates LSA can effectively remove any remaining carbon groups and increase the porosity. The threshold temperature for carbon loss (Figure 5.10) was determined to be between 1110-

1135 ℃. This temperature is the minimum temperature for complete carbon removal. Above 1200 ℃, no additional pores are formed by the LSA treatment.

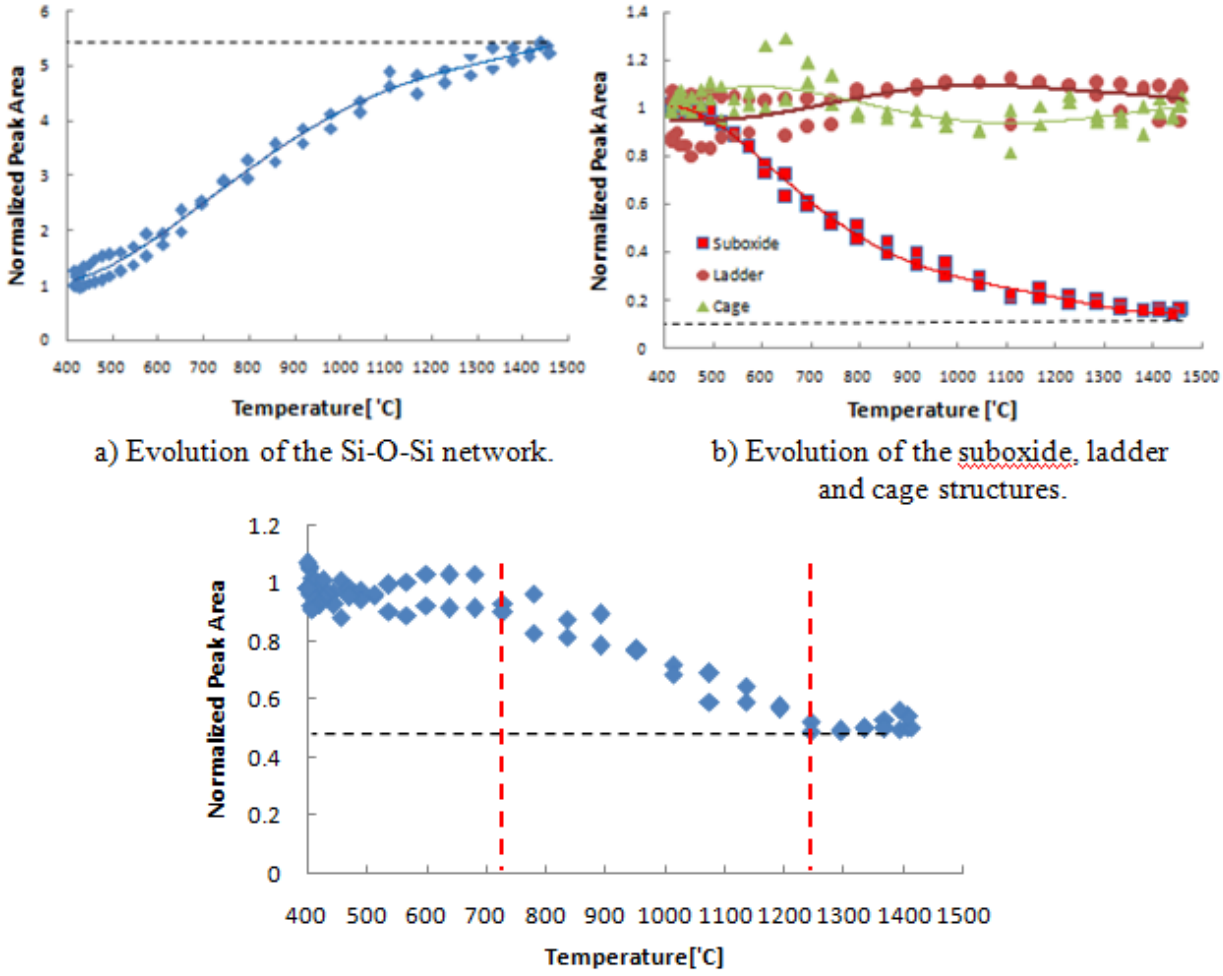


a) Evolution of the Si-O-Si network.

b) Evolution of the suboxide, ladder and cage structures.

c) Evolution of the porogen peak.

Figure 5.11 Temperature dependence of chemical evolution.

The porogen peak exhibits similar behavior, as shown in Figure 5.11c and 5.12. Above 700 ℃, the porogen begins to be removed by the LSA scan. The threshold temperature for the termination of porogen removal is approximately 1200 ℃. This behavior proves that high laser temperatures (700-1200 ℃) are an effective technique to burn off carbon groups, which in turn results in the creation of pores in the low *k* materials.

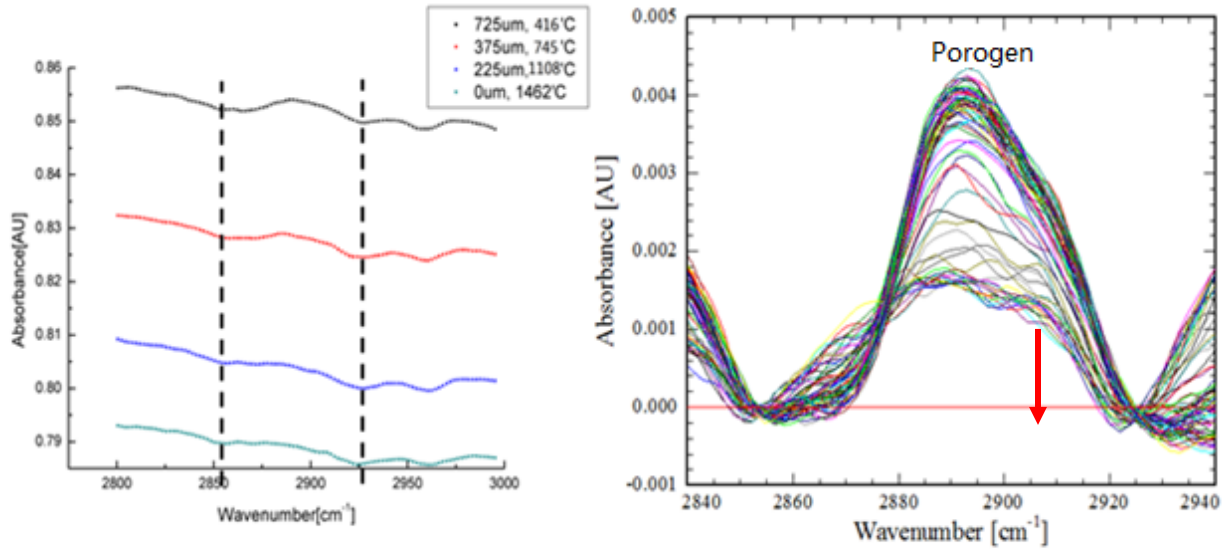


a) Structural comparison in representative points b) Continuous structural evolution

Figure 5.12 Comparison of porogen peak under different temperature.

### *5.2.2 Effects of Dwell Time*

The effect of 0.5 ms and 3 ms dwells on the structural evolution is shown in Figure 5.13. For the short dwell time of 0.5 ms, a higher threshold temperature at 800 ℃ is observed compared to the long dwell time threshold temperature at 500 ℃. In other words, a short dwell time requires a higher annealing temperature to initialize the structural transformation. Contrastively, a long dwell time can produce the structural transformation at low temperatures. This behavior illustrates the feasibility of high temperature, short time frame, annealing by LSA.

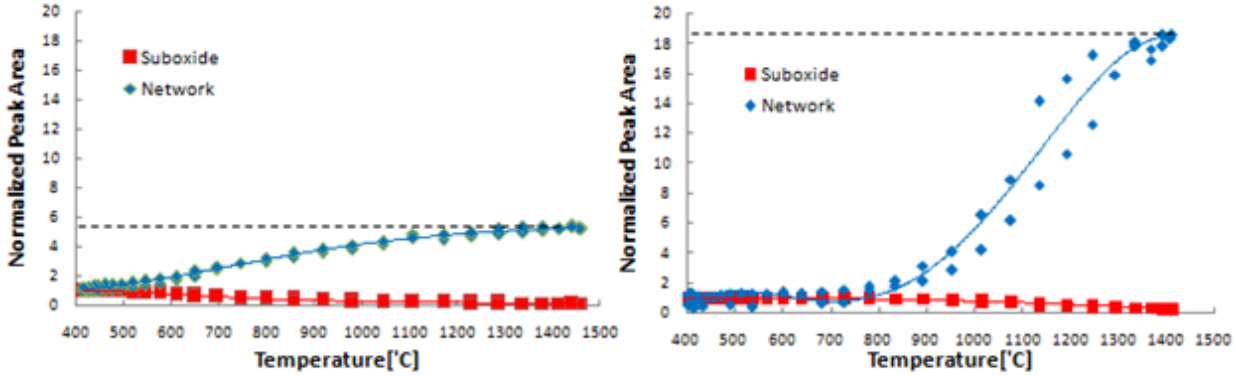


a) Long dwell time: 3 ms. b) Short dwell time: 0.5 ms.

Figure 5.13 Effects of dwell time on structural evolution behaviors.

From Figure 5.13, the short time effectively increases the network fraction by a factor of approximately 18, while the long dwell time increases the network fraction by only 6 times. This behavior is likely influenced by the initial baseline structure. As shown in Figure 5.14, the initial network in the 3 ms sample is higher than the initial network in the 0.5 ms sample, but their final structures are the same. The initial network peak area and the initial suboxide peak area are given in Table 5.4. Thus the difference of annealing effect is due to the influence from the initial baseline structures.

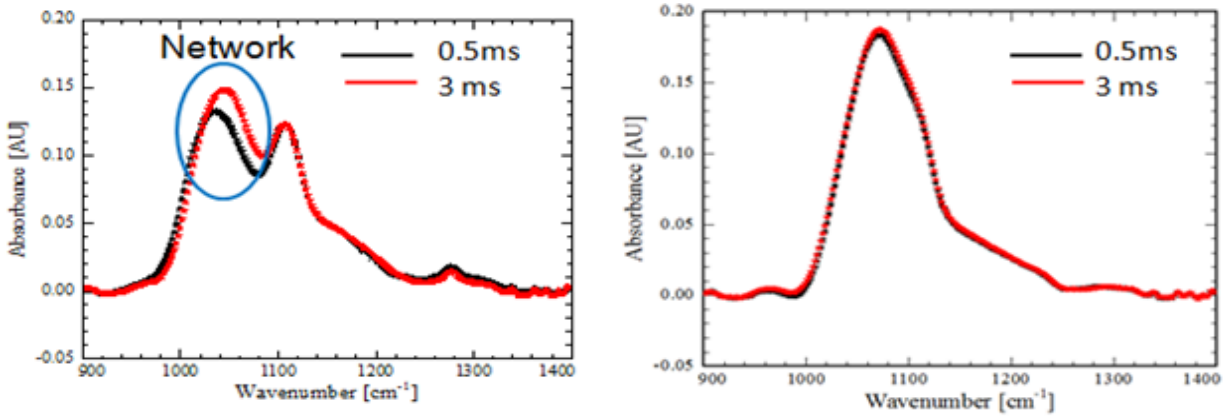


a) Under 400℃ (Initial Structure). b) Under 1400℃ (Final Structure).

Figure 5.14 Comparison of initial structure and final structure between 0.5 ms dwell time sample and 3 ms dwell time sample.

Table 5.4 Comparison of initial peak areas of network and suboxide between 0.5 ms dwell time sample and 3 ms dwell time sample.

| | Initial Network Peak Area | Initial Suboxide Peak Area |
|---|---|---|
| 0.5 ms Sample | 0.38 | 9.26 |
| 3 ms Sample | 1.64 | 8.22 |

### *5.2.3 Comparison of Hotplate Annealing and LSA*

The structure evolution by hotplate annealing at 400 ℃, 450 ℃, 500 ℃ and 540 ℃ for 2 hours is shown in Figure 5.15. With the increasing temperature, the Si-O-Si bond changes from two peaks into a single peak, similar to the behavior observed under LSA anneals.

By fitting the Si-O-Si bond, the evolution of the four structures as a function of the hotplate annealing temperature is obtained. Figure 5.16 compares the 3 ms LSA and the hotplate annealing, with hotplate annealing showing several distinctive behaviors compared to LSA.

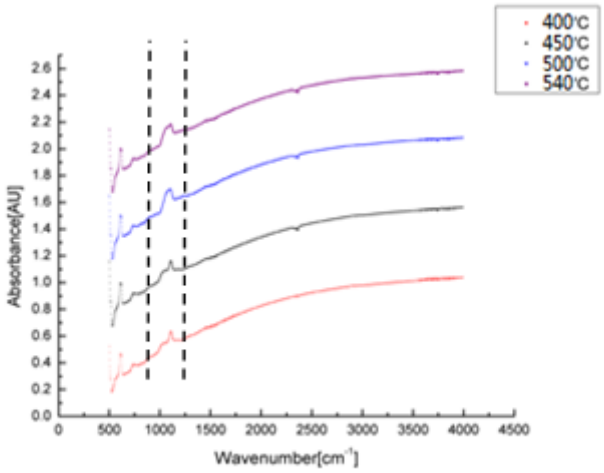


Figure 5.15 Structural evolution by hotplate annealing.

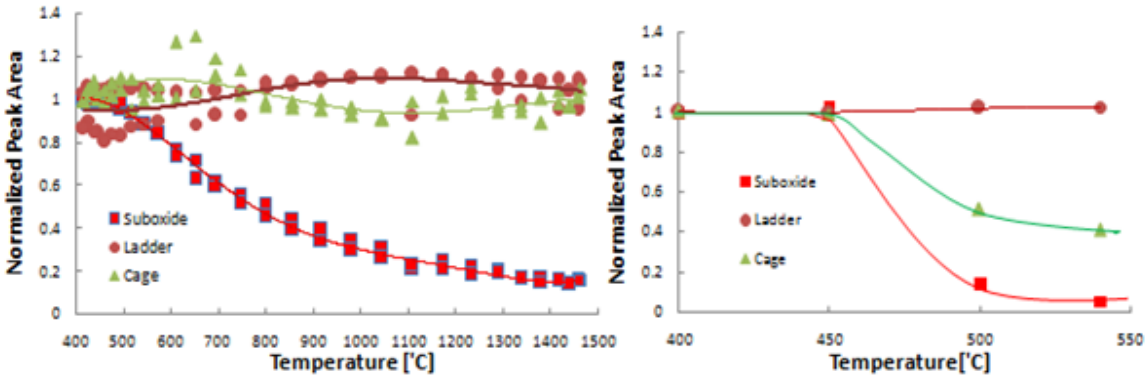


a) Suboxide, ladder and cage under 3 ms LSA. b) Suboxide, ladder and cage under hotplate annealing.

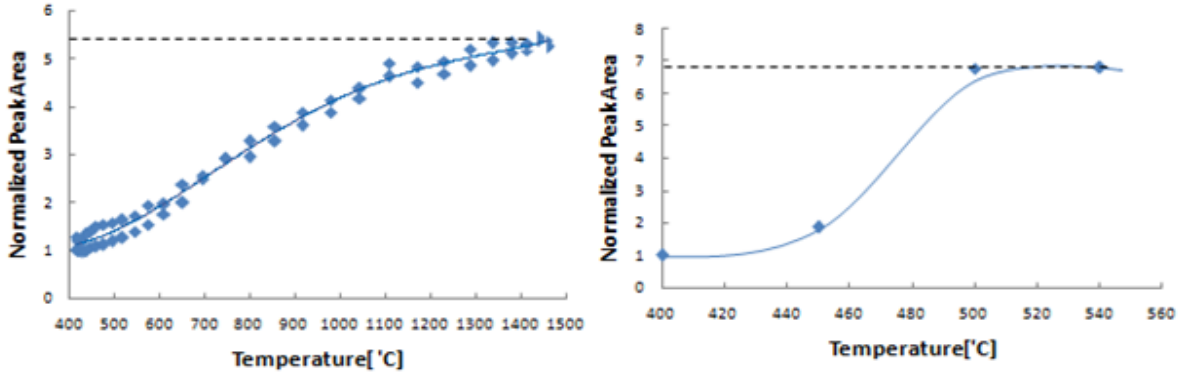


c) Network under 3 ms LSA. d) Network under hotplate annealing.

Figure 5.16 Comparison of structural evolution between LSA and hotplate annealing.

First, unlike LSA, the cage structure decreases indicating that transformation of both the suboxide and cage structures to the network structure are active. Since the cage structure should lead to a relatively low *k* value, the retention of the cage structure after LSA benefits its performance by increasing the mechanical properties (formation of network structure) while also maintaining a low dielectric constant. The reason of this different behavior is due to the different annealing mechanisms. For LSA, the oxidative reaction is minimized allowing for higher temperatures before oxidation occurs[40]. With insufficient oxygen, the cage structure can be retained. For hotplate annealing in air for 2 hours, the cage structure with multiple organic groups will be vulnerable to oxidative reaction, leading to the breakdown of the cage structure.

Second, the increase of the network structure is comparable between LSA (factor of 5.5) and hotplate annealing (factor of 6.8), although LSA has a higher initial network structure due to the influence of the local environment in the sol solution (Figure 5.17). LSA is thus more effective to create the Si-O-Si network structure than simple hotplate annealing. Based on this benefit, LSA with a high temperature and a short time frame exhibits the effectiveness for processing low *k* dielectrics.

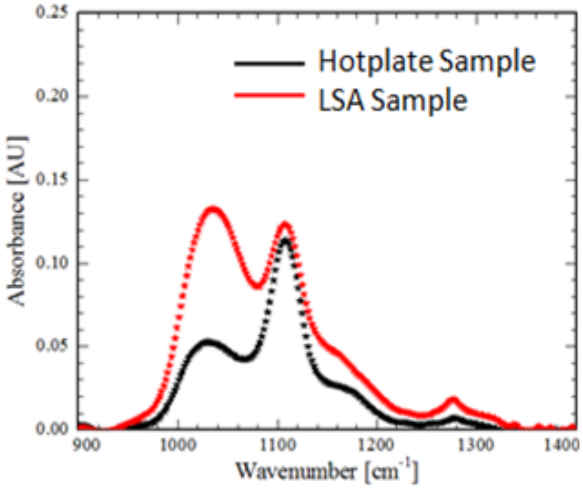


Figure 5.17 Comparison of initial structure between hotplate sample and LSA sample.

### *5.2.4 Comparison of Porous Sample and Dense Sample under LSA*

The effect of porosity under 0.5 ms LSA is given in this section. As shown in Figure 5.18, the porous sample shows a much larger increase in the network structure (factor of 18), when compared with the dense sample showing only an increase of 4×. This behavior is a result of the initial conditions and structures, as summarized in Table 5.5. The porous sample had a much lower amount of the network before LSA, so there existed more opportunity to create new network structures. The dense sample, while starting with a lower amount of structural transformation, finally obtains a higher amount of the network in the absolute number. Such a high amount of network in the dense sample is likely to result in a higher dielectric constant (see Figure 6.3). In conclusion, the porosity can directly affect the initial structure and indirectly affect the amount of the transformation from suboxide to network.

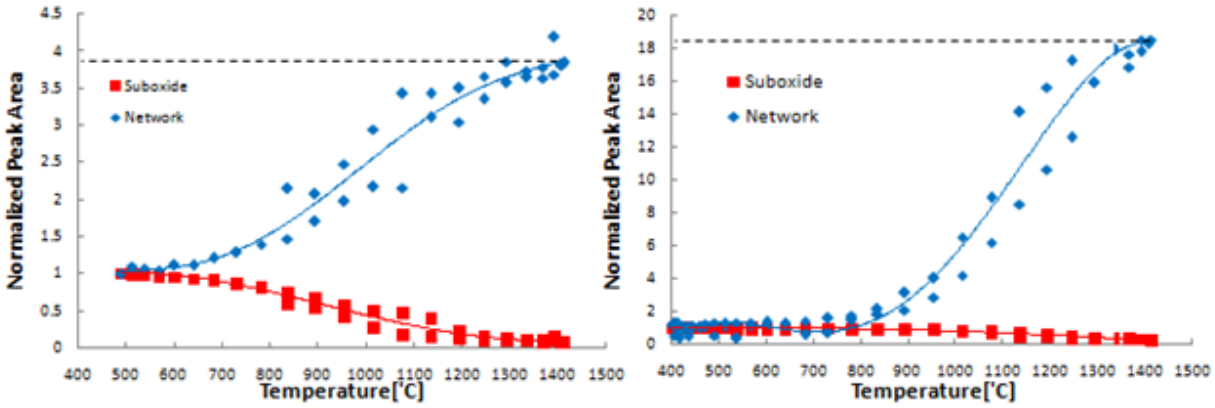


a) Dense sample. b) Porous sample.

Figure 5.18 Comparison of structure evolution between dense sample and porous sample.

Table 5.5 Summary of the initial and final structures of the dense and porous samples.

| Initial Network Area | | Initial Suboxide Area | | Final Network Area | | Final Suboxide Area | |
|---|---|---|---|---|---|---|---|
| Porous | Dense | Porous | Dense | Porous | Dense | Porous | Dense |
| **0.38** | **3.07** | 9.26 | 7.07 | 5.91 | 11.81 | **2.58** | **0.47** |

### *5.2.5 Concerns of Carbon Precipitation*

There are concerns that LSA may produce carbon precipitates in the high temperature region. Such precipitates were observed for the Global Foundries samples, although samples used in this thesis did not exhibit such behavior.

In Figure 5.19, Raman spectra on Global Foundries samples show that the -$CH_3$ stretching peak (2950 $cm^{-1}$) visible in unannealed samples disappears after LSA treatment. In its place, the D-peak and G-peak are created which correspond to clustering of $sp^2$ carbons.

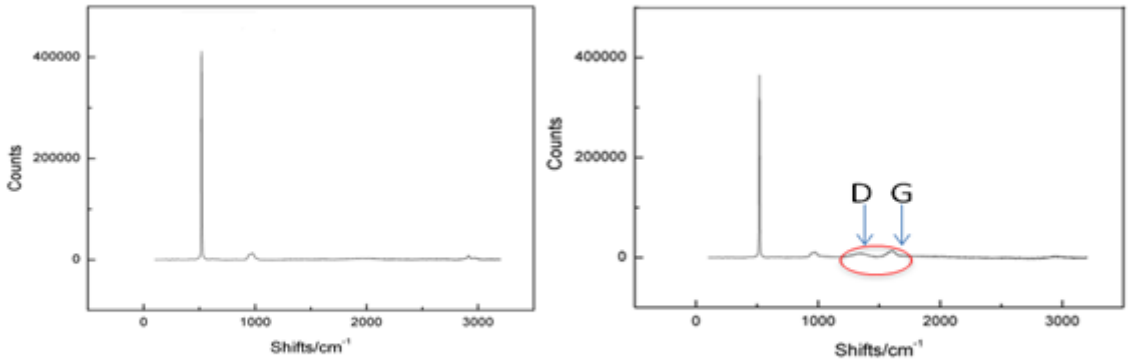


a) Unannealed sample. b) LSA annealed sample.

Figure 5.19 Carbon precipitation in Global Foundries samples characterized by Raman.

By Raman mapping, the temperature dependence of carbon precipitation was explored. Figure 5.20 shows a threshold behavior for formation of the carbon precipitates around 1000 ℃.

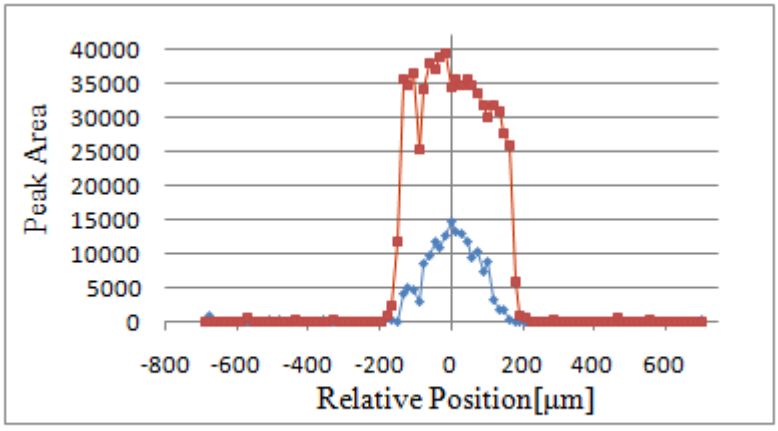


Figure 5.20 Temperature dependence of carbon precipitation under 0.5 ms dwells.

CHAPTER 6

# ELECTRICAL AND MECHANICAL EFFECTS OF LASER SPIKE ANNEALING

## *6.1 Temperature-Dependent Dielectric Constant Evolution*

After patterning metal contacts on the laser scan lines, the dielectric constant was measured across each laser scan. Figure 6.1 shows that the dielectric constant of the porous sample after 0.5 ms LSA ($T_{peak}$ = 1412 ℃). Data are shown both assuming the film thickness remained constant and using the thickness measured by profilometry. For temperature above 1000 ℃, the dielectric constant increases with increasing temperature. However, below 1000 ℃, the dielectric constant is approximately constant at 2.5. This value is a slightly higher than the 2.3 reported *k* value for similar materials in the literature[9], but still much lower than the 3.0 reported *k* value of the dense film in the literature[9]. Given that the porous sample in this thesis was heated to 400 ℃, the *k* value of 2.5 is successful. At high temperatures, densification occurs due to the modification of pore density and pore interconnection[43], which can greatly increase the modulus but also increases the *k* value.

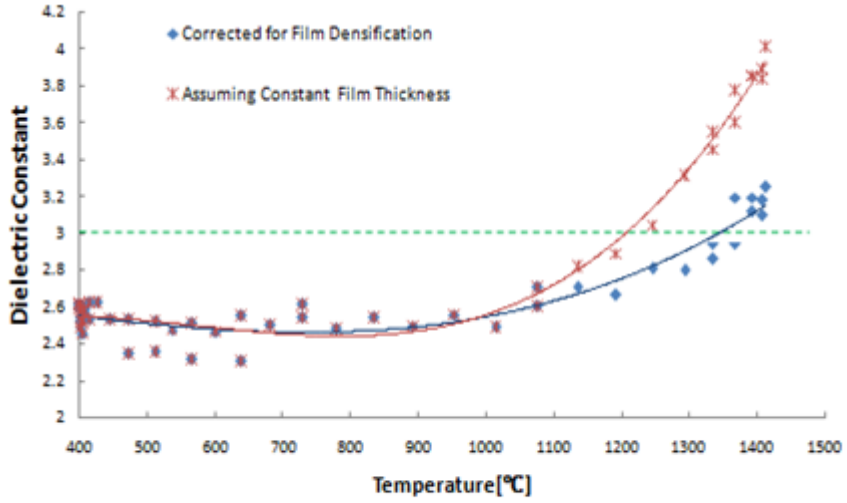


Figure 6.1 Temperature dependence of dielectric constant evolution. The constant dashed line represents the dielectric constant expected for a dense film from the literature[9].

As summarized in Table 6.1, the threshold temperature for densification is 1100 ℃. Above 1100 ℃, no further organic groups loss is observed and hence no new pores are formed. Collapse of the existing pores begins resulting in the observed densification. The dielectric constant begins to increase at the same time with the densification at 1000-1100 ℃. Below 1100 ℃, the dielectric constant remains stable, due to the tradeoff between the network formation and pore generation from remaining porogens.

Table 6.1 Summary of the threshold temperatures for several determinates of the *k* value.

| *k* Value Increase | Densification Start | Organic Group Loss Cease | Network Formation |
|---|---|---|---|
| 1000 ℃ | 1100 ℃ | 1100 ℃ | 800 ℃ |

### *6.1.2 Effects of Dwell Time and Porosity on Dielectric Constant*

Comparison of the dielectric constant between sample annealed with dwells of 0.5 ms and 3 ms is shown in Figure 6.2. For the long dwell time of 3 ms, the threshold temperature for the dielectric constant increase (950 ℃) is a slightly lower than the threshold temperature (1000 ℃)

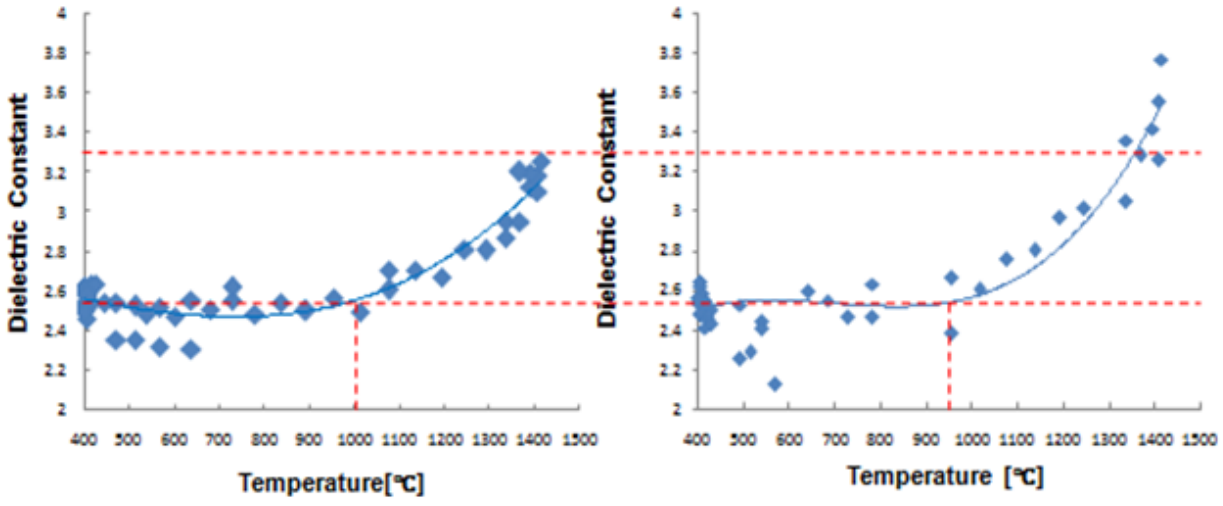


a) 0.5 ms. b) 3 ms.

Figure 6.2 Effects of dwell time on dielectric constant evolution behaviors.

for a dwell time of 0.5 ms, although the difference is not substantial. Below the threshold temperature, the *k* values of both sample are approximately the same at 2.5. Above the threshold temperature, the 3ms dwell leads to a higher *k* value at the same temperature due to a greater densification.

The dielectric constant comparison between the porous sample and a dense sample is shown in Figure 6.3. As discussed in Section 5.2.4, the dense sample initially has a high fraction of the Si-O-Si network, and thus the *k* value (around 3.8) is very high for even low annealing temperatures. The *k* value remains high (3.8-3.9) with increasing annealing temperature and no distinct densification is observed. This value is close to the *k* value of silicon dioxide (4.0). It is also found that when the porous sample is annealed under a long dwell time at high temperatures, the *k* value of the porous sample approaches that of the dense sample. In other words, the porous sample is evolving into the dense sample structure due to densification and the collapse of the pores.

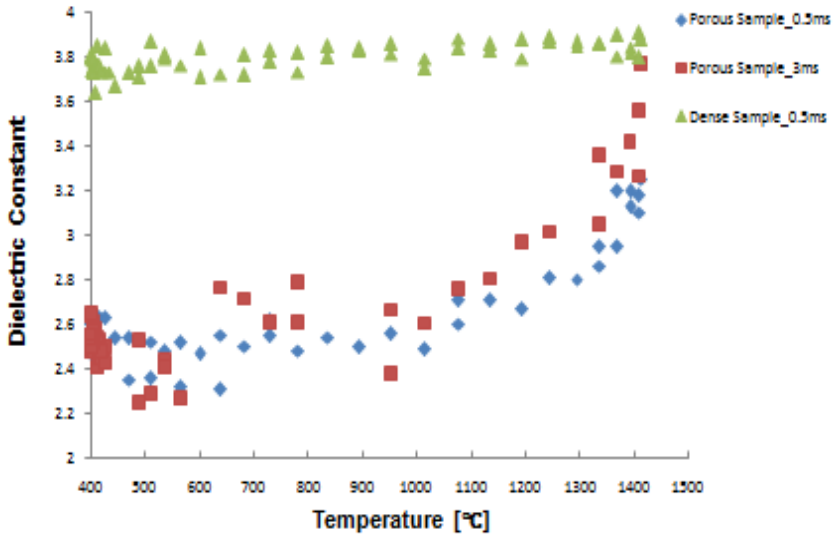


Figure 6.3 Effects of porosity on dielectric constant evolution behaviors.

### *6.1.3 Temperature-Dependent Modulus and Hardness Evolution*

The modulus and hardness of the porous sample after a 0.5 ms dwell LSA is related to the structural evolution and the dielectric constant evolution, as shown in Figure 6.4. Two important threshold temperature regions, 700-800 ℃ and 1000-1100 ℃, are marked in the figure.

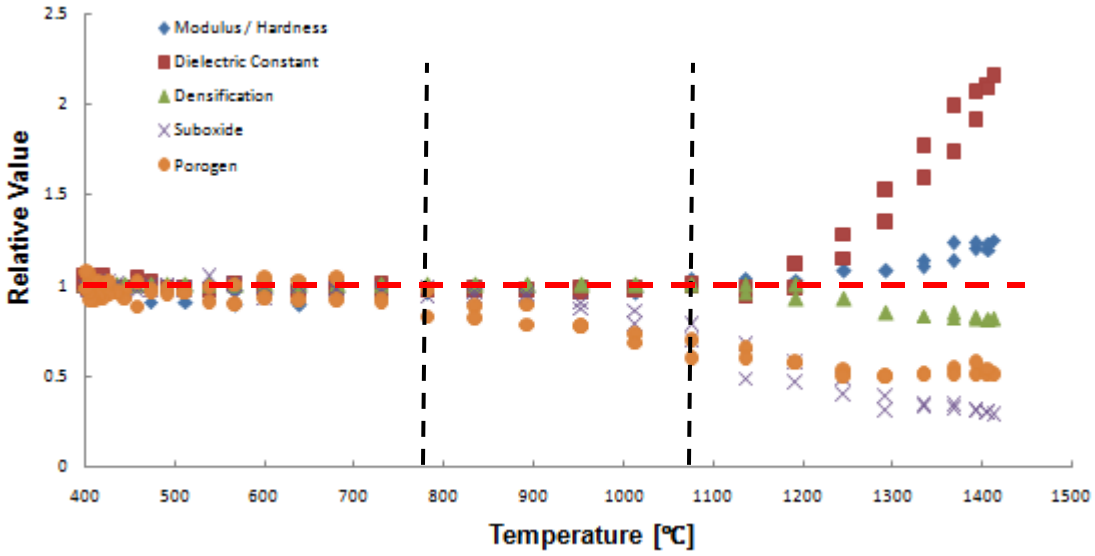


a) Modulus/hardness, dielectric constant, densification, suboxide and porogen.

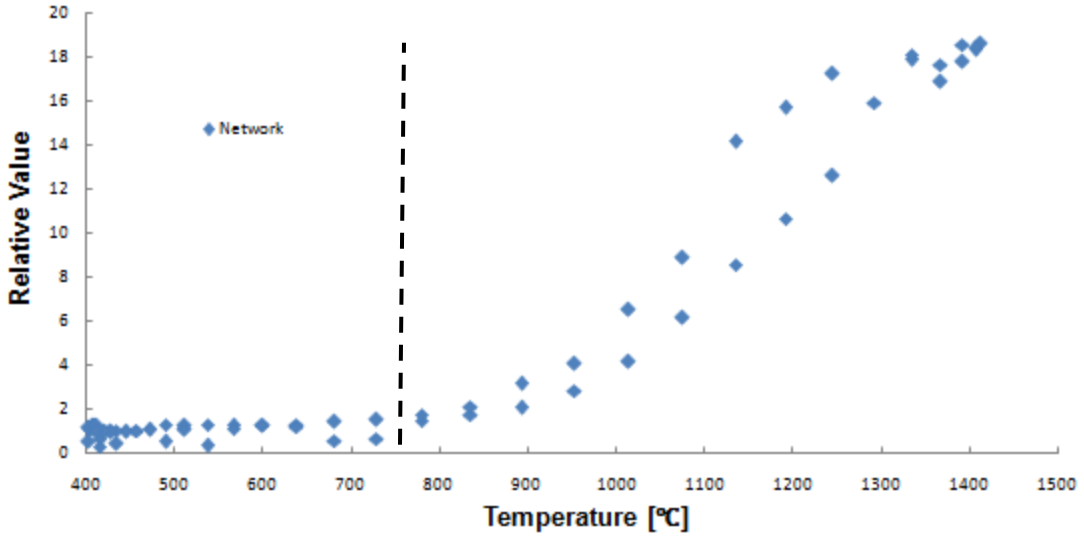


b) Network.

Figure 6.4 Temperature-dependant modulus and hardness evolution, related to the structural and dielectric constant evolution.

The modulus is observed to increase in the same temperature range, 1000-1100 ℃, as the *k* value. Above this threshold temperature, porogen removal and pore generation cease, and densification begins. Thus densification, due to the collapse of the pores, appears to be the primary factor controlling both the *k* value and the modulus. Densification only occurs after pores cease to be created, and hence porous conditions are very important in designing effective low dielectric materials.

At a lower threshold temperature range, 700-800 ℃, the structural transformation from suboxide to network is observed, but the modulus and the k value do not change substantially. This is because porogen removal and pore generation also begin to be important at 700-800 ℃, and any modulus increase by network creation is offset by the pore creation. The increased network connectivity, linked with densification, has an effect on the modulus and the *k* value only after pores cease to be created.

CHAPTER 7

# CONCLUSION AND FUTURE WORK

In this thesis, dielectric films with *k* values below 2.5 were successfully synthesized using a sol-gel process, combined with hotplate and laser spike annealing. Results show that LSA is effective in reorganizing the Si-O-Si structure and generating porosity from remnant organic groups. Compared to hotplate annealing alone, LSA is able to retain the cage structure and achieve a higher amount of structural transformation from suboxide to network due to its short heating duration which prevents too rapid oxidation of the film.

The influence of laser temperature, dwell time, porosity, and the initial structure on the chemical structures and the final properties were explored. The transformation from suboxide to fully network-oxide is observed following high temperature LSA. The threshold temperature for this behavior shifts to a higher temperature as the LSA dwell time is reduced.

The initial porosity has a significant effect on the final structure after laser annealing. It directly affects the initial structure including the fraction in an Si-O-Si network and the initial pore concentration. It also indirectly affects the progression of the suboxide-to-network transformation due to the limited space in the structure. For dense samples, with a high fraction of initial network and an extremely low density of pores, the dielectric constant (3.8-3.9) approaches that of silicon dioxide (4.0). Annealing of porous samples at extremely high temperatures and longer dwell times also results in film which approach the dense sample and exhibit a dielectric constant approximately 3.8.

The initial structure also affects the amount of the transformation from suboxide to network. Difference of the initial structure occur from two mechanisms. First, differences in the local environment of the sol solution can lead to the structural differences between samples. Second, temperature variation during hotplate heating also has a significant effect on the initial structure.

To obtain reproductive results, the time interval between the preparation of the sol solution and the spin-coating should be minimized to reduce the inhomogeneities in the sol solution. In addition, the temperature uniformity of the hotplate should be verified and controlled.

Observation of the structural evolution, the dielectric constant evolution and the modulus evolution, of porous samples under a short dwell time (0.5 ms) LSA anneal, reveals two important threshold temperatures, 700-800 ℃ and 1000-1100 ℃. Above 700-800 ℃, the network begins form while pores are also being generated. These two effects result in the dielectric constant and the modulus changing only slightly with temperature. Above 1000-1100 ℃, no additional pores are created but the network continues to form resulting in film densification. With densification, both the modulus and the dielectric constant begin to increase. Control of pore formation, network formation, and densification are the primary factors during LSA.

In future work, several aspects of this thesis should be improved or investigated. First, given the large influence from the initial structure and the pores, the initial network, the porosity, and the pore distribution should be quantified. During synthesis, studies to understand the control of the initial structure and the pores should be undertaken. By changing the amount of the acid, the porogen, and the water/alcohol ratio, additional information about the initial structure and pores can be obtained to optimize the desired initial structure and porosity. Further understanding of the role of LSA in reorganizing the pores should be expanded.

Second, as a new material feature in this thesis, the existence of carbon bridge in the final films still needs to be confirmed. In this work, the NMR spectroscopy was not feasible as the films could not be dissolved in the required solution. However, the solid-state NMR may be useful in analyzing the chemical environment of the silicon and carbon atoms[40]. Thus an attempt to utilize solid-state NMR is recommended.

Third, the thickness of the low *k* film is an essential value to calculate the dielectric constant, but the resolution of the P10 profilometer is inadequate. Ellipsometric measurements are recommended for all thickness measurements. Given the difficulty of fitting data with ellipsometry, it will likely be necessary to create reference profiles with the optical properties of the low *k* materials.

Fourth and also relevant to the film thickness, the surface topology of the film needs to be improved. The roughness of these sol-gel films may explain some of the dielectric breakdown observed during capacitance measurements of some samples. The variations of the film surface may be caused by nanoparticles in the sol solution. This also would be mitigated by shortening the time interval from the solution preparation to the spin-coating.

## REFERENCES


[1] W. Volksen, R. D. Miller, and G. Dubois, "Low dielectric constant materials", *Chemistry Review*, vol. 110, pp. 56-110, 2010.

[2] A. Grill, S. M. Gates, T. E. Ryan, S. V. Nguyen, and D. Priyadarshini, "Progress in the development and understanding of advanced low k and ultralow k dielectrics for very large-scale integrated interconnects-State of the art", *Applied Physics Reviews*, vol. 1, 011306, 2014.

[3] J. Y. Kim, M. S. Hwang, Y. H Kim, H. J. Kim, and Y. Lee, "Origin of low dielectric constant of carbon-incorporated silicon oxide film deposited by plasma enhanced chemical vapor depostion", *Journal of Applied Physics*, vol. 90, No. 5, 2001.

[4] K. Maex, M. R. Baklanov, D. Shamiryan, S. H. Brongersma, and Z. S. Yanovitskaya, "Low dielectric constant for microelectronics", *Journal of Applied Physic*s, Vol. 93, No. 11, 2003.

[5] V. Sundar, R. Yimnirun, B. G. Aitken, and R. E. Newnham, "Structure-property relationships in the electrostriction response of low dielectric permittivity silicate glasses", *Materials Research Bulletin*, Vol. 33, No.90, pp.1307-1314, 1998.

[6] Tapan Gupta, *Copper interconnect technology*. Blacklick, OH: McGraw-Hill Professional Publishing, 2008, pp. 67-81.

[7] A. Grill, and D. A. Neumayer, "Structure of low dielectric constant of extreme low dielectric constant SiCOH films: Fourier transform infrared spectroscopy characterization", *Journal of Applied Physics*, Vol. 94. No. 10, pp. 6697-6707, 2003.

[8] W. Volksen, G. Dubois, A.Kellock, T. P. Magbitang, R. D. Miller, D. Miller, S. Cohen, E. E. Simonyi, L. Tamirez, D. Markle, S. Chen, S. Zhou, X. Wang, and Y. Wang, "Mechanical enhancement of low-k organosilicates by laser spike annealing", *Journal of The Electrochemical Society*, Vol. 155, No. 10, pp. 224 –230, 2008.

[9] G. Dubois, W. Volksen, T. Magbitang, M. H. Sherwood, R. D. Miller, D. M. Gage, and R. H. Dauskardt, "Superior mechanical properties of dense and porous organic/inorganic hybrid thin films", *Journal of Sol-Gel Science and Technology*, Vol. 48, pp. 187-193, 2008.

[10] G. Dubois, W. Volksen, T. Magbitang, R. D. Miller, D. M. Gage, and R. H. Dauskardt, "Molecular network reinforcement of sol-gel glasses", *Advanced Materials,*Vol.19, pp. 3989-3994, 2007.

[11] D. Lin, L. Hu, Z. Li, and D. A. Loy, "Influence of alkylene-bridging group length on mesostructure and porosity in cubic (*Pm3n*) periodic mesoporous bridged polysilsesquioxanes", *Journal of Porous Materials*, Vol. 21, pp. 39-44, 2014.

[12] D. Boday, R. J. Stover, B. Muriithi, and D. A. Loy, "Mechanical properties of hexylene- and phenylene-bridged polysilsesquioxane aerogels and xerogels", *Journal of Sol-Gel Science and Technology*, Vol.61, pp. 144-150, 2012.

[13] D.M. Gage, L. Peng, J. Stebbins, K. S. Yim, A. Albayati, A. Demos, and R. H. Dauskardt, "Effects of e-beam curing on glass structure and mechanical properties of nanoporous organosilicate thin films", *International Journal of Materials Research,* vol.101, pp. 228-235, 2010.

[14] S. Mehta, C. Dimitrakopoulos, R. Augur, J. Gambino, A. Chou, T. Hook, B. Linder, W. Tseng, R. Bolam, D. Harmon, D. Massey, S. Gates, and H. Nye, "Evaluation of device damage from e-beam curing of ultra low-k BEOL dielectrics", in *Advanced Metallization Conference(AMC),2005 International Conference* on, 2006, pp. 361-367.

[15] S. Jain, V. Zubkov, T. Nowak, A. Demos, and J. Rocha, "Porous low-k dielectrics using ultraviolet curing", *Solid State Technology*, Vol. 48, No. 43, 2005.

[16] Krishna Iyengar, "Modeling sub-millisecond laser spike annealing process", PhD thesis, Cornell University, 2012.

[17] Byungki Jung, "Laser-induced millisecond heating of polymers and small molecules for pattern development", PhD thesis, Cornell University, 2014.

[18] B. Jung, C. K. Ober, and M. O. Thompson, "Addressing challenges in lithography using submillisecond post exposure bake of chemically amplified resists", *Proceedings of SPIE*, Vol. 7972, p. 797219 (6 pp.) 2011.

[19] J. T. Verdeyen, Laser Electronics. Upper Saddle River, New Jersey: Prentice Hall, Inc., 1995, pp. 8-62.

[20] J. Satcher (2005). Novel materials from sol-gel chemistry, [Online]. Available: www.IInL.gov/str/ May05/Satcher.html.

[21] J. D. Wright, and N.A.J.M Sommerdijk, *Sol-gel materials chemistry and applications*. Boca Raton, Florida: CRC Press, 2000.

[22] F. Goethals, E. Levrau, G. Pollefeyt, M. R. Baklanov, I. Ciofi, K. Vanstreels, C. Detavernier, I. V. Driessche and P. Van Der Voort, " Sealed ultra low-k organosilica films with improved electrical, mechanical and chemical properties", *Journal of Materials Chemistry,* Vol. 1, pp. 3961-3966, 2013.

[23] J. C. Sturm, and C. M. Reaves, "Fundamental mechanisms and doping effects in silicon infrared absorption for temperature measurement by infrared transmission", *Proceedings of SPIE*, Vol. 1393, pp. 309-315, 1991.

[24] A. Delan, M. Rennau, S. E. Schulz, and T.Gessner, "Thermal conductivity of ultra low-k dielectrics", *Microelectronic Engineering*, Vol. 70, pp. 280-284, 2003.

[25] C.J.M. Lasance (2004). The thermal conductivity of silicon dioxide, [Online]. Available: www.electronics-cooling.com/2004/08/the-thermal-conductivity-of-silicon-dioxide.

[26] D. Lin-Vien, N. B. Colthup, W. G. Fateley, and J. G. Grasselli, *The handbook of infrared and Raman Characteristic frequencies of organic molecules.* San Diego, California: Academic Press, 1991.

[27] S. M. Thomos (2014). Infrared and Raman Spectroscopy, [Online]. Available: http://serc.carleton.edu/61673.

[28] N. N. Brandt, O. O. Brovko, A. Y. Chikshev, and O. D. Paraschuk, "Optimization of the rolling-circle filter for raman background subtraction", *Applied Spectroscopy*, Vol. 60, No. 3, pp. 288-293, 2006

[29] K. Janssens (2014). X-ray photoelectron and augur electron spectroscopy, [Online]. Available: http://webh01.ua.ac.be/mitac4/micro_xpsaes.pdf.

[30] R. M. A. Azzam, and N. M. Bashara, *Ellipsometry and polarized light.* San Diego, CA: Elesevier Inc., 2003.

[31] S. Lee (2011), C-V measurement tips, tricks and traps, [Online]. Available: www.keithley.com/data?asset=55766.

[32] S. Lee (2009), Fundamentals of semiconductor C-V measurement, [Online]. Available: www.keithley.com/data?asset=52523.

[33] W. C. Oliver, and G. M. Pharr, "Measurement of hardness and elastic modulus by instrumented indentation: Advances in understanding and refinements to methodology", *Journal of Materials Research,* Vol. 19, No.1, pp. 3-20, 2004.

[34] M. R. Baklanov, J. de Marneffe, D. Shamiryan, A. M. Urbanowicz, H. Shi, T. V. Rakhimova, H. Huang, and P. S. Ho, "Plasma processing of low-k dielectrics", *Journal of Applied Physics,* Vol. 113, No. 041101, pp. 1-41, 2013.

[35] G. Das, G. Mariotto, and A. Quaranta, "Microstructural Evolution of Thermally Treated Low-Dielectric Constant SiOC:H Films Prepared by PECVD", *Journal of The Electrochemical Society*, Vol. 153, No. 3, pp. 46-51, 2006.

[36] C. Doux, K. C. Aw, M. Niewoudt, and W. Gao, "Analysis of HSG-7000 silsesquioxane-based low-k dielectric hot plate curing using Raman spectroscopy", Microelectronic Engineering, Vol.83, pp. 387-391, 2006.

[37] E. S. Park, H. W. Ro, C. V. Nguyen, R. L. Jaffe, and D. Y. Yoon, "Infrared spectroscopy study of microstructures of poly(silsesquioxane)s", *Chemistry of Materials*, Vol. 20, No. 4, pp. 1548-1554, 2008.

[38] M. S. Oliver, "Molecular origins of mechanical properties in hybrid glasses", PhD dissertation, Stanford University, 2010.

[39] Mrunalkumar Chaudhari, and Jincheng Du, "Reaction mechanisms of oxygen plasma interaction with organosilicate low-k materials containing organic crosslinking groups", *Journal of Vacuum Science and Technology A*, Vol 30, 061302, 2012.

[40] A. Zenasni, V. Jousseaume, P. Holliger, L. Favennec, O. Gourhant, P. Maury, and G. Gerbaud, "The role of ultraviolet radiation during ultralow k films curing: Strengthening mechanisms and sacrificial porogen removal", *Journal of Applied Physics*, Vol. 102, 094107, 2007.

[41] C. S. Yang, K. S. Oh, J. Y. Ryu, D. C. Kim, J. S. Yong, C. K. Choi, H. J. Lee, S. H. Um, and H. Y. Chang, "A study on the formation and characteristics of the Si-O-C-H composite thin films with low dielectric constant for advanced semiconductor devices", *Thin Solid Film*, Vol. 390, pp. 113-118, 2001.

[42] E. Duguet, Introduction to Hybrid Organic-Inorganic Materials, [Online]. Available: http://www.icmcb-bordeaux.cnrs.fr/duguet/hoim-ed3.pdf.

[43] J. Bao, H. Shi, J. Liu, H. Huang, and P. S. Ho, "Mechanistic study of plasma damage of low k dielectric surfaces", *Journal of Vacuum Science and Technology B*, Vol. 26, No. 1, pp. 219-226, 2008.

# APPENDIX

## *Optical Characterization by Ellipsometry*

A Woollam Spectroscopic Ellipsometer in CNF was used to measure the optical properties and thickness of low k material as deposited and after furnace pre-anneal. Ellipsometry is based on the change of polarization state upon reflection of a highly polarized light beam from sample surface[30]. Shown in As Figure 4.8, the incident light is polarized in two directions: perpendicular (s) and parallel (p). The reflection and transmission are given by

$$r_s = \frac{E_{rs}}{E_{is}} = \frac{\tilde{n_1}\cos\theta_i - \tilde{n_2}\cos\theta_t}{\tilde{n_1}\cos\theta_i + \tilde{n_2}\cos\theta_t} \quad (1)$$

$$r_p = \frac{E_{rp}}{E_{ip}} = \frac{\tilde{n_2}\cos\theta_i - \tilde{n_1}\cos\theta_t}{\tilde{n_2}\cos\theta_i + \tilde{n_1}\cos\theta_t} \quad (2)$$

$$t_s = \frac{E_{ts}}{E_{is}} = \frac{2\tilde{n_1}\cos\theta_i}{\tilde{n_1}\cos\theta_i + \tilde{n_2}\cos\theta_t} \quad (3)$$

$$t_p = \frac{E_{tp}}{E_{ip}} = \frac{2\tilde{n_1}\cos\theta_i}{\tilde{n_2}\cos\theta_i + \tilde{n_1}\cos\theta_t} \quad (4)$$

$$\tilde{n} = n + ik \quad (5)$$

where the complex parameter, ñ, is determined by the refraction index, n, and the extinction coefficient, k. The refraction index controls the light speed in the phase, given by

$$c_p = \frac{c_0}{n}. \quad (6)$$

The extinction efficient controls the absorption loss, described by the absorption coefficient as

$$\propto = \frac{4\pi k}{\lambda} \quad (7)$$

When the multiple reflection and transmission are considered, the sum of reflectivity is given by

$$r = r_1 + r_2 = r_{01} + t_{01} \times r_{12} \times t_{10} \times e^{-\frac{4\pi k}{\lambda}d} \times e^{-\frac{2\pi n}{\lambda}id_x} \quad (8)$$

where the term of $e^{-\frac{4\pi k}{\lambda}d}$ is due to the absorption, and the term of $e^{-\frac{2\pi n}{\lambda}id_x}$ is due to the path length difference ($d_x = 2d\cos\varphi_t$).

Ellipsometry detects the changes of the aptitude, ψ, and the phase, Δ, between perpendicular polarization (s) and parallel polarization (p), determined by

$$\tan\psi\, e^{i\Delta} = \frac{r_p}{r_s}. \tag{9}$$

As shown in the equations, the changes of the aptitude, ψ, and the phase, Δ, are determined by the refraction index, n, the extinction coefficient, k, the film thickness, d, the incident angle, $\theta_i$, and the refractive angle, $\theta_t$. The incident angle $\theta_i$ was fixed (70° and 75° were explored in this thesis) and the refractive angle $\theta_t$ was determined by Snell's Law. By varying the refraction index, n, the extinction coefficient, k and the thickness, d, the ellipsometry results can be modeled.

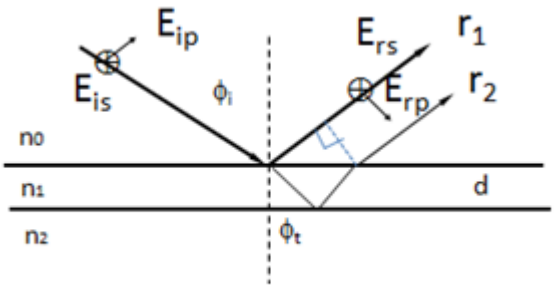


Figure 1 Mechanisms of Ellipsometer